Photoluminescence of ZnO and a multiple quantum well Al$_{0.5}$Ga$_{0.5}$As/GaAs

Dang Thai Giang

A dissertation submitted to

Kochi University of Technology

in partial fulfillment of the requirements

for the degree of

Doctor of Philosophy

Department of Environmental System Engineering

Kochi University of Technology

Kochi, Japan

August 2011

Acknowledgements

I would like to express my deepest gratitude to people, whose supervision, guidance, support, and help played an indispensable role in completion of this thesis.

First of all, I would like to thank Professor Taniwaki Masafumi, my primary supervisor, for his guidance and support during my PhD period. Thank you for providing me with the implanted ZnO wafers, for performing the TEM experiments, for teaching me the TEM technique, for giving me freedom in doing research, and especially for being tolerant to my sometimes impulsive nature.

I am also very grateful to Professor Kanbe Hiroshi, my co-supervisor, who always inspires me with his famous saying "you can try". Your saying gave me strong encouragement to pursue problems that I was really interested in. Your guidance in writing and submitting a manuscript will be helpful for me in far future.

For the generosity of Dr. Kawaharamura Toshiyuki, whom I also consider as my co-supervisor though unofficially, I am deeply in debt. Thank you for teaching me the XRD, FE-SEM, ellipsometry techniques and for introducing me to the mist CVD method, which I see great prospective in. Your warm care helped me a lot during the hardest times of my PhD.

I would like to extend my warmest thanks to Professor Lawrence Hunter, who spent endless time and effort in editing my English writing. Your academic English writing courses were among the most effective courses I have ever taken and your two-page system would be helpful for the rest of my life.

The work related to tin ion implantation in ZnO was conducted with assistance of Professor Yoshiie Toshimasa from Kyoto University Research Reactor Institute, for which I am very grateful.

I also wish to thank Professor Hirao Takashi for providing me with access to the facilities of the Nano-device Research Institute, Kochi University of Technology.

To Professor Momota Sadao, thank you very much for monitoring my PhD process.

I would like to thank Dr. Nitta Noriko, who provided me with access to the FIB and TEM facilities.

To Ms. Yamasaki Momoko, thank you a lot for your guidance in SEM and XRD usage and for your warm friendship. Thanks are extended to Mr. Yamamoto Tomoki, who taught me the TEM sample preparation procedure by ion milling.

I really appreciate the effort of all KUT IRC staff members to make my staying in Japan comfortable, enjoyable, and memorable.

Abstract

Nowadays, nanotechnology plays an important role in developments of semiconductor industry. For optoelectronic device applications, it is highly desirable to understand photoluminescence mechanisms in nano-scale semiconductor structures such as a quantum well and a near surface layer in an ion-implanted semiconductor wafer. This thesis aims at studying mechanism of i) room temperature PL of an $Al_{0.5}Ga_{0.5}As/GaAs$ multiple quantum well and ii) the deep-level band PL of hydrothermal ZnO wafers implanted with 60 keV Sn^+ ions. In addition, excitation power and temperature dependent PL as well as formation of implantation-induced defects in the ZnO wafers are also investigated. Motivation for these studies will be advocated below.

Since 1970s, AlGaAs/GaAs QWs have found widespread applications in (opto)electronic devices working in the red-to-infrared regions. In the study of an AlGaAs/GaAs quantum well, however, problems still remain. First, the ratio of the intensity of the $n = 1$ electron-light hole transition ($1e - 1lh$) to that of the $n = 1$ electron-heavy hole transition ($1e - 1hh$) transition is known to increase with temperature due to the thermal population of holes from the $1hh$ sublevel to the $1lh$ sublevel. Nevertheless, to my knowledge, no model has yet been put forward to describe this phenomenon quantitatively. This study proposes a model in which the temperature dependence of the above ratio can be described by an exponential function of reciprocal temperature. The model was verified against experimental observations in the temperature range 40–340 K. Second, the mechanism of PL at room temperature (RT) in AlGaAs/GaAs quantum wells has been a long-standing controversial problem. Researchers have been extensively debating the question whether the photoemission at RT results from excitonic recombination and/or free-carrier recombination. A common approach to determining the recombination mechanism is to observe the dependence of the PL intensity I_{PL} on the excitation power I_{ext}. This dependence can be described by the formula: $I_{PL} = C \times I_{ext}^t$, where C is a constant, and the exponent t has a value of 1 for excitonic recombination and a value of 2 for free-carrier recombination. In previous studies, such excitation-power dependence measurements have been performed at only few temperatures, which did not allow a detailed investigation of the variation of the PL mechanism. In this study, the PL spectra of a MQW $Al_{0.5}Ga_{0.5}As/GaAs$ was measured from 5 to 296 K in small steps of 15–20 K with numerous excitation powers. The results show that as temperature was increased from 5 to 120 ± 20 K the value of t increased from 1.03 to 1.37 ± 0.5; at temperatures from 120 ± 20 to 296 K, t remained constant at 1.37 ± 0.5. These results indicate that i) as the temperature increases from 5 to 120 ± 20 K, excitons are dissociated and free-carrier recombination gradually makes a larger contribution to the total PL intensity of

the $1e-1hh$ transition, ii) above 120 ± 20 K, the relative contributions from free-carrier recombination and, thus, excitonic recombination to the total PL intensity do not vary. This tendency is confirmed by the temperature dependence of the energy difference between the $1e-1hh$ transition and the bulk GaAs band gap.

Among oxide semiconductors, ZnO possesses many superior characteristics such as a large direct RT band gap of ~3.3 eV and a large binding energy of 60 meV. ZnO was studied as early as in 1935 and has recently been of renewed interest due to developments in growth technique and great concern about (opto)electronics devices working in the blue and violet regions. Despite an enormous effort paid to ZnO research, problems still remain in the field. For example, implantation-induced defects as well as dynamic annealing are not yet well understood, effect of pulsed laser excitation power on temperature dependent PL of ZnO has not been studied, and debate on the origin of various defects responsible for deep level (DL) photoluminescence (PL) band ranging from green to yellow-orange regions (1.9-2.5 eV) is still continuing. In the current thesis, ZnO wafers were implanted at RT and low-temperature (LT) (near liquid nitrogen temperature) with 60 keV Sn^+ ions to doses from 3.1×10^{12} to 1.5×10^{15} ions/cm^2. The implanted wafers and an unimplanted one were systematically characterized by transmission electron microscopy (TEM), photoluminescence (PL), X-ray diffractometry (XRD), atomic force microscopy (AFM), scanning transmission electron microscopy (STEM), X-ray energy-dispersive spectroscopy (EDS), Hall measurement, reflectance and transmittance techniques at RT. Combination of temperature and excitation dependent techniques were employed to measure PL in the temperature range from 5 to 298 K in small steps of 10–20 K. Both excitations with pulsed laser and cw laser were utilized. The defect formation was investigated. When possible, relation between variations of the PL of the near-band-edge (NBE) and deep-level (DL) bands and changes in data obtained by the other techniques was discussed.

TEM, STEM, and EDS techniques were employed to examine ZnO wafers implanted with 60 keV Sn^+ ions at RT to a dose of 8.0×10^{14} ions/cm^2 and at LT to a dose of 1.5×10^{15} ions/cm^2. These ion implantation doses do not render the ZnO wafers amorphous. Within the sensitivity of the EDS measurement device, no regular variations in the relative concentration of O and Zn atoms are observed down to 120 nm under the sample surface.

Photoluminescence spectra of a hydrothermal ZnO wafer implanted at RT to a dose of 3.6×10^{12} ions/cm^2 were measured in the temperature range from 5 to 298 K. The sample was excited by means of the 266-nm line of an Nd^{3+}: YAG Q-switched pulsed laser with numerous average excitation powers in the range from 0.33 mW to 7.50 mW. At constant temperatures, the most intense PL peak red-shifts with average excitation power, whereas positions of other near-band-edge peaks remain unchanged. It was experimentally proven that the red-shift is not due to local

heating at the excited spot. Rather, it is due to relaxation of photo-excited carriers to lower energy transitions as the most intense transition is saturated by high excitation photon density. Furthermore, the temperature dependence of the most intense PL peak energy was fitted with the Varshni equation. The Varshni coefficients α and β decrease with increasing pulsed laser excitation power.

Hydrothermal ZnO wafers implanted at RT with 60 keV Sn$^+$ ions to doses of 3.6×10^{12}, 4.1×10^{13}, 8.0×10^{13}, 1.6×10^{14}, and 2.5×10^{14} ions/cm^2 were examined by photoluminescence (PL), atomic force spectroscopy (AFM), and X-ray diffractometry (XRD) techniques. The PL intensity significantly decreases in the wafers implanted to the doses of 4.1×10^{13} ions/cm^2 and higher. The AFM measurements indicate that the roughness variation is not the cause of the significant decrease in PL intensity. Furthermore, under illumination of the He-Cd laser 325 nm line the DL band peak in the PL spectra of the implanted samples blue-shifts, and the DL band intensity first increases and then steadily decreases with illumination time. The illumination time dependence of the deep-level PL intensity is similar to the dependence of EPR V_O^+ signal reported previously. The abnormal behaviors of the DL band are discussed in details in the thesis body text.

Table of contents

List of acronyms

ADF - Annular dark field

AFM – Atomic force microscopy (or microscope)

b1 RT 8×10^{14} ions/cm^2 sample – ZnO wafer implanted at room-temperature to a dose of 8×10^{14} ions/cm^2

BF – Bright-field

CCD – Charge-coupled device

CTEM – Conventional transmission electron microscopy

cw – continuous-wave

DF – Dark-field

DL – Deep-level

DTE – Detection energy

EDS – Energy dispersive spectrometry

HAADF - High-angle annular dark field

HEMT – High electron mobility transistor

HRTEM – High-resolution transmission electron microscopy

LED – Light emitting diode

LT – Low-temperature

MQW – Multiple quantum well

NBE – Near-band-edge

PL – Photoluminescence

PLE – Photoluminescence excitation

QD – Quantum dots

QW – Quantum well

QWIP – Quantum-well infrared photodetectors

RMS – Root mean square

RT – Room-temperature

SAED – Selected area electron diffraction

SEM – Scanning electron microscopy (microscope)

SRIM – the Stopping and Range of Ions in Matter

STEM – Scanning transmission electron microscopy

TEM – Transmission electron microscopy (or microscope)

UV – Ultra-violet

XRD – X-ray diffraction (or diffractometer)

YO – Yellow-orange

1 Introduction

Nowadays, nanotechnology plays an important role in developments of semiconductor industry. Photoluminescence is a simple technique, which is routinely utilized to characterize nanostructures such as quantum wells, quantum wires, quantum dots, thin films, and a thin near surface layer of an ion-implanted semiconductor wafer. Photoluminescence (PL) is spontaneous emission of light resulting from recombination of electron-hole pairs, which are created by another light excitation source. Study on photoluminescence plays an indispensable role in fabrication process of radiative devices such as lasers, light emitting diodes (LED), electroluminescence panels, and cathodoluminescence of cathode ray tubes (CRT) [1]. Moreover, energies of peaks, which normally appear in PL spectra, provide useful information about energy levels in semiconductor structures. Those peaks are referred to in the field as transitions. When an electron returns from an occupied level in the conduction band to an unoccupied level (a hole) in the valence band, the process is called recombination. There exist many kinds of recombination. If the electron returns to the unoccupied state directly, the process is referred to as free-carrier recombination. On the other hand, the electron can interact with the hole by an attractive Coulomb force to form an exciton, similarly to the interaction of an electron with a nuclear in a hydrogen atom. Excitonic recombination occurs when the exciton collapses releasing a photon. The exciton can be also bound to a donor or acceptor to form a donor-bound or acceptor bound exciton (DBX or ABX). Collapse of these bound excitons results in peaks, whose energies are smaller than energy of the un-bound or free exciton (FX). More complicatedly, when an exciton bound to a neutral donor collapsed, part of its energy can be transferred to an electron on the donor; as a result, energy of the DBX transition decreases and the donor is left in an excited state. This process results in two electron satellites (TES) in PL spectra [2, 3]. Similar process occurring in a neutral-acceptor-bound exciton complex results in two hole satellites [4, 5]. Thus, not only PL research is useful for device applications, but also mechanism of various PL transitions provides a researcher with rich physics to investigate. This thesis aims at studying mechanism of i) room temperature PL of an $Al_{0.5}Ga_{0.5}As/GaAs$ multiple quantum well and ii) the deep-level band PL of hydrothermal ZnO wafers implanted with 60 keV Sn^+ ions. In addition, excitation power and temperature dependent PL as well as implantation-induced defects in the ZnO wafers are also investigated. Motivation for these studies will be advocated below.

1.1 AlGaAs/GaAs – a classical quantum well

Nanotechnology has been occupying a central place in industrial development recently. Nanotechnology deals with low-dimensional structures, in which the size of at least one dimension is reduced to less than the electron de Broglie wavelength [6], typically in the range from few nanometers to few hundreds nanometers. As electrons are confined in such extremely narrow space, quantum effects naturally emerge, which make properties of the low-dimensional structures fundamentally different from those of the corresponding bulk materials. Last decades have witnessed an enormous effort (see [7] and references therein) devoted to studies of i) quantum wells and superlattices, ii) quantum wires, nanotubes, and nanorods, and iii) quantum dots and nanocrystals, where electrons are confined in one, two, and three dimensions, respectively. These studies have resulted in not only a new understanding of the quantum systems but also in fabrication of nanostructure-based devices with much better performance than bulk material-based ones (see [7, 8] and references therein). All these advances were deeply in debt to a pioneering work by R. Dingle *et al.* [9], who first observed the quantum confinement effect in an AlGaAs/GaAs multiple quantum well. Later on, a large number of studies have been devoted to the optical properties of AlGaAs/GaAs quantum wells (QWs). Photoluminescence (PL) at different temperatures [5-7], photoluminescence excitation (PLE) spectroscopy [10], and absorption [11] in these structures have all been intensively studied. As a result, AlGaAs/GaAs QWs have found widespread applications in optoelectronic devices [12]. AlGaAs/GaAs-QWs-based resonant-tunneling diodes [13, 14], laser diode [15], high electron mobility transistors (HEMT) [16], quantum cascade laser (QCL) [17], optical bistable switch [18], quantum-well infrared photodetectors (QWIP) [19], and ultrafast optical modulator [20] have been readily demonstrated.

$Al_xGa_{1-x}As$/GaAs QW is a classical QW, where the GaAs well layer is a direct band gap semiconductor and the mismatch in lattice constants of $Al_xGa_{1-x}As$ and GaAs is extremely small (less than 0.12% [8, 21]), which makes growth of abrupt $Al_xGa_{1-x}As$-GaAs interface feasible. Owing to these properties, it was not accidental that the quantum confinement effect was first observed in $Al_xGa_{1-x}As$/GaAs. From material points of view, $Al_xGa_{1-x}As$/GaAs QWs are generally preferred to bulk $Al_xGa_{1-x}As$ alloys. Due to carrier confinement effect, devices fabricated from the QWs normally show superior characteristics than those fabricated from bulk materials. For example, $Al_xGa_{1-x}As$/GaAs-QW-based lasers require lower threshold current [15] but possess higher quantum efficiency and higher output power owing to the unique step-like shape of density of states [8, 22]. In QWs, wavelength tuning also can be readily realized by variation of the well width. HEMT has been achieved utilizing the QW as a channel layer [16]. QWIPs are highly reproducible and more stable than infrared photodetectors based on narrow

band gap materials such as HgCdTe [8]. Thus, study on photoluminescence of $Al_xGa_{1-x}As$/GaAs QWs would be helpful for optoelectronic applications.

Even though properties AlGaAs/GaAs QWs have already been well-documented, problems still remain. This thesis addresses two problems.

First, in the PL spectra of AlGaAs/GaAs QWs, the strongest luminescence is caused by the transition from the $n=1$ electron sublevel to the $n=1$ heavy hole sublevel [23-25]; this transition is denoted as $1e-1hh$ in this thesis. The ratio of the intensity of the $n=1$ electron-light hole transition ($1e-1lh$) to that of the $1e-1hh$ transition is known to increase with temperature due to the thermal population of holes from the $1hh$ sublevel to the $1lh$ sublevel [23]. However, to our knowledge, no model has yet been put forward to describe this phenomenon quantitatively. This thesis proposes a model in which the temperature dependence of the above ratio can be described by an exponential function of reciprocal temperature. The model was verified against experimental observations in the temperature range 40–340 K.

Second, the dominant PL mechanism in AlGaAs/GaAs quantum wells at room temperature has been a topic of extensive debate. For a long time, researchers have been arguing whether the room-temperature photoemission dominantly resulted from excitonic recombination, or free-carrier recombination or from both of them. Normally, the exciton binding energies of excitons in most studies fluctuated around 10 meV [23, 25-30], which is well below room-temperature thermal energy of ~26 meV. Therefore, if the quantum confinement effect is not considered, the excitons should be readily dissociated at room temperature. However, due to the small thickness of the well layer, the free electrons and holes are effectively confined in the well to form electron-hole pairs. Therefore, excitonic recombination is possible even at room temperature, according to many authors [12, 23, 31, 32]. Christen and Bimberg et al. [31] have constructed a complicated theory of line shapes for free-carrier recombination and excitonic recombination. By fitting the PL spectrum measured at 300 K with their constructed formulae, they concluded that excitonic recombination was the predominant PL mechanism at 300 K. Dawson et al. [32] have measured the PL and photoluminescence excitation (PLE) spectra at room temperature. Due to

the closeness in energy of peaks observed in the PL spectrum and those in the PLE spectrum, they concluded that the luminescence in the PL spectrum was due to the excitonic recombination. Jiang *et al.*[23] observed temperature dependence of energy differences between the $1e-1hh$ and $1e-1lh$ peaks and the bulk GaAs band gap. The differences remained unchanged with temperature. This led them to the conclusion that excitonic recombination is still dominant even at room-temperature. However, using the same approach, Fouquet *et al.* [33] and Zhongying *et al.*[25] reported that the energy differences did increase with temperature, indicating the dissociation of excitons at high temperature. Another common approach to determining the recombination mechanism is to observe the dependence of the PL intensity I_{PL} on the excitation power I_{ext}. This dependence can be described by the formula [25, 33]: $I_{PL} = C \times I_{ext}^t$, where C is a constant, and the exponent t has a value of 1 for excitonic recombination, a value of 2 for free-carrier recombination, and a value between 1 and 2 for an intermediate case. Fouquet *et al.* [33] and Zhongying *et al.* [25] reported the value of 2 and 1.91 for the t exponent determined at room temperature and at 300 K, respectively. Their conclusion was in favor of free-carrier recombination. On the other hand, utilizing the same approach, Hayakawa *et al.* [34] concluded that the PL is the result of both free-carrier and excitonic recombination because the t exponent values determined at room temperature were 1.45 and 1.21 for the (111)- and (100)-oriented MQWs, respectively. In previous studies [25, 33, 34], such excitation-power dependence measurements have been performed at solely few temperatures, which did not allow a detailed investigation of the variation of the PL mechanism. In this study, the excitation-power dependence was measured from 5 to 296 K in small steps of 15–20 K. In addition, PLE and temperature dependence of difference in energy between the MQW's peaks and bulk GaAs band gap were utilized to study the PL mechanisms.

1.2 ZnO – a promising material for blue-ultraviolet (opto)electronics and transparent
electronics

Even though AlGaAs/GaAs has been widely applied in fabrication of numerous (opto)electronic devices working in the red-infrared ($h\nu < 1.9$ eV) region, extension of this material to devices working in the blue-ultraviolet (UV) region ($h\nu > 2.8$ eV) is impeded by a fundamental limitation, that is, the low band gap energy of GaAs (1.424 eV at 300 K [21]). Oxide semiconductors are potential materials of choice for the application owing to their higher RT band gaps (ZnO-3.3 eV [35], α-Ga$_2$O$_3$-5.3 eV [36], MgO-7.8 eV [37], In$_2$O$_3$-3.75 eV [38], and α-Fe$_2$O$_3$-2.6 eV [39]). Among oxide semiconductors, ZnO is probably the most promising material. ZnO was studied as early as in 1935 [40], and has recently been of renewed interest due to developments in growth technique [41] and great concern about blue-UV (opto)electronics devices and transparent electronics [37]. Some researchers even called the recent period as the renaissance of ZnO [42] probably because of an significant increase in the number of papers devoted to ZnO during the last decade. In atmospheric pressure and RT conditions, single crystalline ZnO is stable in the wurtzite structure [37]. Wurtzite ZnO possesses a direct RT band gap of ~3.3 eV and large exciton binding energy of 60 meV. The latter energy is much larger than RT thermal energy (~26 meV). Therefore, excitonic lasing is feasible even at RT [43]. Alloying ZnO with CdO and MgO can vary the band gap energy from 2.9 to 4 eV [37], which is another advantage of ZnO. In addition, growth of ZnO nanostructures such as quantum well [44], quantum wires [45], quantum dots [46] have been all demonstrated. The superior characteristics mentioned above widen the range of applications of ZnO. ZnO-based transparent thin-film transistor (TTFT) [47], heterostructure field-effect transistor (HFET) [48], diode [49], LED [50], laser [51], piezoelectric device [52], gas sensor [53] have been readily fabricated.

Despite an enormous effort paid to ZnO research, problems still remain in the field. For example, achievement of reproducible and stable p-type ZnO is challenging [35], implantation-induced defects as well as dynamic annealing are not yet well understood [54], effect of pulsed laser excitation power on temperature dependent PL of ZnO has not been studied, and debate on the origin of various defects responsible for deep level (DL) photoluminescence (PL) band ranging from green to yellow-orange regions (500-600 nm) [55-60] is still continuing. The current thesis addresses three problems as described below.

First, little is known about the formation and annihilation of implantation-induced defects in ZnO probably due to rather small number of studies on ion-implanted ZnO by means of transmission electron spectroscopy, which is one of primary techniques to investigate an ion-implanted layer. Iwanaga *et al.*[61] have reported that high voltage electron irradiation caused formation of interstitial loops. The interstitial were i) O interstitials displaced by irradiating

electrons and ii) excess Zn interstitials originally residing in the crystal before electron irradiation. Annealing ZnO implanted with As^+ ions, Coleman *et al.* [62] have illustrated that implantation-induced damage layer was thermally less stable unimplanted ZnO. In addition, the study of Kucheyev *et al.*[54] indicates that ZnO possessed strong dynamic annealing against 300 keV Au ion implantation, whereas relatively low dose of 60 keV Si ions could induce crystalline-to-amorphous phase transition in ZnO. Tin is also another group IV element like silicon. However, the effect of tin ion implantation on properties of ZnO has not been studied. On the other hand, Nitta *et al.* have reported formation of anomalous cellular structure in GaSb implanted with 60 keV Sn^+ ions [63, 64]. Moreover, a dose of 10^{14} Sn ions/cm^2 could render GaAs amorphous according to Taniwaki *et al* [65]. Therefore, the study of Sn ion implantation-induced defects in ZnO and comparison with other materials are highly desirable.

Second, little attention has been paid to effect of pulsed laser excitation on PL of ZnO, even though PL spectra excited by a continuous-wave laser has been studied rather carefully from low temperature of 2 K to RT of 300 K. Low temperature (LT) photoluminescence of bulk ZnO was reported early in 1965 in the study of Reynolds *et al.* [66]. In that study, ten prominent near-band-edge (NBE) peaks were observed and labeled as I_1-I_{10}. Later studies (see [55] and references therein) confirmed the presence of those peaks and the notion of Reynolds *et al.*[66] has been widely utilized. Recently, numerous studies have been devoted to temperature dependent PL of ZnO [67-75]. Most of these studies [67, 69-73] utilized a continuous-wave (cw) laser as an excitation source except for the studies of Zhang *et al.* [68] and Cao *et al.* [74], which utilized pulsed laser excitation. However, researchers have not addressed the question whether and how pulsed laser excitation power variation causes changes in i) position of PL peaks and ii) Varshni coefficients α and β derived from temperature dependence of the peaks.

Third, the notorious problem remaining in the study of ZnO is roles of various defects (point defects such as V_O, O_i, V_{Zn}, Zn_i, Li_i, Li_{Zn}, Cu_{Zn}, and their complexes) in the photoemission of the deep-level (DL) band stretching from the green region (around 2.4 eV) to yellow-orange region (around 2.1 eV) [55-60, 76]. Many defects were attributed to the green band. Dingle [77] found that the ratio of intensities of the peaks at 2.85908 and 2.85897 eV was identical to that of the natural abundances of ^{63}Cu and ^{65}Cu. Consequently, it was concluded that the green band arose from Cu_{Zn} point defects [55, 77]. Nonetheless, later studies also suggested V_{Zn}, Zn_i, O_{Zn}, and V_O as origins of the green band (see [55] and references therein). For instance, it has been reported in [78] that an EPR (electron paramagnetic resonance) signal with g = 1.9560 directly correlated to the green band PL intensity. The authors of [78] attributed this signal to V_O^+ centers. Annealing data of Studenikin *et al.* [58] appeared to support this assignment. However, as has been pointed out in [55], the g = 1.9560 value is close to the g-factor of effective mass (EM)

shallow donors rather than V_O^+ [79, 80]. The V_O^+ centers caused the EPR signal with $g_\parallel$=1.9948 and $g_\perp$=1.9963, according to Smith and Vense [81]. For the assignment, they have put forward very strong arguments based on the presence of 4.1% natural abundance of the ^{67}Zn isotope. Base on this assignment, Vlasenko and Watkins [79] have demonstrated a direct correlation between the yellow-orange (YO) band PL and the ODEPR (optical detection of electron paramagnetic resonance) signal of the V_O^+ centers. In contrast to Vlasenko and Watkins [79], Liu *et al.* [59] attributed the YO band to O_i. On the other hand, Nikitenko [82] concluded that the YO band results from Li_{Zn}. As evident, much confusion occurred in literature mainly because the green-yellow-orange PL band is relatively broad and highly asymmetric, indicating that numerous transitions of close energy contribute to it. For identification of the origins of those transitions it is necessary to: first vary the conditions, which can cause changes in position and/or intensity of the band, then analyze why those changes occur. Several methods have been applied, for example, utilizing different growth techniques and varying parameters during the growth processes [57-59], and annealing ZnO in different atmospheres [56, 60]. As an alternative, implantation technique has been widely employed to vary optical and electronic properties, structure, and morphology of materials [54, 61-63, 83, 84]. Thus, it would be interesting to study influence of Sn ion implantation on the deep-level PL band.

In the current thesis, ZnO wafers were implanted at RT and LT (near liquid nitrogen temperature) with 60 keV Sn$^+$ ions to doses from 3.1×10^{12} to 1.5×10^{15} ions/cm^2. The implanted wafers and an unimplanted one were systematically characterized by transmission electron microscopy (TEM), PL, X-ray diffractometry (XRD), atomic force microscopy (AFM), scanning transmission electron microscopy (STEM), energy-dispersive spectroscopy (EDS), Hall measurement, reflectance and transmittance techniques at RT. Combination of temperature and excitation dependent techniques were also employed to measure PL in the temperature range from 5 to 298 K in small steps of 10–20 K. Both excitations with pulsed laser and cw laser were utilized. The defect formation was investigated. When possible, relation between variations of the PL of the NBE and DL bands and changes in data obtained by the other techniques was discussed.

2 Experiments

2.1 The samples

2.1.1 The multiple quantum well $Al_{0.5}Ga_{0.5}As/GaAs$

The sample utilized in this study is depicted in (Figure 1). The sample was grown on a (100)-oriented GaAs substrate by molecular beam epitaxy. It consisted of a 0.5-μm-thick $Al_{0.5}Ga_{0.5}As$ buffer layer, 100 periods of alternating $Al_{0.5}Ga_{0.5}As$ and GaAs layers and a 6-nm-thick GaAs cap layer. The grown layers were unintentionally doped. The $Al_{0.5}Ga_{0.5}As$ barrier width was close to 10 nm and the GaAs well width, determined from the PL peaks (see below), was 9.6 ± 0.6 nm (17 ± 1 monolayers).
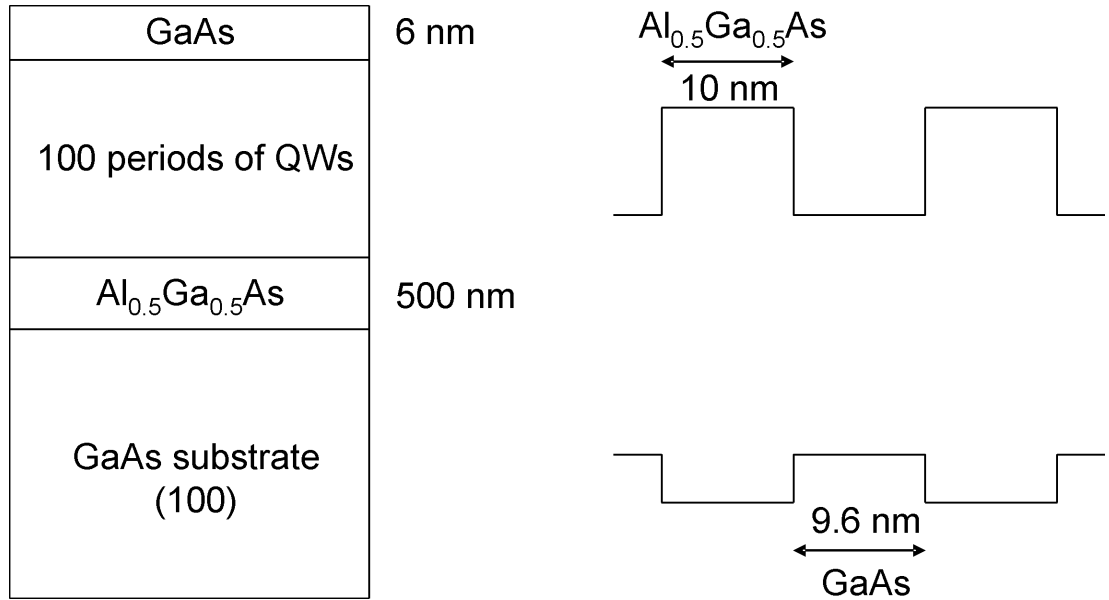

Figure 1. The $Al_{0.5}Ga_{0.5}As/GaAs$ multiple quantum well utilized in the study.

According to [21], $Al_xGa_{1-x}As$ ternary alloys crystallize in the zinc blende structure for all x from 0 to 1. For x < 0.41-0.45 [21], $Al_xGa_{1-x}As$ is a direct band gap semiconductor, the Γ-valley is the lowest valley. For x > 0.45, $Al_xGa_{1-x}As$ is an indirect band gap semiconductor, the X-valley is lower than the Γ-valley. However, in this study $Al_{0.5}Ga_{0.5}As$ is treated as a direct band gap semiconductor when calculating the band offsets and the electron effective masses of the barrier in the Kronig-Penney model. The lattice mismatch between $Al_{0.5}Ga_{0.5}As$ and GaAs at 300 K was calculated to be 0.07% based on the formula: $a(x) = 5.6533 + 0.0078x$ in [21], where $a(x)$ is the lattice constant of $Al_xGa_{1-x}As$. With such a small lattice mismatch, the abrupt change in band gap energy is expected in the interface of $Al_{0.5}Ga_{0.5}As$ and GaAs. For the detail parameters of the $Al_xGa_{1-x}As$ ternary alloys, readers are referred to the reference [21].

2.1.2   The batches of hydrothermal ZnO wafers implanted with Sn^+ ions.

Hydrothermal ZnO wafers were purchased from ORBE PIONEER LTD. The purity of the wafers was advertised to be 99.99%. According to the producer website, the ZnO wafers contained other impurities in ppm level as listed in Table 1. Ion implantation was performed by Professor Taniwaki Masafumi from Kochi University of Technology.

Table 1. Concentrations of various impurities in ppm in the purchased hydrothermal ZnO wafers. The table was taken from the website of the producer ORBE PIONEER LTD.

Ca	Mg	Fe	Ni	Cu	Mn	Cr	Co
1.83	4.69	0.61	0.92	0.007	0.15	<0.01	<0.02
Ag	Ti	Al	Li	Mo	V	Na	K
<0.02	0.049	0.67	1.1	<0.02	<0.01	6.53	6.1

The zinc surface of the wafers was implanted by a home-made ion implanter, which locates at Kyoto University Research Reactor Institute, Japan. A titanium filament was heated up to approximately 1500 ^{o}C. Electrons sputtered from the filament ionized the Ar atoms which filled the chamber. The ionized Ar atoms were accelerated by an electric field of 750 V between the filament and the target. The target was made from phosphor bronze (CuSnP), which contains 3.5-10 % Sn and 0.03-0.35 % P. The accelerated Ar atoms bombarded the target and caused the sputtering of its constituents Cu, Sn, and P. The ions Cu, Sn, and P were accelerated by a 60 keV electric field. Subsequently, the 60 keV Cu, Sn, and P entered a tube surrounded by a wire coil. Magnetic field produced by current running through the coil exerted Lorentz force on the ions. As a result, Cu, Sn, and P ions were bent in different trajectories, which enabled selection of solely Sn ions. The 60 keV Sn^+ ions perpendicularly bombarded the zinc surface of a ZnO wafer, which was stored in a 2×10^{-6} Torr chamber. The temperature of the wafer was kept at room temperature (RT) or nearly liquid nitrogen temperature (see **Error! Reference source not found.**). Hereafter the liquid nitrogen temperature was referred to as low temperature (LT). There were two batches of samples. The implantation dose of the samples in the two batches was listed in **Error! Reference source not found.**. **Error! Reference source not found.** also specifies which characterization techniques were performed in which samples. For brevity, the samples are hereafter referred to by their batch, implantation temperature, and implantation dose. For example, the b2 RT 8.0×10^{13} ions/cm^2 sample is the wafer in batch 2 implanted at RT to a dose of 8.0×10^{13} ions/cm^2.

Table 2. Implatation dose of the sample in the batches 1 and 2 and characterization techniques performed on the samples.

Sample		Dose 10^{14} ions/cm^2	Tempearture, K	Implantation time	Date
Batch	Temperature				
1	Unimplanted	0			2009/12/6
	RT	2			2009/12/6
		4			2009/12/6
		8			2009/12/6
		1.5			2009/12/6
	LT	4	112	27'20''	2009/12/19-20
		8	112	46'12''	2009/12/19-20
		1.5	112	30'30''	2009/12/19-20
2	RT	0.036	298	25''	2010/05
		0.41	298	3'40''	2010/05
		0.8	298	5'	2010/03
		1.6	298	14'	2010/03
		2.5	298	21'	2010/03
	LT	0.41	131	15'50''	2010/9/10
		0.88	133	14'	2010/9/10
		2.4	114	27'30''	2010/9/9
		4.9	128	49'29''	2010/9/14

(Continue)

Sample		Dose 10^{14} ions/ cm^2	Characterization techniques							
Batch	Tempe-rature		PL	CTEM	STEM	EDS	XRD	AFM	Trans. and Refl.	Hall
1	Unim-planted	0							O	O
	RT	2							O	O
		4							O	O
		8		O	O	O			O	O
		1.5		O	O	O			O	O
	LT	4							O	O
		8							O	O
		1.5		O	O	O			O	O
2	RT	0.036	O				O	O	O	O
		0.41	O				O	O	O	O
		0.8	O				O	O	O	O
		1.6	O				O	O	O	O
		2.5	O				O	O	O	O
	LT	0.41					O		O	
		0.88					O		O	
		2.4					O		O	
		4.9					O		O	

O: performed and reported in this thesis.
Empty box: not reported in this thesis.

2.2.1   Photoluminescence techniques

2.2.1.1   Simple photoluminescence (PL)

In the PL technique, an electron is excited from the valence band to the conduction band leaving a hole in the valence band by means of an excitation source, whose energy is larger than the energy of the semiconductor band gap. The excited electron and hole then relax to the bottom of the conduction and the top of the valence band, respectively. Subsequently, the electron and hole recombine releasing by a photon. The process is illustrated in (Figure 2)
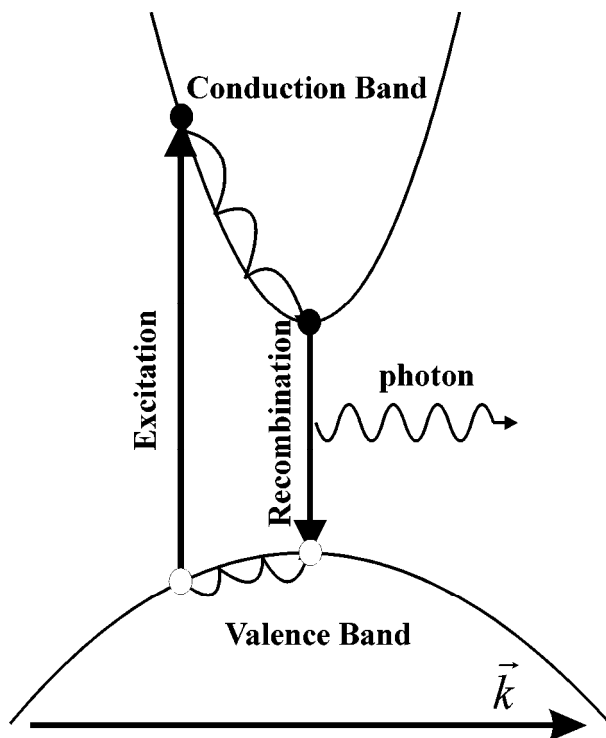
Figure 2. Energy scheme in PL technique

To measure the PL of the $Al_{0.5}Ga_{0.5}As/GaAs$ MQW, the sample was excited with a 635 nm line of a laser diode. The PL emission was focused onto the slit of a 0.3-m-diffraction-grating monochromator (Acton Research Corporation SpectraPro®-300i), whose blaze wavelength and groove density were 1 μm and 600 g/mm, respectively. A 100×1340 Roper Scientific CCD (charge coupled device) array was used to record the PL signal. The system was calibrated by Spectrograph Calibration method (see the manual WinSpec Princeton Instruments Spectroscopic Software Version 2.5C). In the excitation-power dependence measurements, output power of the

laser diode was varied with an optical attenuator and was registered by means of an optical power meter.

To measure PL of a ZnO implanted at RT with Sn^+ ions to a dose of 3.6×10^{12} ions/cm^2 at temperature range from 5 to 298 K, the same system as that in the previous paragraph was utilized except for the excitation laser and the grating. When the near-band-edge (NBE) PL was measured (357-422 nm), the grating, whose blaze wavelength and groove density were 0.3 μm and 1200 g/mm, respectively, was utilized. When the whole spectrum including deep-level PL was measured (330-800 nm), the grating, whose blaze wavelength and groove density were 0.5 μm and 1200 g/mm, was utilized. Since any position of the last grating could not cover the wide wavelength range from 330 to 800 nm, the "Step and Glue" data acquisition mode was used. The minimum overlap was 45 nm. The sample was excited with the 266-nm line of the fourth harmonic generation from an Nd^{3+}: YAG Q-switched pulse laser (pulse duration: ~10 ns, repetition rate: 16 kHz, maximum output average power: ~10 mW). The pulse peak power was approximately 10^3 times more than the measured maximum output average power. The average excitation power was varied from 0.33 ± 0.02 to 7.5 ± 0.05 mW by means of an optical attenuator. The excited area was estimated to be 10^{-5} cm^2. Note that accuracy of the estimated area was limited merely to the order of the value because the excited-spot size could not be determined precisely.

The PL of ZnO wafers implanted with 60 keV Sn^+ ions at RT to doses of 3.6×10^{12}–2.5×10^{14} ions/cm^2 was also measured by a HOBIRA Jobin Yvon system. The samples were excited with the 325-nm line of a continuous wave He-Cd laser. The PL emission was focused onto the slit of a 0.32-m-diffraction-grating spectrometer (iHR320 HOBIRA Jobin Yvon), and a 256×1024 pixel CCD (charge coupled device) array (the Synapse CCD camera HOBIRA Jobin Yvon) was used to record the PL signal.

To compare the effect of the 266 nm line Q-switched pulsed laser excitation and the 325 nm line cw He-Cd laser excitation on PL of the b2 RT3.6 × 10^{12} ions/cm^2 ZnO wafer, room-temperature PL spectra excited by both lasers were measured by means of the HOBIRA Jobin Yvon system. The excited spot areas were 1.2×10^{-3} and 2.6×10^{-4} cm^2 in the cases of pulsed laser and cw laser excitation, respectively.

The two measurement systems are hereafter referred to shortly as the Princeton and Hobira systems.

2.2.1.2   Photoluminescence excitation (PLE)

Photoluminescence excitation (PLE) technique is a powerful technique to determine energy levels in semiconductors. Different from PL technique, in the PLE technique the excitation wavelength is varied. PL spectra are measured for all excitation wavelengths [see (Figure 3)(a)]. These PL spectra then are normalized by excitation power [see Fig. 3 (b)]. Subsequently, a detection wavelength is fixed, and the normalized PL intensity at the detection wavelength is plotted as a function of excitation wavelengths. As a result, a PLE spectrum is obtained. For simple imagination, if the Fig. 3(b) is cut by a plane perpendicular to the Detection Wavelength axis, the resulting intersection is a PLE spectrum. Figure 3(c) shows some PLE spectra at different detection wavelengths. The arrow in Fig. 3(c) indicates the detection wavelength or detection energy (DTE) as normally denoted in PLE spectra. The DTE is usually selected at the low-energy shoulder of a peak observed in a PL spectrum. Though the PL intensity is measured, a PLE spectrum is similar to an absorption spectrum because the more photons of some excitation wavelength a sample absorbs, the more photons of the detection wavelength the sample emits. However, PLE spectroscopy is generally more sensitive than absorption spectroscopy, e. g. in many cases transitions, which do not appear in an absorption spectrum, can be readily resolved in a PLE spectrum.
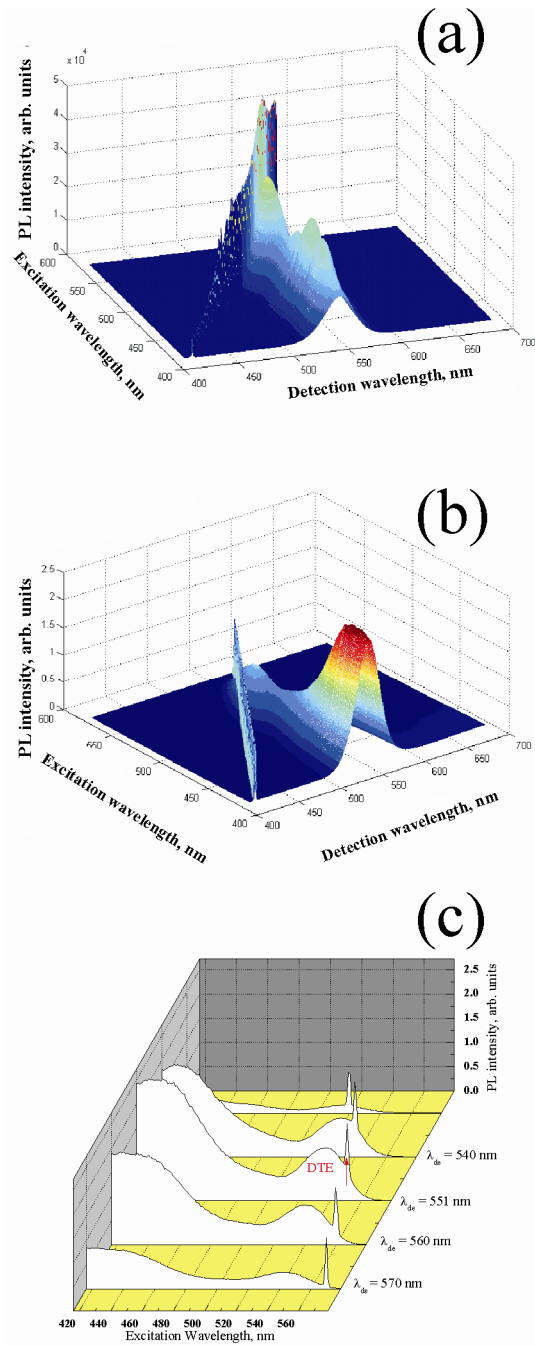
Figure 3. (For illustration purpose only) (a) PL spectra of CdSe quantum dots measured with numerous excitation wavelengths (b) normalized PL spectra, whose intensity was normalized by excitation power (c) some representative PLE spectra at different detection wavelengths.

In this study, PLE measurement was performed only in the $Al_{0.5}Ga_{0.5}As/GaAs$ MQW at 5 K. Experimental scheme for PLE measurement is shown in (Figure 4). The excitation source was a Ti: sapphire laser, whose wavelength was varied in the range 716–820 nm with a step of about 1 nm. Part of the laser beam was divided by a half mirror and measured by a power-meter for normalizing PL spectra.
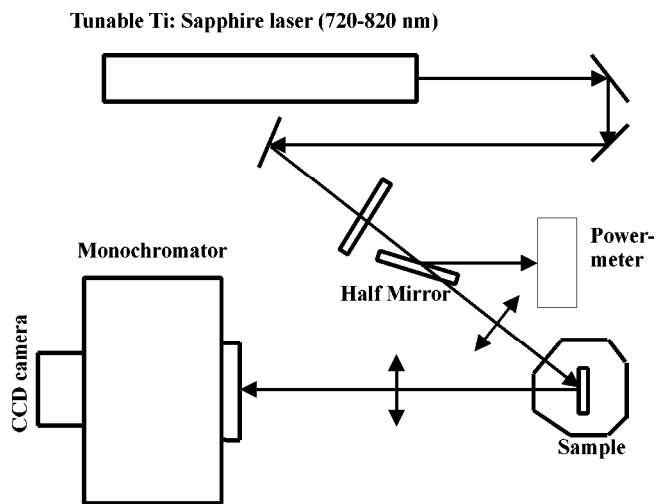
21

Figure 4. Experimental scheme for PLE measurement.

2.2.2   Transmission and reflection

Figure 5 shows experimental scheme for transmission and reflectance measurements. The measurements were conducted by means of a UV-4100 C system. The light source provided wavelengths in the range from 176 to 2500 nm. As shown in Figure 5, the light incident beam made angles of 0 and 5 degrees with respect to the normal of the sample surface in the transmission and reflection measurements, respectively. In addition, a system of four mirrors was also utilized in the reflectance measurement (see Figure 5).
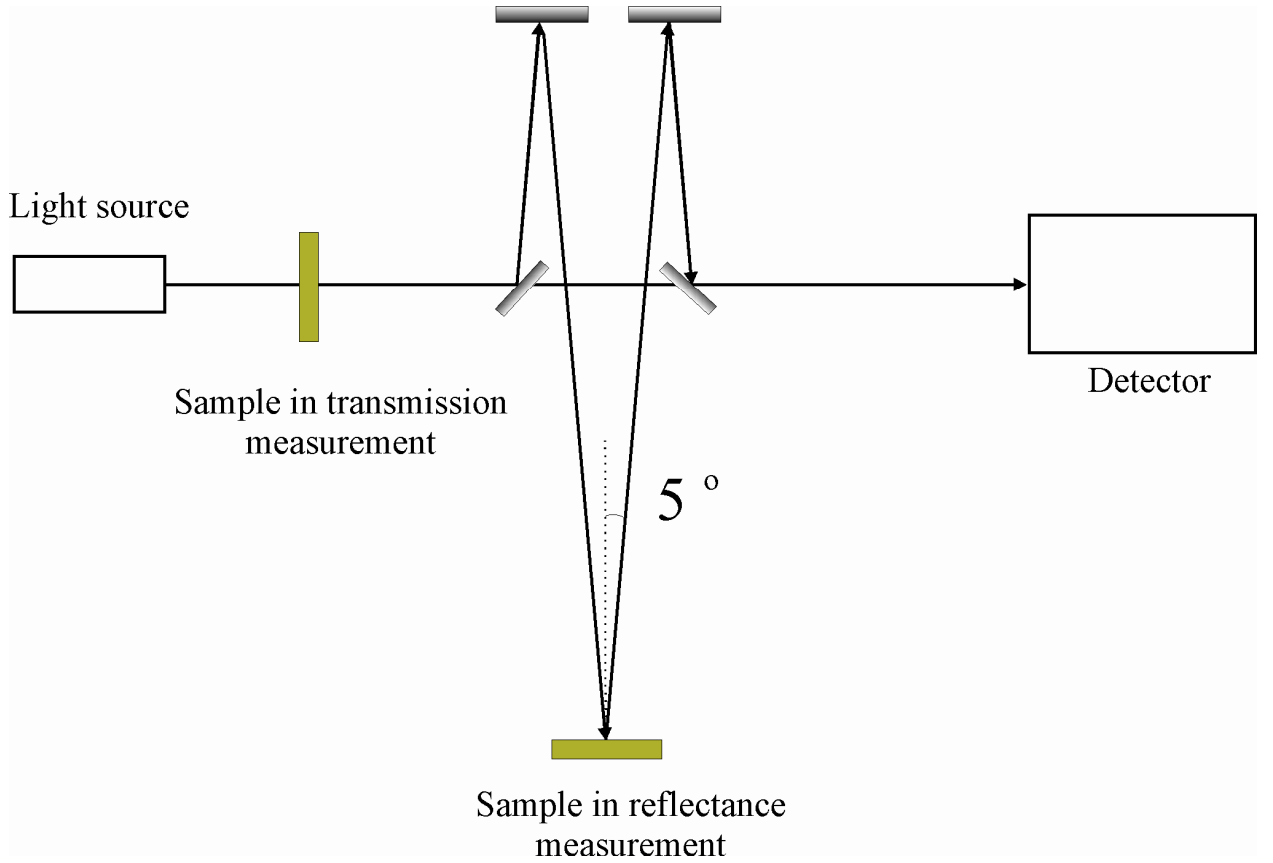
Light source

Sample in transmission
measurement

Detector

$5\,^{\circ}$

Sample in reflectance
measurement

Figure 5. Experimental scheme for transmission and reflectance measurements.

2.2.3 Four-point Van De Pauw measurements

Currently, the resistivity, Hall mobility, and carrier concentration measurements are routinely conducted in the conventional four-point Van der Pauw configuration [85]. In this method, four contacts are produced on the sample surface near the sample edge. An current I_{ij} is injected through contacts i and j (i: input, j: output), and the potential difference between the other two contacts $V_{kl} = V_l - V_k$ is measured. The resistance $R_{ij,kl} = V_{kl}/I_{ij}$ is calculated. According to Van der Pauw [85], the sheet resistance R_s satisfied the equation: $\exp(-\pi R_{12,34}/R_s) + \exp(-\pi R_{23,41}/R_s) = 1$, where the contacts from 1 to 4 are numbered in the anti-clockwise order. In his original paper, Van der Pauw plotted a graph, which allows determination of R_s graphically, knowing $R_{12,34}$ and $R_{23,41}$. But nowadays, the equation can be numerically resolved for the variable R_s with the help of a personal computer. The sheet resistance R_s relates to the resistivity ρ of the sample and the sample thickness d by the formula: $\rho = R_s d$. The sheet Hall coefficient R_{Hs}, Hall coefficient R_H, and mobility μ_H can be determined by the formulae: $R_{Hs} = \Delta R_{13,24}/B$, $R_H = R_{Hs} d$, and $\mu_H = |R_{Hs}|/R_s$, respectively, where B is magnetic induction and $\Delta R_{13,24} = R_{13,24\,(B \neq 0)} - R_{13,24\,(B=0)}$. The positive magnetic field

23

direction is specified in Figure 6. When $B > 0$ is applied, if $\Delta R_{13,24} < 0$, the major charge carrier is electron and $\Delta R_{13,24} > 0$, the major carrier is hole. The sheet carrier concentration n_s and carrier concentration n are calculated by the formulae: $n_s = B / e \Delta R_{13,24}$ and $n = n_s / d$. When performing Van der Pauw measurements, an operator usually commutates the contacts and switches the polarities of the injected current, measured voltage, and magnetic field to obtain statistically more accurate results.
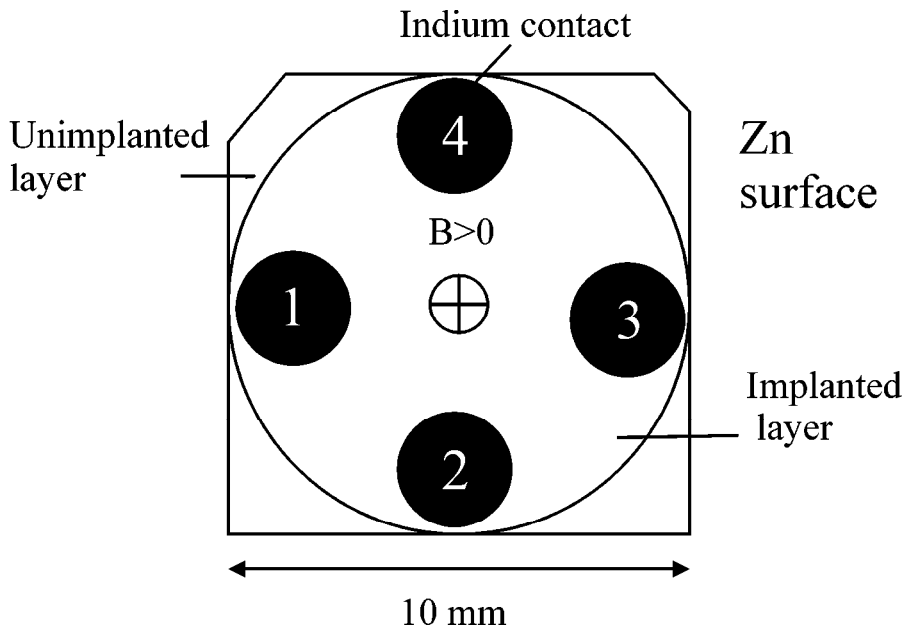

Figure 6. A ZnO wafer image denoting the implantation area, position of In contacts, positive direction of magnetic field in the four-point Van der Pauw measurements. .

In this study, the Hall measurements were conducted to investigate the variations of electrical properties of ZnO wafers with implantation conditions (dose and temperature). The measurements were conducted at RT by means of a HL5500PC Accent Optical Technologies system. The system utilized a permanent magnet of ~0.505 Tesla. After measurements of the corresponding resitances $R_{ij,kl}$, the system automatically calculated R_s, ρ, R_{Hs}, μ_H, n_s, and n, given that the thickness of 0.5 mm of the wafers was inserted *a priori*. The contacts were produced by evaporating indium in a 3×10^{-4} Pa chamber. Positions of the contacts are shown in the Figure 6.

2.2.4   X-ray diffraction (XRD)

X-ray diffraction (XRD) is a powerful tool to study crystal structures, chemical analysis and stress measurement, phase equilibria, grain size, orientation of different domains in

polycrystalline aggregates [86]. In XRD, X-ray parallel beams is utilized to irradiate a sample, the beams reflect from parallel atomic planes in the sample, the reflected beams subsequently interfere with each other. If the angle between the the X-ray beam and the atomic planes θ (see Figure 7), and the interplanar spacing between the plane d, and the X-ray wavelength λ satisfy the Bragg's law:
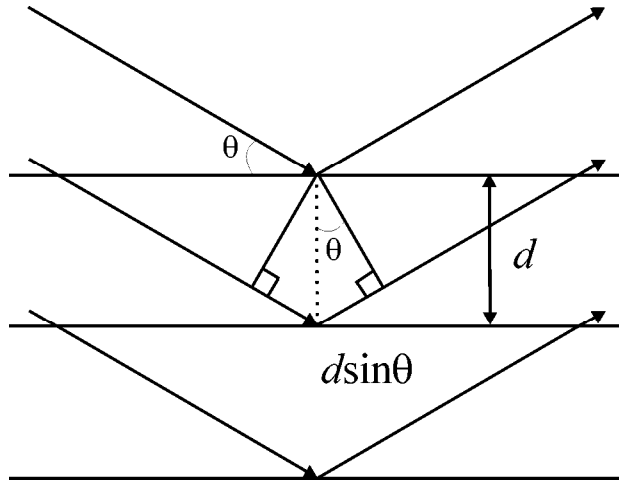

Figure 7. Scheme illustrating working principle of the X-ray diffraction.

$$2d \sin \theta = n\lambda \qquad (1)$$

where n is an integer and it is called the order of reflection, then the reflected beams produce an intense peak. There exists numerous varieties of XRD measurements such as out-of-plane, in-plane, rocking curve, and pole measurements [86]. However, in this thesis results of merely the most popular $2\theta / \theta$ measurement are reported. In this measurement, both the angles between the incident beam and i) the sample surface θ and ii) the detector 2θ are varied. The detected signal intensity is plotted as functions of 2θ.

The measurements were conducted by means of a JEOL Rigaku ATX system. The emitted X-ray from a copper target normally contained Cu Kα, CuKβ, and WLα lines. Therefore, a Ge 220 crystal collimator is utilized to i) render the incident X-ray beam parallel and ii) select solely Cu Kα (λ = 1.5418 Å) for the measurement. This experimental set up was referred to in literature as double crystal diffraction (DCD) [87, 88] configuration [see Figure 8(a)]. In addition, triple crystal diffraction (TCD) configuration [84, 89] was also utilized to improve the measurement resolution. In TCD configuration, an additional Ge 220 crystal was placed behind the sample as an analyzer [see Figure 8(b)]. In this thesis, the XRD measurements were conducted merely in the ZnO wafers not in the AlGaAs/GaAs MQW.
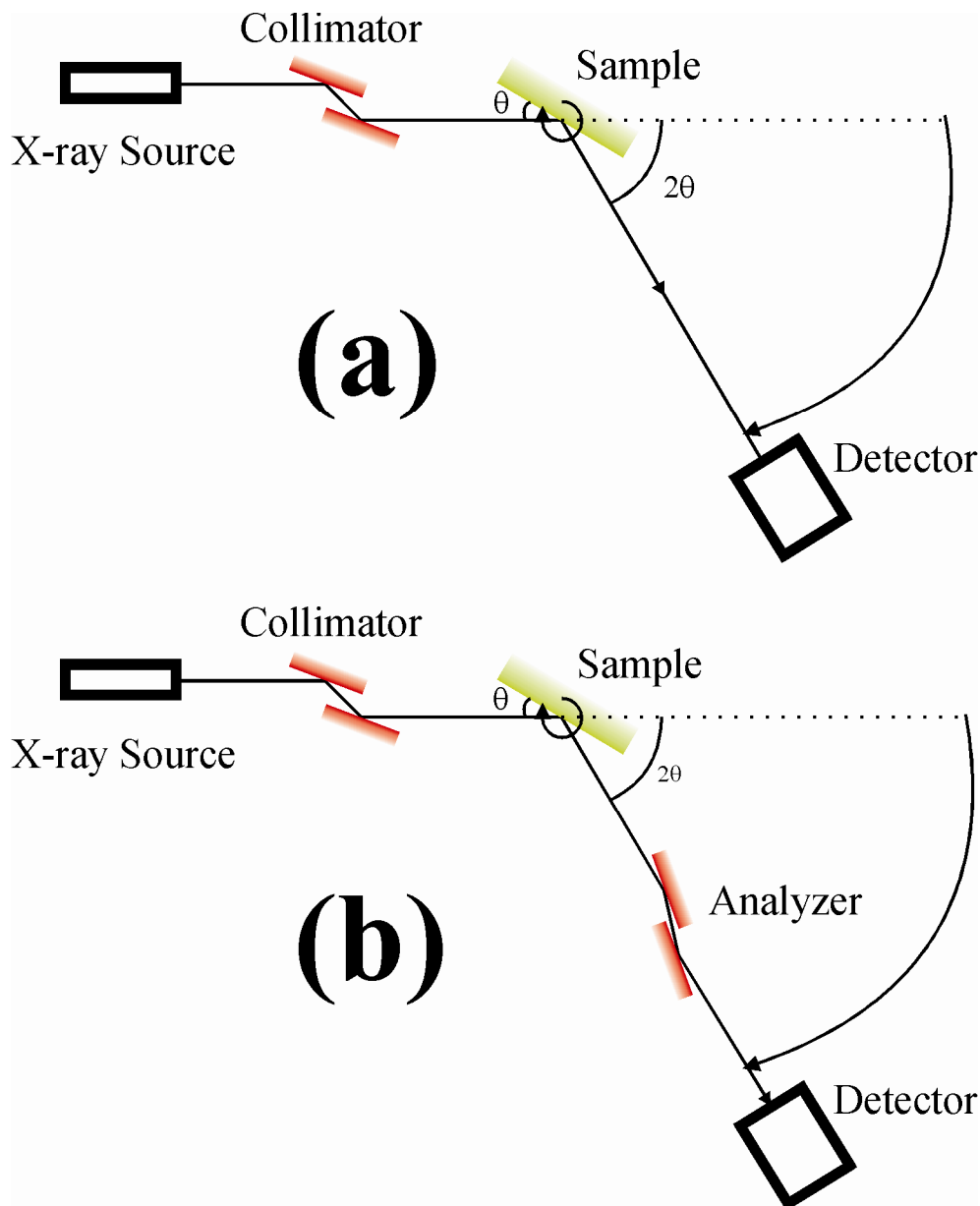
Figure 8. (a) Double crystal (DCD) and (b) Triple Crystal (TCD) X-ray diffraction configurations.

2.2.5   Atomic force microscopy (AFM)

Atomic force microscopy (AFM) is a tool to study surface morphology of interested samples. In AFM, a sharp tip attached to a cantilever is utilized to probe the sample (see Figure 9). When the tip approaches the sample surface, the atoms on the sample surface exert a force on the front atoms of the tip. This force bends the cantilever. The bending is monitored via a photo diode, which detects intensity of a reflected laser beam. The incident laser beam is directed on the top of the cantilever. A feedback system is employed to adjust the Z distance between the tip and the sample surface (see Figure 9). AFM operation is divided into static and dynamic modes [90]. In the static AFM mode, while the tip is scanning the sample surface, the feedback system adjusts the Z distance so that the force between the sample and the tip is kept constant [90, 91].

Consequently, a map of Z as a function of X and Y results in the image of the sample morphology. This imaging mode is also referred to in literature as dc contact mode [91]. In the dynamic AFM mode, the tip is deliberately vibrated. The dynamic itself is divided into amplitude modulation (AF) [92] and frequency modulation (FM) [90, 93] modes. In the AM mode, when the tip is brought close to the sample surface, the interaction between sample and the tip changed the tip oscillation amplitude, the feedback system adjust the Z distance so that the oscillation amplitude is kept constant. Similar to the static AFM mode, the AFM image results from a map of Z as function of X and Y. In the FM mode, not oscillation amplitude but oscillation frequency variation [93] is registered as function of X and Y. The frequency variation is caused by the interaction of the tip and the sample. In literature, the dynamic AFM mode is usually called non-contact mode, in the sense that the tip is not necessarily brought into contact with the sample. The dynamic AM mode has another variety mode called tapping mode, in which the driving oscillation amplitude is large so that the tip is brought to close contact with the sample surface (or tapped to sample surface) in a small time during one vibration period. This reduces the damage on the sample in comparison with the dc contact mode. In addition to the topography image type, there exist also frictional-force and phase image types. The readers are referred to the reference [91] for the detailed discussion.
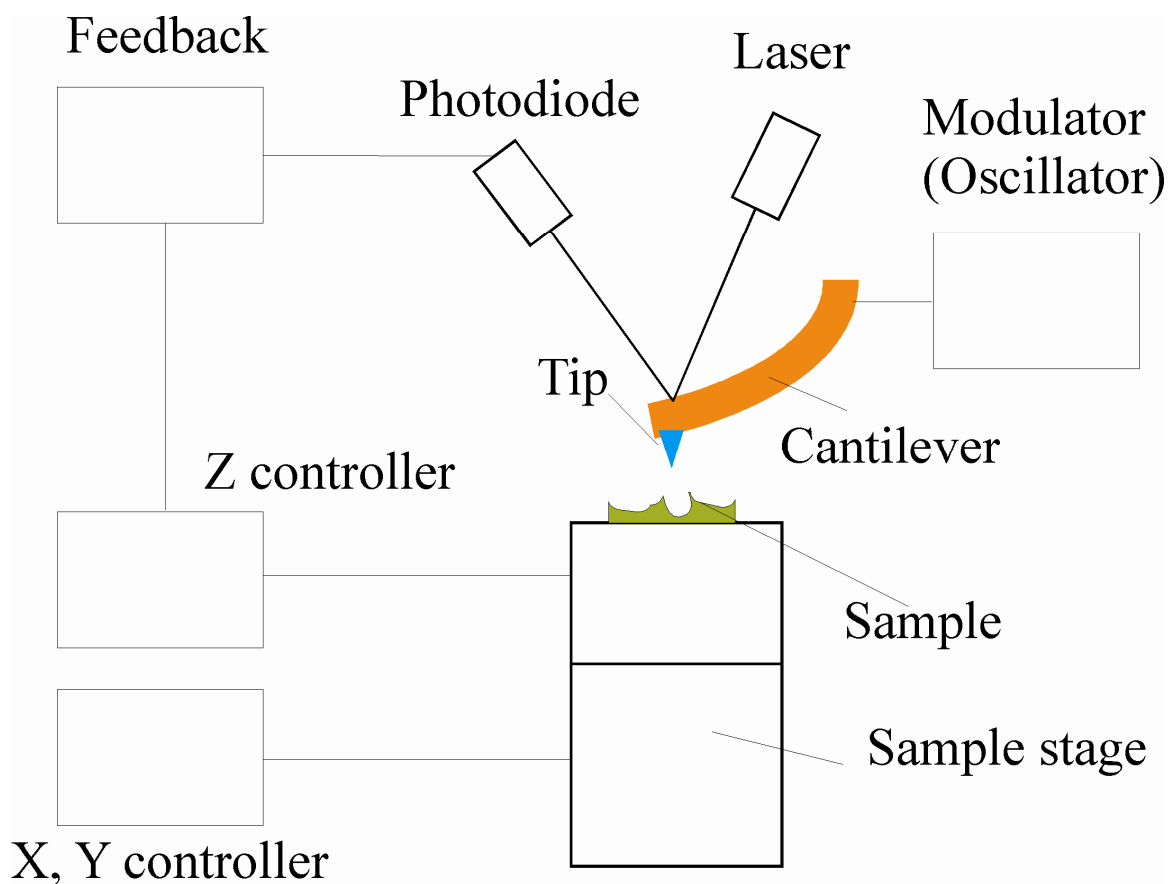

Figure 9. Simplified scheme describing the working principle of an AFM.

In this study, AFM was utilized to measure morphology of implanted ZnO wafers. The general purpose was to investigate whether the relationship between the wafer roughness and PL intensity exists. Morphology of the samples was investigated by means of a JEOL TM-4210BU Scanning Probe Microscope, which was set to the AFM contact mode.

2.2.6   SRIM

The simulation of ion implantation process has been developed since 1960s. Nowadays, the most popular software package is TRIM or SRIM (Transport of Ions in Matter or Stopping and Ions in Matter) depending on version. The software has been developed by James F. Ziegler, Jochen P. Biersack, and Matthias D. Ziegler since 1980s. Generally, the authors utilized the Monte Carlo method, detail descriptions of the method can be referred to the authors' book [94] and will not be reproduced in the current thesis. The SRIM software posseses many advandtages such as i) user-friendly interface, since the interface is self-explained and the simulation parametters are automatically provided and ii) trajectories of a large number of implanted ions can be tracked in reasonable fast time with normal mordern personal computer. However, the SRIM program suffers from two major disadvantages. First, it does not take into account the structure of the target materials [94]. Second, the program does not consider important effects during ion implantation process such as dynamic annealing [94]. In fact, as claimed by the author of the program, all calculations are performed as if all damage events happen at 0 K. Despite those limitations, SRIM is very helpfull for experimentalists, who want to know general outcomes when they implant a concrete ion into a concrete target.

The calculations itsef are rather complicate; however, for a experimentalist it is important to understand outputs that the latest SRIM version (SRIM-2011) provides. Below are outputs, which are relevant to the study reported in this thesis, :

-   The trajectories of ion implants and recoils. Here, recoils are host atoms, they either are knocked out from the previously balanced position or vibrate stronger around the balanced position after collision with the ion implants. The trajectories are depicted in four graphs: XY longitudinal, XZ longitudinal, XY ions only, and YZ lateral. Here, the X-axis is coincident with the ion incident beam direction, YZ plane are parallel to the surface of the target. The first three graphs show the depth trajectories of the recoils (XY longitudinal and XZ longitudinal) and the ions (XY ion only), whereas the last graph shows the transverse view of recoils' trajectories.
-   Ion and recoil distributions. These graphs show the depth distributions of the ion implants and recoil host atoms.

- Damage events. These graphs show the depth distributions of implantation-induced host atoms' vacancies. Note that the SRIM program treatments imply that these vacancies do not recover after being knocked out from the previous (before implantation) position. The treatments are unrealistic.

- The 3D-distributions of ions, recoils, and vacancies.

2.2.7   Conventional transmission electron microscopy (CTEM)

2.2.7.1   TEM sample preparation

The TEM samples in this study were prepared by means of a focused ion beam (FIB) FEI QUANTA 3D 200i system. The system provides Ga^+ ions, which serve to i) mill the sample, ii) deposit platinum (Pt) protection and attachment layers, and iii) monitor the preparation process. Before the preparation process, the samples were deposited with conductive Au layer to prevent charge accumulation and to protect the sample from being damaged by the ion beam in the initial stage of Pt deposition process. To deposit the Pt protection layer, C9H16Pt gas was allowed to blow on the interested region; the ion beam was directed to the region simultaneously. As a result, Pt atoms were deposited on the sample surface. After that, the ion beam was utilized to dig two trenches into the sample leaving a wall between the trenches see Figure 10(a). The top surface of the wall was covered with the Pt protection layer. The depth of the trenches was few micrometers and the thickness of the wall was about 1.5 μm. Note that the sample surface was perpendicular to the ion beam in the Pt deposition and digging steps. Next, the sample was tilted so that its surface made an angle of 45 ^{o} with the ion beam and the ion beam was utilized to cut a U-shape piece from the wall see Figure 10(b). The wall was almost cut out from the sample wafer except for a small bridge [(see the right side of the wall in Figure 10(b)]. Subsequently, a sharp tip called omniprobe was inserted into the chamber near the wall [see Figure 10(c)]. The small piece of the sample (the wall) was attached to the omniprobe by Pt deposition. The small bridge was then cut off and the small piece was taken out from the wafer [see Figure 10(d)]. Subsequently, the small piece was placed on a copper grid sample holder; Pt deposition was performed once again to attach the small piece to the copper grid [see Figure 10(e)]. The sample stage was rotated again so that the top surface of the small piece was perpendicular to the ion beam. Finally, the piece was milled to desired thickness by mean of the ion beam [see Figure 10(f)].
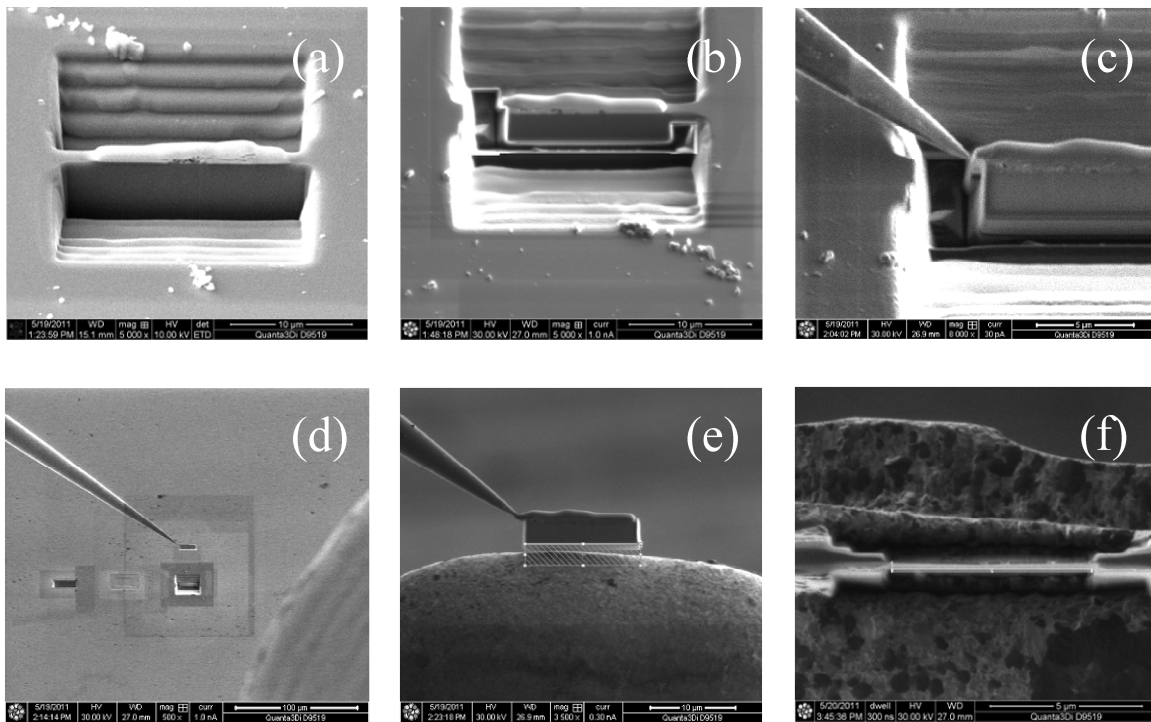
Figure 10. TEM sample preparation by means of FIB: (a) Digging two trenches, (b) U-shape milling, (c) Attaching a piece of sample to an omniprobe (d) Taking out the sample (e) Attaching the sample on a copper grid sample holder, and (f) Milling sample to desired thickness.

2.2.7.2   Operation of TEM: BF, DF, SAED, and HRTEM images

Transmission electron microscopy (TEM) is a powerful technique for observation of nanoscale structures. It has been widely utilized to characterize ion-implanted samples. In TEM, a high energy (hundreds of kilo-electron volts) electron beam is utilized to illuminate an examined sample, whose thickness is typically less than ~100 nm [95]. For imaging, TEM uses electrons that cross over the sample. If the electron beam crosses the sample without angle deviation, it is termed as a transmitted beam (or direct beam [95]), if it reflects from the sample's crystallographic planes, it is termed as a diffracted beam (see Figure 11). There exist two fundamental imaging modes in TEM. In the *diffraction mode*, the back focal plane (BFP) of the objective lens is projected onto the viewing screen; whereas in the *image mode*, the image plane of the objective lens is projected (see Figure 12). In the *diffraction mode*, normally the objective aperture is opened wide and the selected-area aperture is inserted to select the area of interest, here comes the term selected-area electron diffraction (SAED). In the *image mode*, the selected-area diffraction (SAD) aperture is usually opened wide and the objective aperture is inserted to select interested spots. Bright field (BF) and dark field (DF) regimes are usually utilized to take photos of samples. In the BF regime, the objective aperture is adjusted so that it does not

intercept the transmitted spot. Several diffracted spots around the transmitted spot can be selected also. However, it is a trade-off between the brightness and contrast, the more spots are selected the brighter the image is but the worse the image contrast is and vice versa. To take a simple DF images, the objective aperture is adjusted so that it intercepts the transmitted spot. As a result, merely diffracted spots are selected. Again, the number of selected diffracted spots depends on the quality of the image. DF images taken in this manner are generally not preferable because the diffracted beams travel off from the optic axis, which increases aberration and astigmatism. To overcome this problem, the incident beams are normally tilted so that the selected diffracted spot lies on the optic axis. This can be realized by changing the regime from Bright Tilt to Dark Tilt. This technique is called centered dark-field (CDF) imaging. Unlike BF or DF images, which result from amplitude contrast, high-resolution TEM (HRTEM) images result from phase-contrast [95]. When electron waves travel across very thin sample (typically less than 50 nm [95], as the result of scattering by the sample's atoms, the electron waves pass through the sample with uniform amplitude but with phase shift [96]. This phase shift is introduced by the atoms of the specimen; therefore, atomic resolution can be obtained in HRTEM images. It should be noted that phase shift can be introduced also by the aberration and defocusing of lenses [95]. Therefore, not every time the obtained HRTEM images can be interpreted intuitively as in the cases of DF and BF images. To obtain HRTEM images, i) the samples need to be very thin to avoid inelastic scattering of the electrons, ii) the electron beam need to be aligned precisely along the zone axis [95], this can be done by centering the crossover of Kikuchi lines to the center of the viewing screen see Figure 13, ii) the objective aperture is maximally opened to select as many diffracted beams as possible.
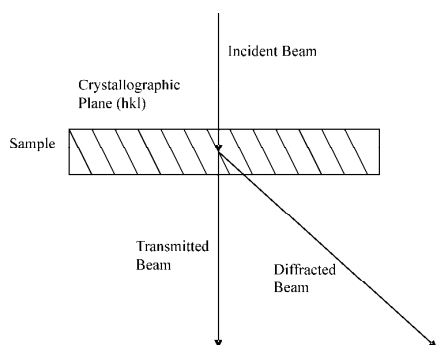

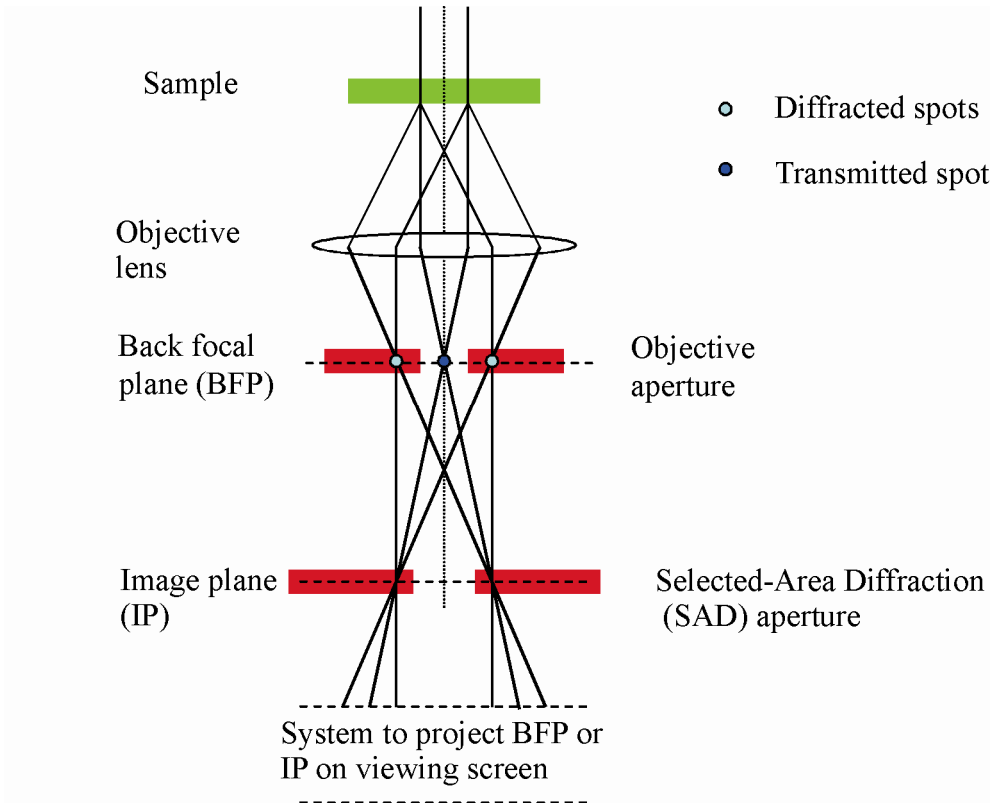**Figure 11. Electron beams in TEM.**

Figure 12. Simplified scheme describing the working principle of TEM.
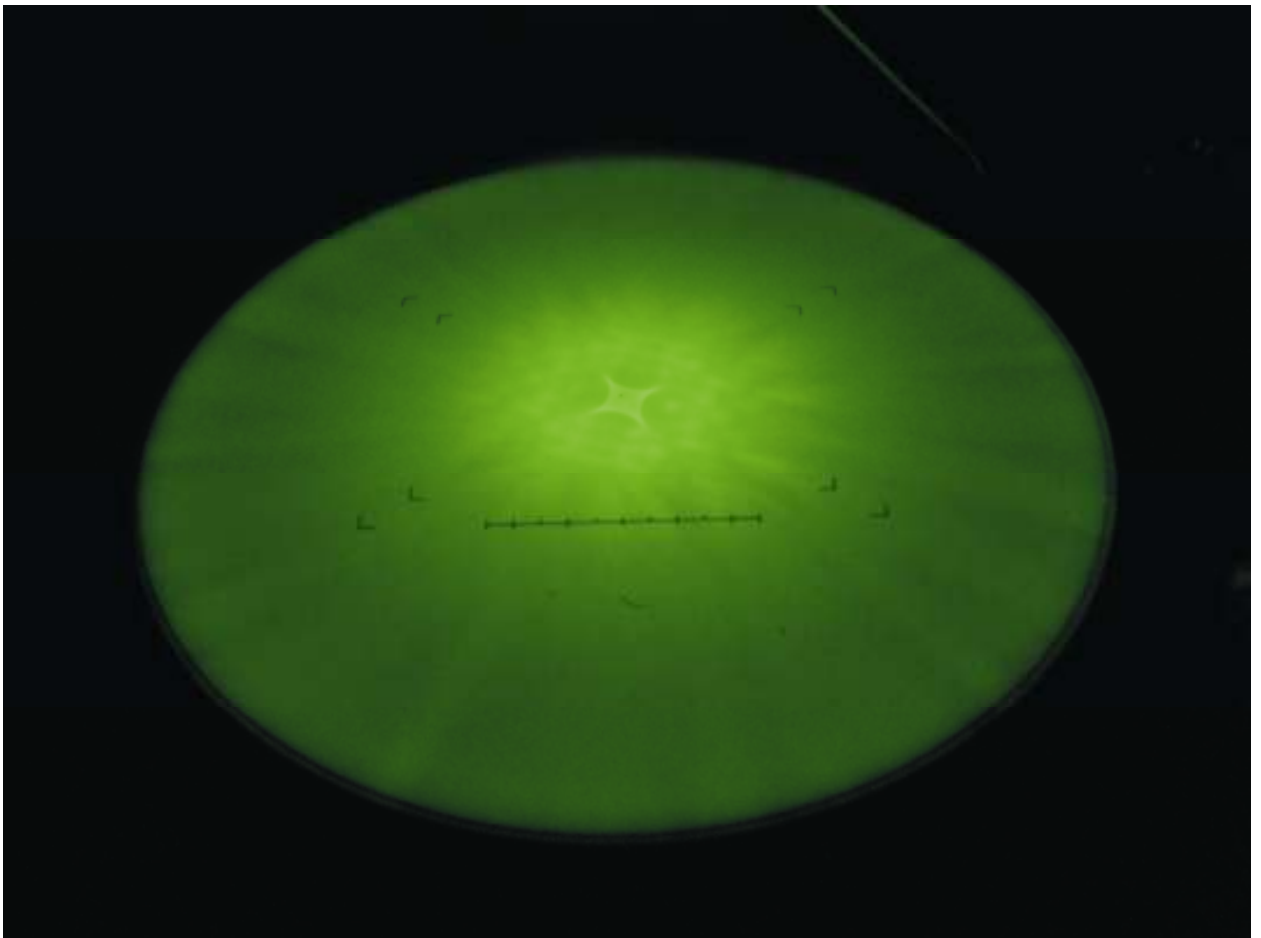
Sample

Objective lens

Back focal plane (BFP)

Objective aperture

Image plane (IP)

Selected-Area Diffraction (SAD) aperture

System to project BFP or IP on viewing screen

○ Diffracted spots

● Transmitted spot

Figure 13. Crossover of Kikuchi lines was placed in the center of the viewing screen. The image was taken in the batch 2 RT 8 x 10^{14} ions/cm^2 sample.

In the current thesis, TEM was performed to study the defects in the Sn$^+$ implanted layer of ZnO wafers. The images were taken either by JEOL JEM-2100F or JEOL JEM-2010F TEMs. The working acceleration voltage in both TEMs was 200 keV.

2.2.8   Scanning transmission electron microscopy (STEM)

Employing the same post-sample lens system but differing from conventional TEM (CTEM), scanning transmission electron microscopy (STEM) utilized a highly-convergent electron beam to probe a sample instead of a broad (or parallel) beam and the probe is scanned across the sample instead of static imaging [95]. While scanning, the intensity of electrons emerging from a small area on the sample is registered by means of a detector, in that sense STEM is similar to scanning electron microscopy (SEM). The detector is placed on the plane conjugate to BFP of the objective lens [95]. Depending on the position and shape of the detector, images can be obtained in BF, DF, annular dark field ADF, and high-angle annular dark field HAADF modes [95]. In the BF mode, the detector is placed on the optic axis to register the transmitted beam, in the DF off the optic axis to register diffracted beams (see Figure 14). In the ADF mode, the detector possesses an annular shape and registers diffracted beams even though its center is aligned on the optic axis (see Figure 14). In the HAADF, diffracted beams, which make large angles with the optic axis, are registered by the annular-shaped detector. Resolution of STEM is not determined by the aberration of the objective lens as in the case of CTEM but by the probe size, and STEM is sensitive to atomic numbers of the atoms that constitute the sample [95]. These are the major advantages of STEM in comparison with HRTEM.
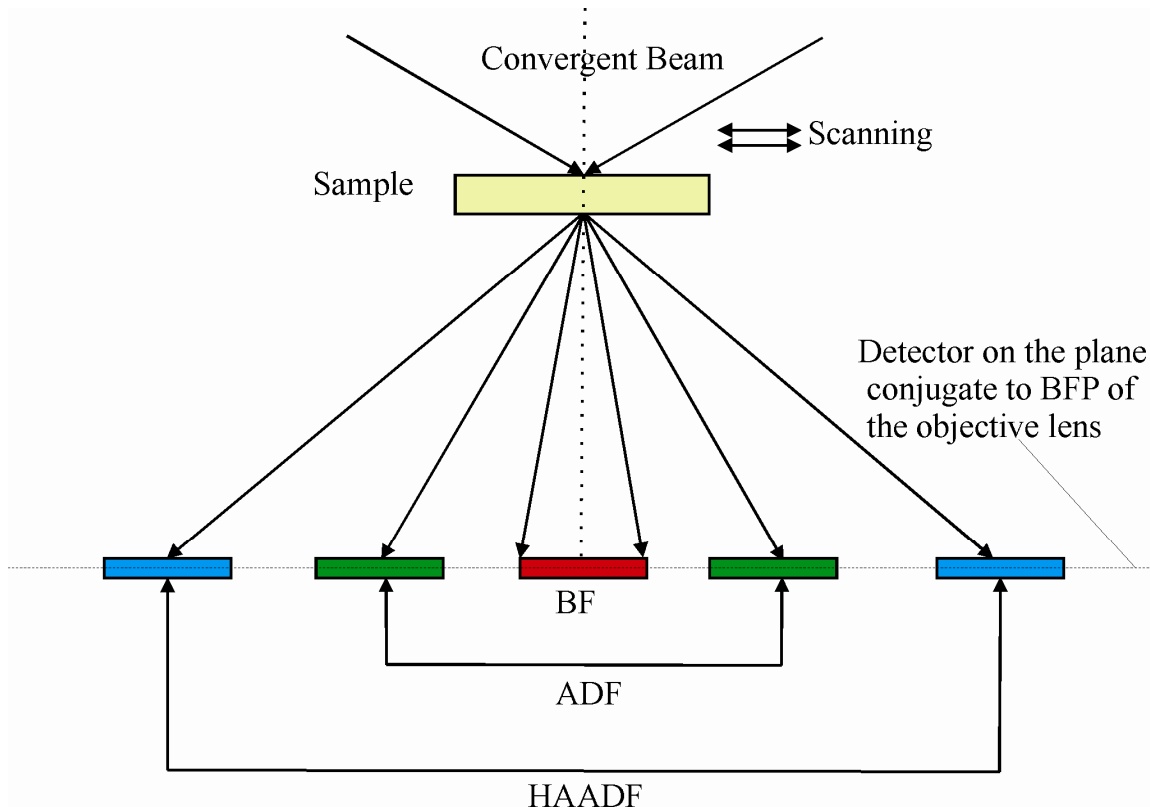
Figure 14. Simplified scheme describing the working principle of STEM.

In this thesis, STEM was utilized to take BF images of the implanted layer in the ZnO wafers. The images were compared to the distribution of elements taken by EDS. The STEM system was incorporated to the JEOL JEM-2100F TEM.

2.2.9   X-ray energy dispersive spectroscopy (EDS)

The composition of interested materials can be analyzed by means of X-ray Energy dispersive spectroscopy (EDS) technique. In EDS, high energy electrons (from a few keV to hundreds of keV) bombard an interested sample. Interaction of these electrons with the constituents of the materials can produce continuum and characteristic X-rays [95, 97]. Continuum X-rays, also called Bremssrahlung X-rays, result from deceleration of the incident electrons [97] by the Coulombic field of the sample atoms. Bremssrahlung X-ray energy can vary in the range from zero to the energy of incident electrons [97]. The incident electrons can also displace the electrons in the inner shells of the sample atoms leaving vacancies in the inner shells (see Figure 15). As the electrons from the outer shells fill the vacancies, characteristic X-rays are emitted from the sample. The photon energies of the characteristic X-rays are equal to the differences in energy of the outer shells and the inner shells and therefore are unique for each element. Registration of these characteristic X-ray photons can determine i) which elements are available in the sample, qualitatively speaking and ii) atomic percentages of the elements, quantitatively

34

speaking. Nowadays, energy dispersive spectrometers are routinely incorporated in scanning electron microscopes (SEMs) and transmission electron microscopes (TEMs), which make SEM and TEM analysis more powerful. Especially in TEM, mapping of different elements in the interested region of the sample can be readily performed. Namely, an image of the interested region is taken by TEM or STEM; subsequently, the distribution of various elements in the region is measured by EDS. However, the atomic percent of constituents should be larger than 1-2 % to be observable in conventional EDSs [97].
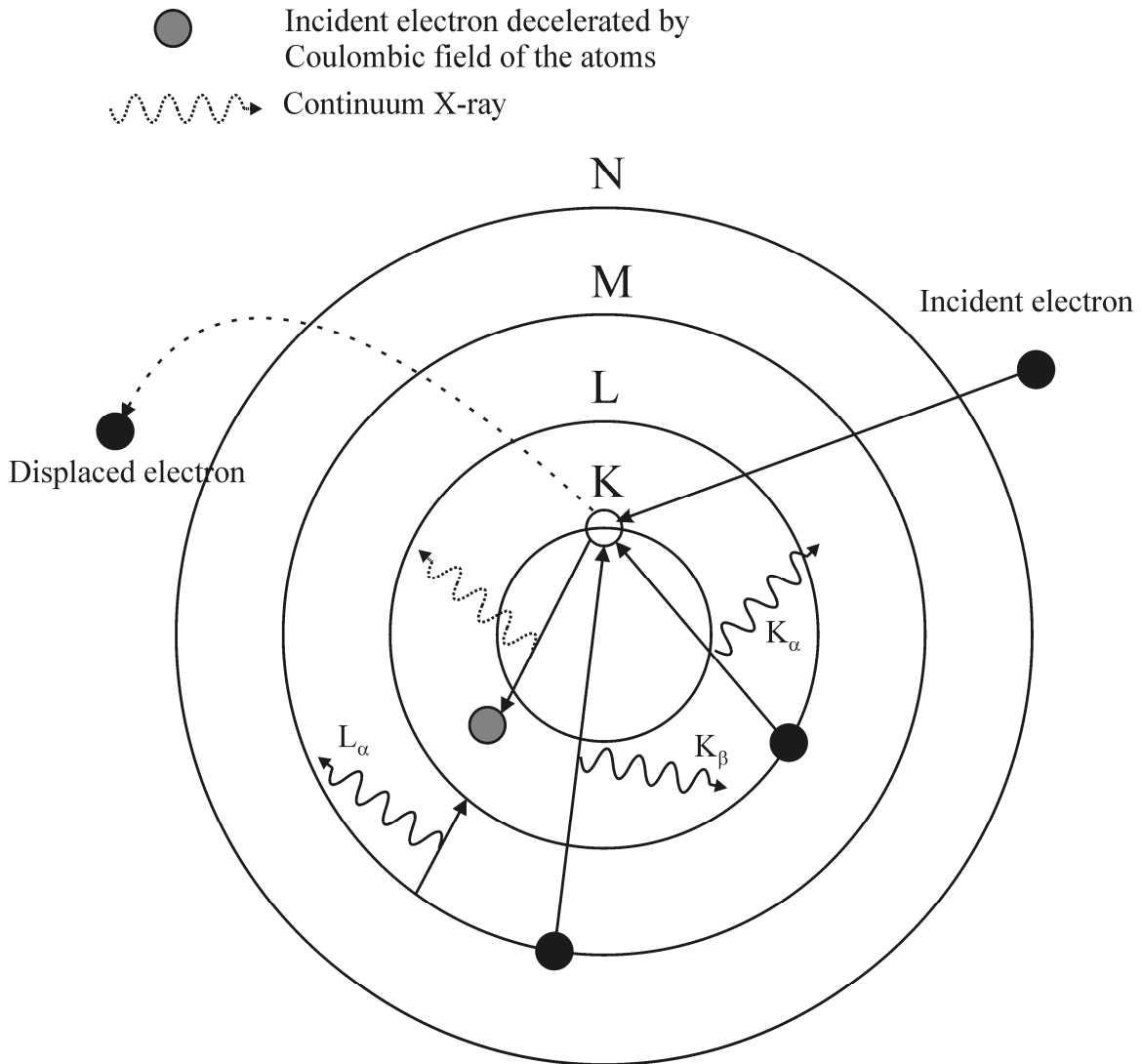

Figure 15. Production of continuum and characteristic X-rays when the sample is bombarded by high energy electrons.

In this thesis, the EDS was performed to search for possible variation of relative Zn and O atomic percent ration in the implanted layer compared to the unimplanted layer. This information would be helpful for judgment of deep level PL origins. The EDS was incorporated in the TEM,

whose details were described in section 2.3.7.2. The EDS detector was cooled by Peltier elements.

3 Photoluminescence of an $Al_{0.5}Ga_{0.5}As/GaAs$ MQW in the temperature range from 5 to 400 K

3.1 The photoluminescence spectra and the temperature dependence of peak positions.

The PL spectra from the MQW are shown in Figure 16. At 5 K, 3 peaks were observed at 1.518, 1.565, and 1.572 eV. At this temperature, the 1.572 eV peak had the highest intensity. As the temperature was increased, an additional peak appeared on the high-energy side of the strongest peak. At 50 K, four separate peaks can be distinguished; they were denoted as peak 1, peak 2, peak 3, and peak 4 in order of increasing energy. The energy difference between peak 4 and peak 3 at 50 K was 15 meV.
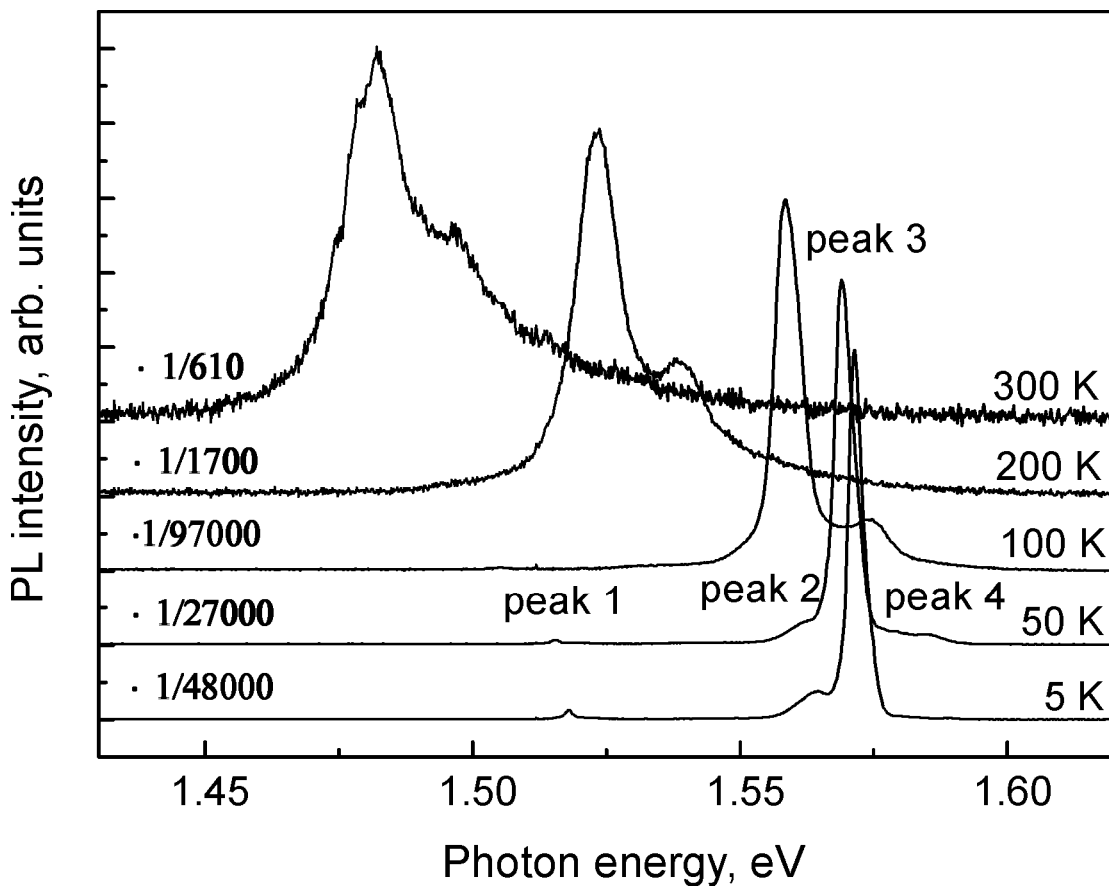

Figure 16. PL spectra of the $Al_{0.5}Ga_{0.5}As/GaAs$ MQW at different temperatures.

In Figure 17, the energy of each peak is plotted as a function of temperature and compared to the bulk GaAs band gap energy, which is described by the formula [98]: $E_g(T) = 1.519 - 5.405 \times 10^{-4} \times T^2 / (T + 204)$, where $E_g(T)$ is the band gap energy measured in eV at T K. It can be seen that the curves for peaks 1, 3, and 4 follow the general shape of the bulk GaAs band gap energy curve, shown by the dashed line. The curve for peak 1 is very close

to the bulk GaAs band gap energy curve, and can therefore be attributed to PL from the GaAs substrate. In addition, peaks 3 and 4 can be attributed to the $1e-1hh$ and $1e-1lh$ transitions[24, 99], respectively. Figure 2 also shows the calculated energies for the $1e-1hh$ (solid line) and $1e-1lh$ (dotted line) transitions in an $Al_{0.5}Ga_{0.5}As/GaAs$ MQW with a well width of 9.6 nm. The calculations were carried out based on the Kronig-Penney model. The calculations are described in the next section.
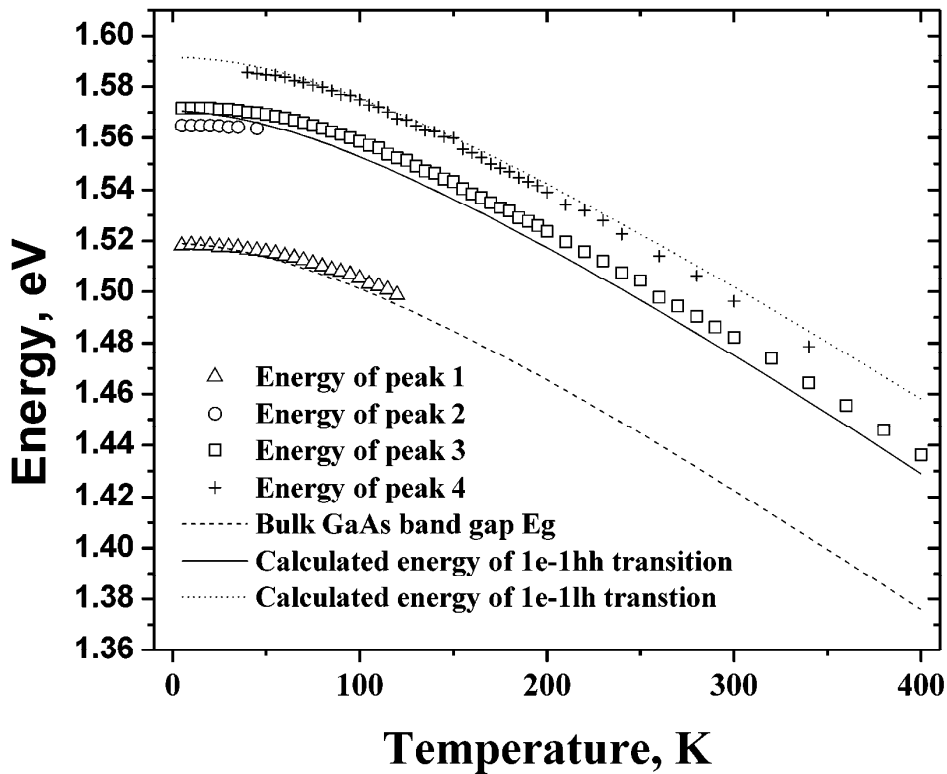

Figure 17. Energies of peaks 1, 2, 3, 4, the bulk GaAs band gap, and the calculated *1e-1hh, 1e-1lh* transitions versus temperature.

3.2 The Kronig-Penney fits

Figure 18 shows the energy scheme of an $Al_{0.5}Ga_{0.5}As/GaAs$ QW. For simplicity, in the Kronig-Penney model it is considered that the potential barrier possesses the rectangle shape.
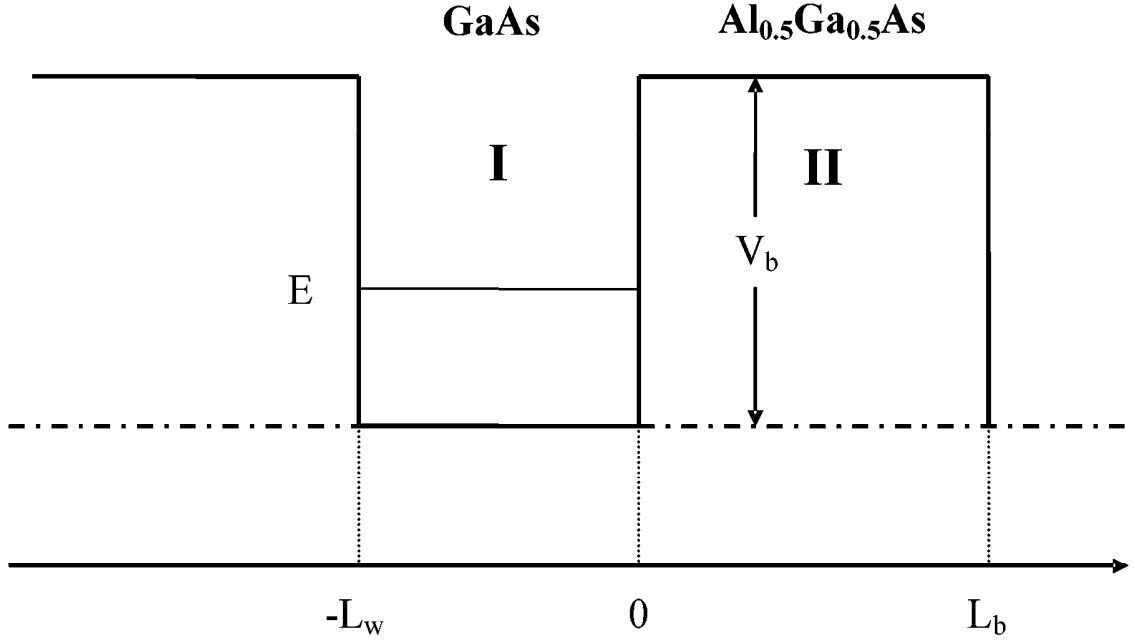
GaAs   **Al$_{0.5}$Ga$_{0.5}$As**

Figure 18. Energy scheme of an Al$_{0.5}$Ga$_{0.5}$As/GaAs QW

Time-independent Schrödinger equations for the wave functions of the carrier (electron)

in area I: $-\dfrac{\hbar^2}{2m_w}\dfrac{d^2\psi_I(x)}{dx^2} - E\psi_I(x) = 0$, where m_w - mass of a charge carrier (electrons or holes) in the well.

in area II: $-\dfrac{\hbar^2}{2m_b}\dfrac{d^2\psi_{II}(x)}{dx^2} + (V_b - E)\psi_{II}(x) = 0$, where m_b - mass of a charge carrier (electrons or holes) in the barrier.

Solutions of those equations are:

in area I: $\psi_I(x) = A_1\cos(\alpha x) + B_1\sin(\alpha x)$, where $\alpha = \dfrac{\sqrt{2m_w E}}{\hbar}$.

in area II: $\psi_{II}(x) = A_2\cosh(\beta x) + B_2\sinh(\beta x)$, where $\beta = \dfrac{\sqrt{2m_b(V_b - E)}}{\hbar}$.

For the sake of convenience, axis x was set as shown in the Figure 18. As the results, boundary conditions would be:

(1): $\psi_I(0) = \psi_{II}(0) \rightarrow A_1 = A_2$ (because the wave functions should be continuous at $x = 0$)

(2): $\psi'_I(0) = \psi'_{II}(0) \rightarrow \alpha B_1 = \beta B_2$ (because the first derivatives of the wave functions should be continuous at $x = 0$)

$\rightarrow \psi_{II}(x) = A_1\cosh(\beta x) + \dfrac{\alpha}{\beta}B_1\sinh(\beta x)$

and periodical conditions of wave functions:

(3): $\psi_I(-L_w) = \psi_{II}(L_b) \rightarrow A_1 \cos(\alpha L_w) - B_1 \sin(\alpha L_w) = A_1 \cosh(\beta L_b) + \dfrac{\alpha}{\beta} B_1 \sinh(\beta L_b)$

(4): $\psi'_I(-L_w) = \psi'_{II}(L_b) \rightarrow \alpha A_1 \sin(\alpha L_w) + \alpha B_1 \cos(\alpha L_w) = \beta A_1 \sinh(\beta L_b) + \alpha B_1 \cosh(\beta L_b)$

So we have a system of linear equations for A_1 and B_1:

$$\begin{cases} A_1(\beta \cos(\alpha L_w) - \beta \cosh(\beta L_b)) - B_1(\beta \sin(\alpha L_w) + \alpha \sinh(\beta L_b)) = 0 \\ A_1((\alpha \sin(\alpha L_w) - \beta \sinh(\beta L_b)) + B_1(\alpha \cos(\alpha L_w) - \alpha \cosh(\beta L_b)) = 0 \end{cases}$$

Since this system should have an infinite number of roots, because the wave functions may differ from each other by a multiply factor, so the determinant :

$$\begin{vmatrix} \beta \cos(\alpha L_w) - \beta \cosh(\beta L_b) & -(\beta \sin(\alpha L_w) + \alpha \sinh(\beta L_b)) \\ (\alpha \sin(\alpha L_w) - \beta \sinh(\beta L_b) & \alpha \cos(\alpha L_w) - \alpha \cosh(\beta L_b) \end{vmatrix}$$

should be equal to zero. From that, the following equation can be obtained to define the energy level of electrons or holes in the QW:

$$\frac{\beta^2 - \alpha^2}{2\alpha\beta} \sin(\alpha L_w) \sinh(\beta L_b) + \cos(\alpha L_w) \cosh(\beta L_b) - 1 = 0 \qquad (2)$$

Strictly speaking, equation (2) slightly differs from the equation normally quoted in textbooks, for examples, [100]. Namely, instead of simple " -1 ", the last term is usually written as " $-\cos[k(L_w + L_b)]$ ". The difference results from the difference in boundary conditions. In the textbook [100], the wave function at $-L_w$ may differ from that at $-L_b$ by a phase factor, e.g

$\psi(-L_w) = e^{ik(L_w + L_b)} \psi(L_b)$, where $k = \dfrac{2\pi r}{N(L_w + L_b)}$, $r = 0,1,2,...$ By selecting $r = 0$, the term

" $-\cos[k(L_w + L_b)]$ " becomes " -1 " as in Eq. (2). In practice, the results of calculation did not strongly depend on this term because $\sinh(\beta L_b)$ and $\cosh(\beta L_b)$ are normally much larger than unity, hence, the first and the second terms normally are much larger than the last term, which can be neglected.

The values of the band offsets, effective light hole masses, and effective electron masses were derived from [101] as follows:

$\Delta E_c(T) = \Delta E_c(2) + (T-2) \times [\Delta E_c(300) - \Delta E_c(2)]/298$

where $\Delta E_c(T)$, $\Delta E_c(2)$, and $\Delta E_c(300)$ are the conduction band offset at T , 2, and 300 K, respectively. According to [101], $\Delta E_c(2)$ and $\Delta E_c(300)$ were calculated by placing $x = 0.5$ into the formulae: $\Delta E_c(x)_{T=2K} = (0.9456x + 0.1288x^2)$ (eV) and

$\Delta E_c(x)_{T=300K} = (0.805x + 0.217x^2)$ (eV) for the conduction band offset of the Al$_{0.5}$Ga$_{0.5}$As/GaAs quantum well at 2 and 300 K, respectively.

$$\Delta E_v(T) = \Delta E_v(2) + (T-2) \times [\Delta E_v(300) - \Delta E_v(2)]/298$$

where $\Delta E_v(T)$, $\Delta E_v(2)$, and $\Delta E_v(300)$ are the valence band offsets at T, 2, and 300 K, respectively. According to [101], $\Delta E_v(2)$ and $\Delta E_v(300)$ were calculated by placing $x = 0.5$ into the formulae: $\Delta E_v(x)_{T=2K} = (0.4145x + 0.0912x^2)$ (eV) and $\Delta E_v(x)_{T=300K} = (0.350x + 0.153x^2)$ (eV) for the valence band offset of the Al$_{0.5}$Ga$_{0.5}$As/GaAs quantum well at 2 and 300 K, respectively.

$$m_{lh(GaAs)}(T) = m_0 \times (0.0951 - \frac{3.902 \times 10^{-5}}{T+204} T^2)$$

where $m_{lh(GaAs)}(T)$ is an effective GaAs light hole mass at T K and m_0 is a free electron mass.

$$m_{lh(AlGaAs)}(T) = m_{lh(AlGaAs)}(2) + (T-2) \times [m_{lh(AlGaAs)}(300) - m_{lh(AlGaAs)}(2)]/298$$

where $m_{lh(AlGaAs)}(T)$, $m_{lh(AlGaAs)}(2)$, and $m_{lh(AlGaAs)}(300)$ are the effective light hole masses of the barrier Al$_{0.5}$Ga$_{0.5}$As/GaAs at T, 2, and 300 K, respectively. According to [101], $m_{lh(AlGaAs)}(2)$ and $m_{lh(AlGaAs)}(300)$ were calculated by placing $x = 0.5$ into the formulae:

$$m_{lh(AlGaAs)}(x)_{T=2K} = m_0(0.0951 + 0.0441x + 0.0097x^2) \quad \text{and}$$

$m_{lh(AlGaAs)}(x)_{T=300K} = m_0(0.088 + 0.372x + 0.0163x^2)$ for the effective light hole masses of the Al$_{0.5}$Ga$_{0.5}$As barrier at 2 and 300 K, respectively.

$$m_{e(GaAs)}(T) = m_0 \times (0.0665 - \frac{1.848 \times 10^{-5}}{T+204} T^2)$$

where $m_{e(GaAs)}(T)$ is an effective GaAs electron mass at T K and m_0 is a free electron mass.

$$m_{e(AlGaAs)}(T) = m_{e(AlGaAs)}(2) + (T-2) \times [m_{e(AlGaAs)}(300) - m_{e(AlGaAs)}(2)]/298$$

where $m_{e(AlGaAs)}(T)$, $m_{e(AlGaAs)}(2)$, and $m_{e(AlGaAs)}(300)$ are the effective light hole masses of the barrier Al$_{0.5}$Ga$_{0.5}$As/GaAs at T, 2, and 300 K, respectively. According to [101], $m_{e(AlGaAs)}(2)$ and $m_{e(AlGaAs)}(300)$ were calculated by placing $x = 0.5$ into the formulae:

$$m_{e(AlGaAs)}(x)_{T=2K} = m_0(0.0665 + 0.1006x + 0.0137x^2) \quad \text{and}$$

$m_{e(AlGaAs)}(x)_{T=300K} = m_0(0.0632 + 0.0856x + 0.0231x^2)$ for the effective electron masses of the Al$_{0.5}$Ga$_{0.5}$As barrier at 2 and 300 K, respectively.

Due to the lack of temperature dependences of the effective heavy hole masses in literature, the effective heavy hole masses of $Al_{0.5}Ga_{0.5}As$/GaAs were considered as constants in the whole temperature range from 5 to 400 K. The values of the effective heavy hole masses of GaAs and $Al_{0.5}Ga_{0.5}As$ were calculated by placing $x = 0$ and $x = 0.5$ into the formula: $m_{hh}(x) = m_0(0.51 + 0.25x)$ given in [21]. Note that variation in the effective heavy hole masses did not cause a significant change in the calculated results of the $1e - 1hh$ and $1e - 1lh$ transitions. These parameters (the band offsets and effective masses) at temperatures in the range from 5 to 400 K were saved in a list. Subsequently, a program was written in Delphi 7. This program read the parameters in the list as an input, and solved the equation (2) numerically. The barrier width was taken to be 10 nm, according to the specification of the sample. In fact, the calculated results did not strongly depend on the barrier width. The well width was varied so that the calculated $1e - 1hh$ and $1e - 1lh$ transitions best fitted the experimental data of peaks 3 and 4. The well width of 9.6 (± 0.6) nm corresponding to 17 (± 1) monolayers provided the best fit. The lists of parameters and the calculated $1e - 1hh$ and $1e - 1lh$ transitions, interface of the program, are provided in the Appendix A. The source code of the whole program is too long (35 pages) to include in this thesis, merely the main function responsible for the energy level calculation is included in the Appendix. If one needs the whole source codes and the program itself, please, contact with me by the e-mail: giang2110@gmail.com.

3.3 PLE spectrum

Figure 19 shows the excitation power of the Ti: sapphire laser as a function of excitation energy. This dependence was utilized to normalize the PL spectra measured at 5 K. Figure 19 also illustrates the PLE spectrum detected from low-energy shoulder of peak 3 (see Figure 19). In the PLE spectrum, three peaks, which are distinguished from the excitation power line, were observed at 1.572, 1.589, and 1.714 eV. The calculated energies of the $1e - 1hh$, $1e - 1lh$, and $2e - 2hh$ were 1.570, 1.591, and 1.719 eV, according to the Kronig-Penney model (see section 3.2). Therefore, the three peaks were attributed to $1e - 1hh$, $1e - 1lh$, and $2e - 2hh$ free excitons (FXs). Note that in the Kronig-Penney calculation the exciton binding energy was not considered.
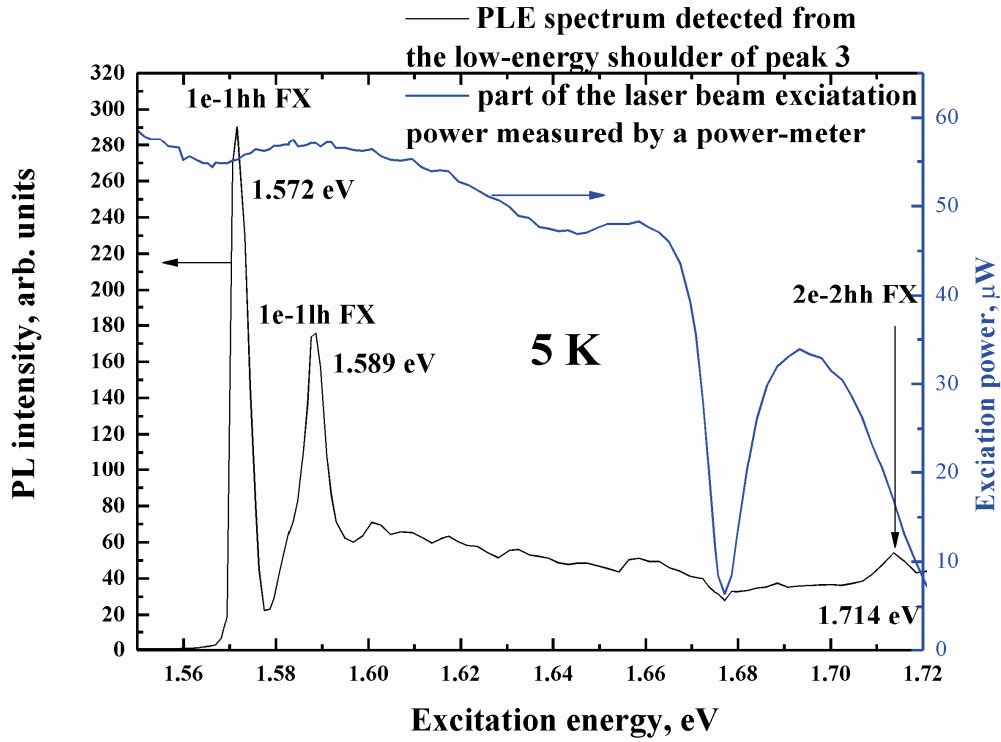
Figure 19. PLE spectrum detected at low-energy shoulder of peak 3 and the Ti: sapphire laser excitation power as a function of excitation energy.

A detailed view of the PLE spectrum of peak 3 is shown in (Figure 20). Another feature appeared between the $1e-1hh$ and $1e-1lh$ FXs. Previously, in [27, 28] this feature was assigned to the excited $2s$ state or the onset of the continuum of the of the $1e-1hh$ FX. Following the approach of Miller *et al.* [28], the excited $2s$ state of the $1e-1hh$ FX was determined at the middle point of the rising part of the feature. Thus, the energy of 1.5809 eV was obtained for the $2s$ state of the $1e-1hh$ FX. According to the hydrogenic model, the difference in energy of the $1s$ and $2s$ state of a free exciton E_{2s-1s} and the exciton binding energy E_b by the formula:
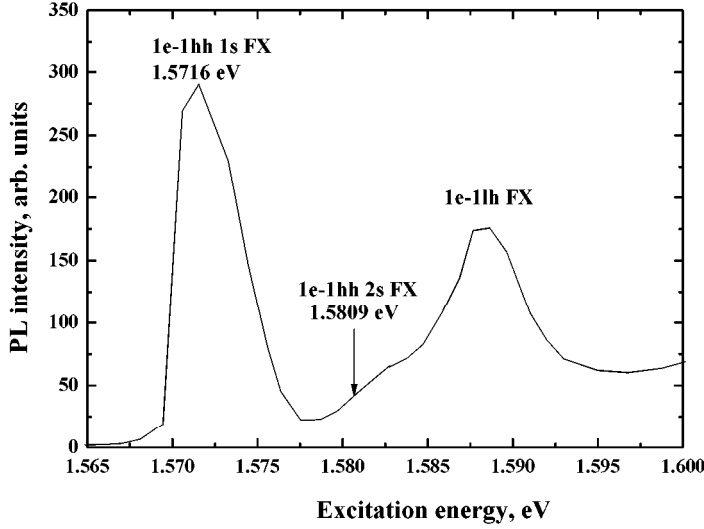
Figure 20. Detailed view of the PLE spectrum from peak 3, which shows the 2s excited level or the onset of the 1e-1hh exciton.

$$E_{2s-1s} = \frac{3}{4} E_b \qquad\qquad (3)$$

However, an exciton in a QW cannot be considered as a 3D-exciton so the ratio E_{2s-1s} / E_b should differ from 0.75. A model treating an excitons in a QW as a 2D-exciton has been conducted by Miller *et al.* [28]. The model provided a value of 0.84 for the ratio E_{2s-1s} / E_b in a 10-nm-well-thickness $Al_{0.37}Ga_{0.63}As$/GaAs QW. Utilizing the value of 0.795 for the ratio E_{2s-1s} / E_b, I obtained a value of 11.7 $\pm$ 1 meV for the binding energy of the $1e-1hh$ FX in the current sample. The binding energy error of 1 eV resulted from the errors when determining the exact position of the 2*s* state in the PLE spectrum and the value of the E_{2s-1s} / E_b ratio.

Figure 21 illustrates PLE spectra detected from the low-energy shoulder of peaks 2 and 3. In the PLE spectrum of peak 2, the two FX peaks $1e-1hh$ and $1e-1hh$ were observed at the same energy position. This indicates that the photoluminescence of peaks 2 and 3 is from the same set of quantum wells. In addition, the normalized PL intensity of peak 2 decreased drastically when the excitation energy became less than the energy of $1e-1hh$ FEs. This suggests that peak 2 is the result of recombination of excitons bound to impurities since for excitation energies lower than the energy of the $1e-1hh$ FX, exciton formation seems to decrease, leading to a considerable reduction in the PL intensity of impurity-bound excitons.
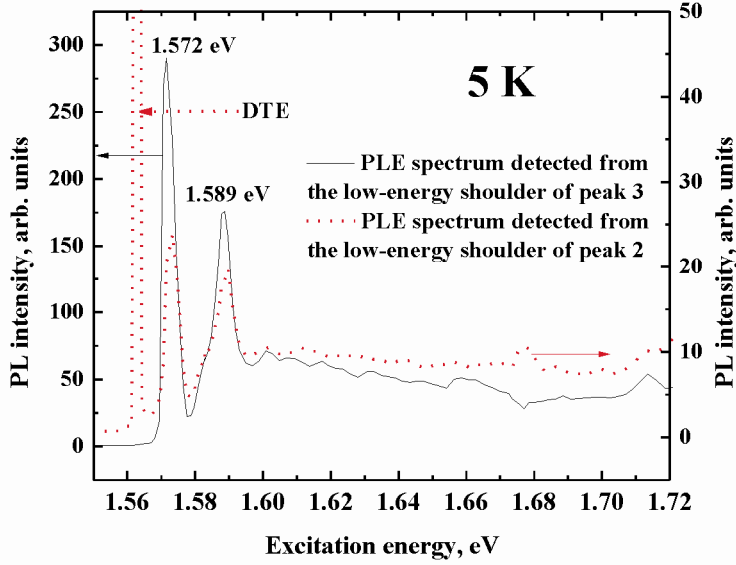
Figure 21. PLE spectra detected at low energy shoulders of peak 3 and peak 2.

3.4 The quenching and Arrhenius fit

The temperature dependence of PL intensity is usually fitted with the formula[23, 25, 102]:

$$I = I_0 \, /[1 + A \exp(-E_a \, / kT)] \tag{4}$$

where I and I_0 are PL intensities at T K and as temperature approaches 0 K, respectively; A is a temperature-independent constant, and E_a is an activation energy. This formula was first proposed by Williams and Eyring [103] in a slightly different form. Originally, the meaning of E_a was the activation energy necessary for an electron to "radiationlessly" surmount a barrier between a "metastable" state and a "normal" state. The "metastable state" was referred to as an electron trap, whereas the "normal state" probably implied an energy level in the valence band. Later, numerous studies interpreted this activation energy E_a as dissociation energies of various exciton complexes [23, 25, 102, 104, 105]. Jiang *et al.* [23] and Zhongying *et al.* [25] have considered E_a as an exciton binding energy in AlGaAs/GaAs quantum wells.

In the current study, thermal quenching of the integrated PL intensity of the $1e - 1hh$ transition is depicted in (Figure 22). The experimental data in the temperature range 5–120 K were fitted using the expression (4) to obtain the activation energy $E_a = 12.5 \pm 0.7$ meV. This activation energy is close to the binding energy of 11.7 ± 1 meV of the $1e - 1hh$ FX determined previously in the PLE spectra (see Figure 20).
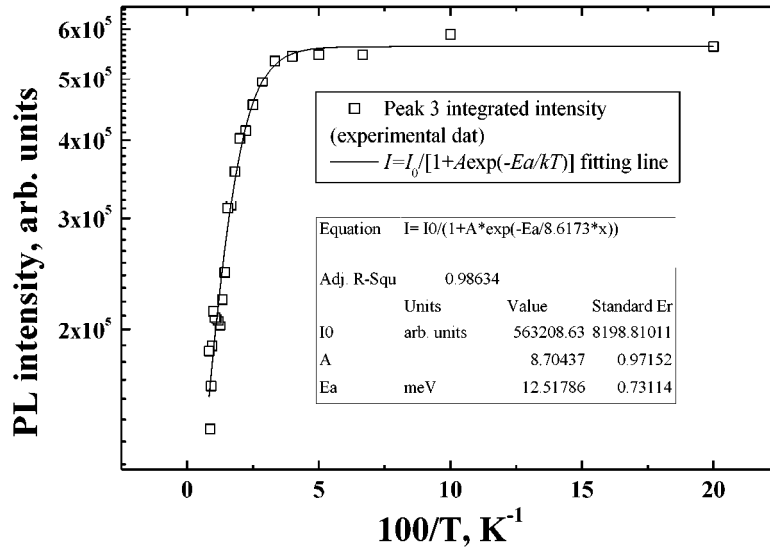
45

Figure 22. Temperature dependence of the peak 3 integrated intensity in the range from 5 to 120 K. The experimental data (empty squares) were fitted with the formula $I=I_0/[1+Aexp(-E_a/kT)]$. The solid line shows the least-square fit.

It should be noted that the activation energies obtained from least-square fits fluctuated when the range of data (or range of temperature) varied, as illustrated in Table 2. The 5-120 K range was selected because at 120 K the t value and the energy difference $E_3 - E_g$ started to stabilize. The temperature of 120 ± 20 K is equivalent to the thermal energy of 10.3 ± 1.7 eV. This energy is also close to the binding energy 11.7 ± 1 meV and the activation energy 12.5 ± 0.7 meV determined before. This closeness once again supports the conclusion on the dissociation of the $1e - 1hh$ FX in the temperature range from 5 to 120 K.

Table 2. Activation energies obtained by fitting the temperature dependence of the peak 3 integrated intensity with the formula: $I=I_0/[1+Aexp(-E_a/kT)]$. Activation energies fluctuated with the selected range of temperature.

Range of temperature	E_a	Error
K	meV	meV
5-80	14.3377	1.08525
5- 95	13.2836	0.85087
5-120	12.5179	0.73114
5-160	12.9956	0.67575
5-200	14.1121	0.68045
Average	13.4494	
Stadard Error	0.76313	

3.5 The ratio of intensities of the $1e-1lh$ and $1e-1hh$ transitions

Figure 23 depicts the energy diagram for calculation of the ratio I_{lh}/I_{hh}, where I_{lh} and I_{hh} are the intensities of peaks 4 (the $1e-1lh$ transition) and 3 (the $1e-1hh$ transition). Assuming a Boltzmann distribution, $n_h \propto \exp[-(F_v - E_h)/kT]$, where F_v is the nonequilibrium quasi-Fermi level in the valence band and E_h is the hole energy level. As a result, the PL peak intensities of the $1e-1hh$ and $1e-1lh$ transitions are given as $I_{hh} = \alpha_{hh}(T)\exp(-(F_v\text{-}E_{1hh})/kT)$ and $I_{lh} = \alpha_{lh}(T)\exp(-(F_v\text{-}E_{1lh})/kT)$, where E_{1hh}, E_{1lh} are the energies of the $1hh$ and $1lh$ sublevels, respectively, and α_{hh}, α_{lh} are coefficients. Assuming:
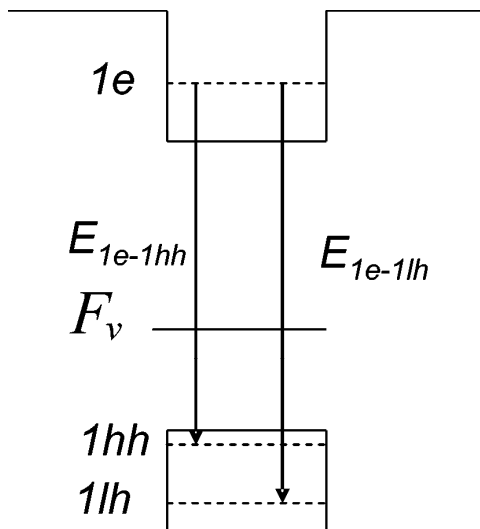

Figure 23. Energy diagram for calculation of the ration Ilh/Ihh.

$$\alpha_{lh}(T)/\alpha_{hh}(T)=1 \qquad\qquad (5)$$

and taking into account the fact that the difference in energy between the $1hh$ and $1lh$ sublevels is equal to that between the $1e-1lh$ and $1e-1hh$ transitions, the ratio I_{lh}/I_{hh} can be written as:

$$I_{lh}/I_{hh}=\exp(-\Delta E/kT) \qquad\qquad (6)$$

where $\Delta E=E_4\text{-}E_3$ and E_3, E_4 are the energies of peaks 3 (the $1e-1hh$ transition) and 4 (the $1e-1lh$ transition), respectively. According to this formula, the ratio I_{lh}/I_{hh} is expected to approach unity as the temperature approach infinity because ΔE has a finite value.

Figure 24 shows the ratio I_{lh}/I_{hh} plotted versus reciprocal temperature with a semi-logarithmic scale. Note that the I_{lh} and I_{hh} were the peak intensities not integrated intensities. As expected, in the semi-logarithmic plot the experimental data make a straight line, which tends to cross the vertical axis at unity. The data are fitted by equation (6) with ΔE calculated from the experimental values for the energies of peaks 3 and 4 not from the Knonig-Penney model. The theoretical curve is a close fit to the experimental data except for the data points at the lowest (40 K) and highest (340 K) temperatures. At 40 K, it is possible that the PL of peak 4 at 1.586 eV was affected by a known defect in the CCD array at 1.590 ± 0.002 eV. At 340 K, the accuracy of the measured PL intensities for peaks 3 and 4 is expected to be poor because of the low signal-to-noise ratio. In general, the data are most reliable in the temperature range 70–260 K, where peaks 3 and 4 are clearly resolved. Figure 5 also shows experimental I_{lh}/I_{hh} data derived from the PL spectra of a 4.2-nm AlAs/4.2-nm GaAs MQW reported by Jiang *et al*. [23]. Note that I_{hh} was the intensity determined at the $1e-1hh$ peak and I_{lh} was the intensity determined at the postion 33 meV above the $1e-1hh$ peak in the PL spectra published by Jiang *et al*. [23]. Again, these data are approximated by equation (6) using the 33 meV energy difference between the $1e-1lh$ and $1e-1hh$ transitions claimed in the reference. The approximation line fits the experimental data well, which suggests that equations (5) and (6) are valid regardless of the barrier aluminum mole factor and the well width. The line made from the data of Jiang *et al*. [23] lies below that from the current study and is steeper because of the larger ΔE, which resulted from i) smaller GaAs well thickness (4.2 nm) and ii) larger band offsets at the AlAs/GaAs interface in comparison with the $Al_{0.5}Ga_{0.5}As$/GaAs interface.
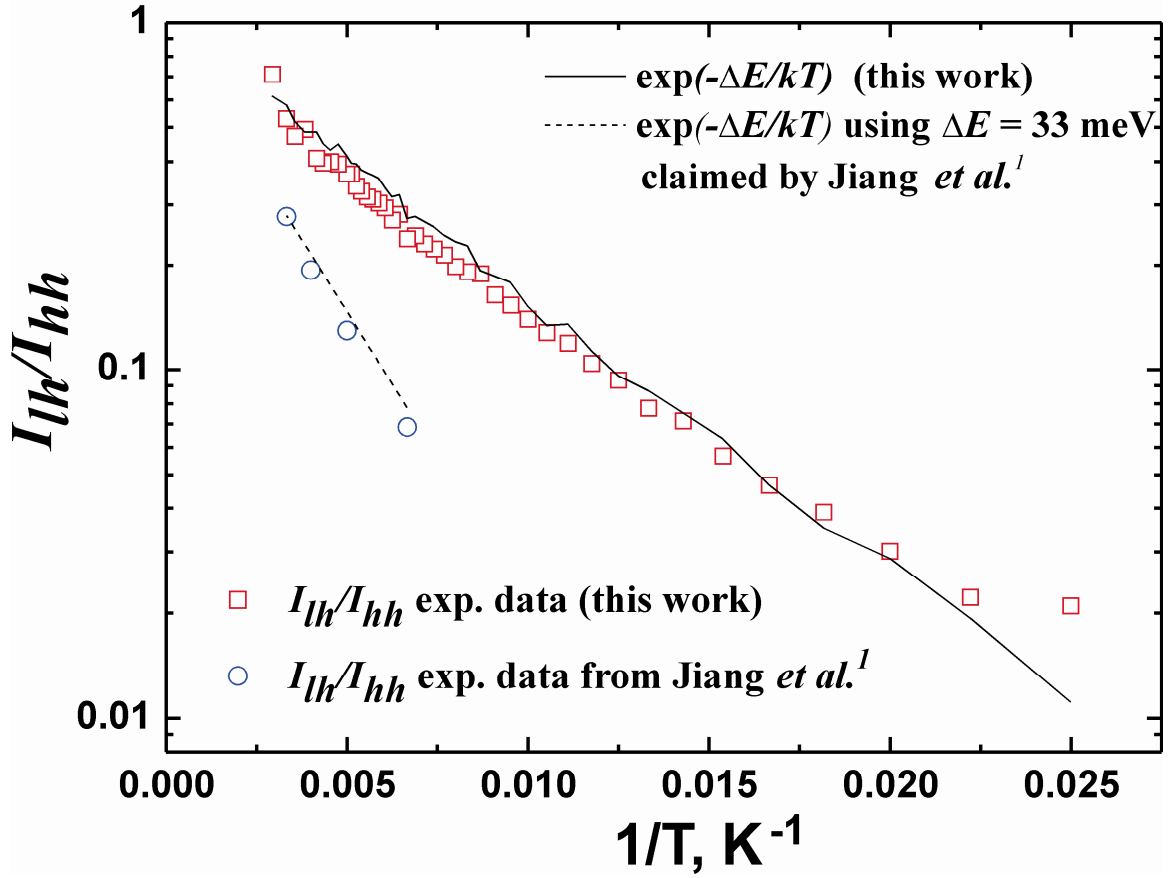
Figure 24. Temperature dependence of the ratio I_{lh}/I_{hh}.

In the case of free-carrier recombination, the assumption that the PL peak intensity is proportional to the hole concentration is reasonable, since PL intensity is proportional to the product of the electron and hole concentrations. For excitonic recombination, this cannot be so readily assumed, because in this case the PL intensity is proportional to the exciton concentration [1]. Since an exciton is an electron-hole pair, the exciton concentration should be proportional to either the electron or hole concentration. To fulfill the charge neutrality condition, the $n=1$ electron concentration should be larger than both the $n=1$ heavy hole concentration and the $n=1$ light hole concentration. Therefore, the exciton concentration should again be proportional to the hole concentration as required. In addition, as the temperature increases, peaks 3 and 4 partly overlap due to thermal broadening. Even though this fact was not considered in the model, equation (6) has proven to be a good approximation for the ratio I_{lh}/I_{hh} at temperatures in the range 50–300 K.

3.6 Excitation dependences

The dependence of PL intensity I_{PL} on excitation power I_{ext} has been readily approximated [25, 29, 106, 107] by the formula:

$$I_{PL} = C \times I_{ext}^t$$

where C and t are constants. Numerous studies [29, 106, 107] have attempted to prove that the underlying recombination process can be determined from the value of the exponent t. According to the model developed by Fouquet and Siegman [29], excitonic recombination results in $t = 1$, free-carrier recombination in $t = 2$, and mixture of excitonic recombination and free-carrier recombination in $1 < t < 2$. The model of Fouquet and Siegman [29] was applied only to the time-integrated photoemission intensity after the sample was shortly excited by a ~250 ps laser pulse. However, the conclusion of the model was quoted in the case of steady-state excitation and photoemission [25, 34]. On the other hand, Schmidt *et al.* [107] and Taguchi *et al.* [106] have developed models for steady-state excitation and photoemission. In those models, the value of t can be larger than 1 even for the excitonic recombination. Nevertheless, the models merely considered the process at low temperatures. As a result, Schmidt *et al.* [107] and Taguchi *et al.* [106] neglected the term related to the non-radiative depopulation of electron concentration, which played an essential role in the argument of Fouquet and Siegman [29]. Thus, at this moment no adequate models have been developed for the steady-state case at both low- and room-temperatures. I consider the model of Fouquet and Siegman more appropriate to apply in the current study because it reflects the monomolecular and bimolecular nature of the excitonic and free-carrier recombination, respectively. Therefore, the conclusion of the model is utilized in this study.

To determine the mechanism of photoemission, the dependence of PL of peak 3 on excitation power was measure in the wide temperature range from 5 to 296 K with small steps from 15 to 20 K. Figure 25 shows some representative PL spectra measured at 100 K. The excitation power was varied more than 2 orders of magnitude at 100 K. In the worst case the excitation was varied at least 1 order of magnitude at 296 K. PL intensity in the center region of peak 3 was integrated.
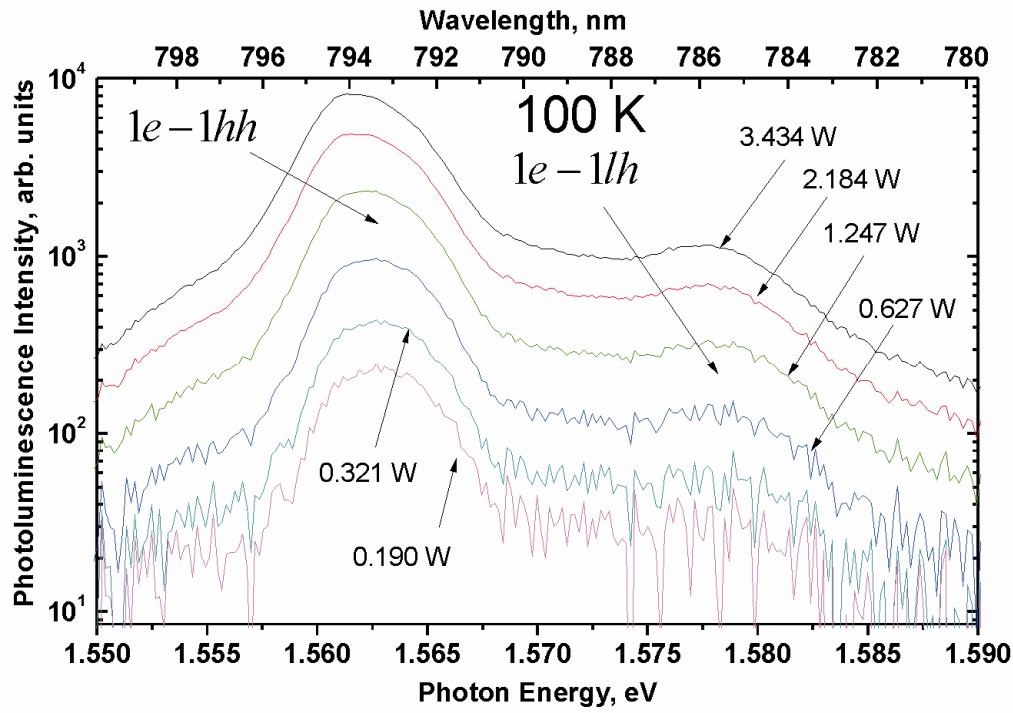
Figure 25. Some representative PL spectra excited with numerous excitation powers. The spectra were measured at 100 K.

In Figure 26, the integrated PL intensity of peak 3 at temperatures of 5, 60, 120, 180, and 296 K is plotted versus excitation power with a double-logarithm scale. The experimental data are fitted by straight lines, whose slopes are equal to the exponent t in the expression $I_{PL} = C \times I_{ext}^{t}$. At 5 K, $t = 1.03$, indicating that the dominant recombination mechanism is excitonic at this temperature. Figure 27(a) illustrates the temperature dependence of the t exponent. As the temperature increases from 5 to 120 ± 20 K, the value of t increases from 1.03 to 1.37 ± 0.5. At temperatures from 120 ± 20 to 300 K, t remains constant at 1.37 ± 0.5. The deviation of the data point at 120 K ($t = 1.29$) from the above trend may have been related to the accuracy of the measurement. The temperature dependence of t suggests that as the temperature increases from 5 to 120 ± 20 K, excitons are dissociated and free-carrier recombination gradually makes a larger contribution to the total PL intensity of the $1e-1hh$ transition. Above 120 ± 20 K, the relative contributions from free-carrier recombination and, thus, excitonic recombination to the total PL intensity do not vary. This appears to validate Hayakawa's conclusions [34] on the presence of two PL recombination mechanisms at room temperature.
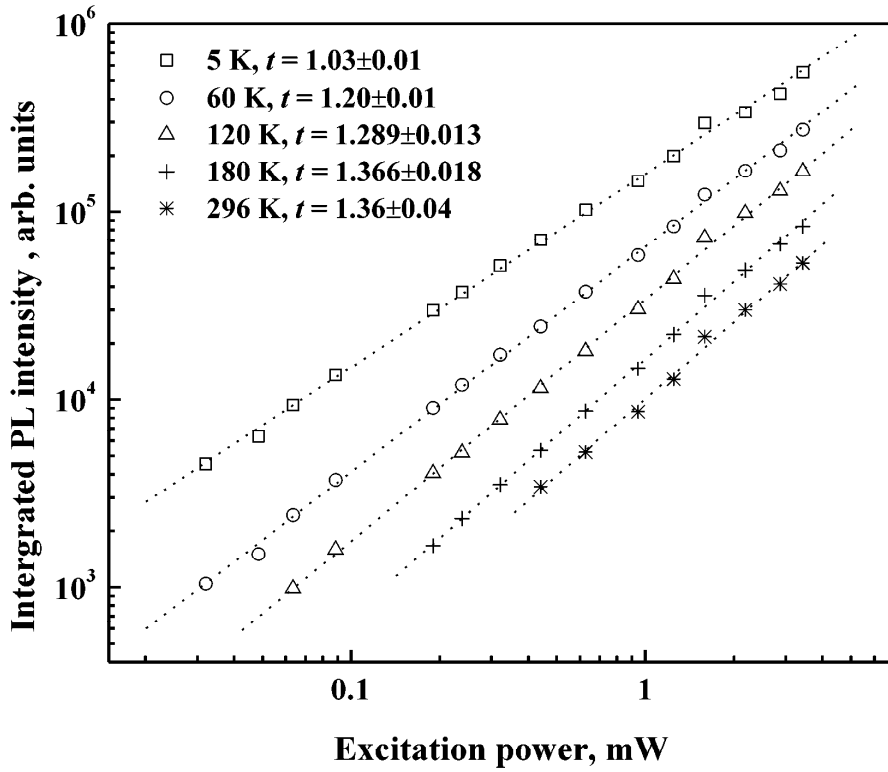
Figure 26. Dependence of integrated PL intensity of peak 3 on excitation power at 5, 60, 120, 180, and 296 K. The exponent t in the expression $I_{PL} = C \times I_{ext}^{t}$ is also shown.
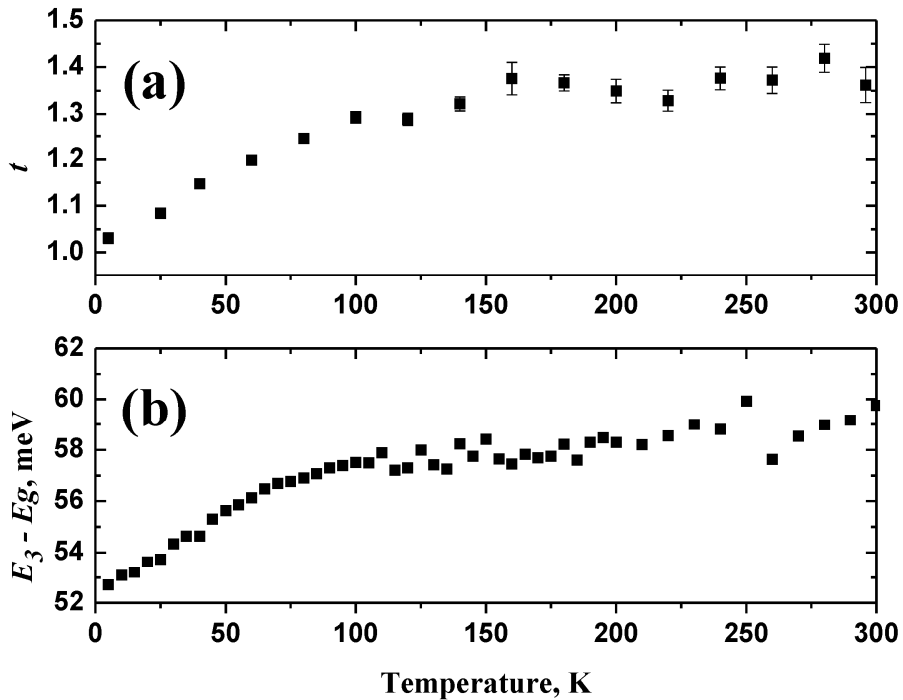

Figure 27. Temperature dependence of (a) the t exponent and (b) energy difference between peak 3 and the bulk GaAs band gap.

A large variance exists in the values of the t exponent reported in the literature. Fouquet and Siegman found that $t = 2$ at room temperature. The values of 1.05 at 11 K and 1.42 at 120 K reported by Zhongying $et\ al.$ [25] are very close to the values 1.03 at 5 K and 1.38 at 160 K found in this study. However, Zhongying $et\ al.$ [25] reported a further increase in t up to 1.91 at 200 K, in contrast to the results described here. In addition, Hayakawa $et\ al.$ [34] reported a t value of 1.21 at 300 K for a 50 Å wide $Al_{0.3}Ga_{0.7}As/GaAs$ MQW. The discrepancy in the published results suggests that the t exponent is sensitive to the measurement conditions. Also, in this study, such sensitivity may have led to unreliability in some of the data points for the t exponent, for example, the one at 120 K. However, this is unlikely to have affected the overall trend observed in Figure 27(a), due to the large experimental dataset in the current study.

Let me denote the difference in energy between peak i ($i = 1,3,4$) and the bulk GaAs band gap as $E_i - E_g$. Figure 27(b) plots the energy difference $E_3 - E_g$ in the temperature range 5–300 K. The shape of the curve is very similar to that of the temperature dependence of the t exponent except for the fact that the former stabilizes at 105 ± 10 K and the latter at 120 ± 20 K. If a single recombination mechanism dominated the PL in the entire 5–300 K temperature range, the energy difference would not be expected to change in that temperature range. The fact that two completely different physical quantities show similar temperature dependence strongly supports the conclusion on the variation of the PL mechanism and on the relative contribution of free-carrier recombination to the total PL intensity. The relative contribution is expected to increase with temperature in the entire 5-300 K temperature range, since excitons are more easily dissociated at higher temperature. However, the observed stabilization of the t exponent and of the energy difference between peak 3 and the bulk GaAs band gap completely contradicts this expectation.

It should be noted that the temperatures 120 ± 20 K and 105 ± 10 K correspond to thermal energies (kT) of 10.4 ± 1.7 meV and 9.0 ± 0.9 meV, respectively. These energies are close to the reported binding energies of the $1e - 1hh$ exciton [10, 12, 26, 30] in AlGaAs/GaAs MQWs with well widths almost identical to that used in this study. As a result, one can speculate that the temperature at which the t exponent and the energy difference $E_3 - E_g$ begin to stabilize may represent the binding energy of the $1e - 1hh$ exciton. However, this leads to difficulties in explaining the fact (data not shown here) that the energy differences $E_1 - E_g$ and $E_4 - E_g$ also increase from 5 to 105 K before becoming constant, as in the case of $E_3 - E_g$. Such similar stabilization temperatures would not be expected since the binding energies of bulk GaAs, $1e - 1hh$, and $1e - 1lh$ excitons are different. For example, the binding energy of bulk GaAs is claimed to be 4 meV [9], whereas the binding energies of $1e - 1hh$ and $1e - 1lh$ excitons in an

Al$_{0.4}$Ga$_{0.6}$As/GaAs quantum well with a width of 9.6 nm were calculated to be 10 and 13 meV [26], respectively. More investigations are needed to clarify this problem.

4 Characteristics of hydrothermal ZnO wafers implanted with 60 keV Sn⁺ ions

4.1 SRIM calculations

The parametters utilized in the simulation are listed as follow.

For the implantation ions: Type: Tin (Sn), Energy: 60 keV, Atomic number: 50, Atomic mass: 119.90 amu, Incident angle: 0 degree.

For the target: The layer thick ness: 5 mm. Layer density: 5.605 g/cm^3. Compound Correction: 1.

> The first target element: Type: Oxygen (O), Atomic number: 8, Atomic mass: 15.99, Atomic Stoichimetry: 0.5 or 50%, Displacement Engergy: 28 eV, Lattice Energy: 3 eV, and Surface Energy: 2 eV.

> The second target element: Type: Zinc (Zn), Atomic number: 30, Atomic mass: 65.39, Atomic Stoichimetry: 0.5 or 50%, Displacement Engergy: 25 eV, Lattice Energy: 3 eV, and Surface Energy: 1.35 eV.

Most parameters were automatically filled in by the SRIM program except for the ion energy of 60 keV, which was applied for this concrete study, and the density of 5.605 g/cm^3, which differed from the SRIM default value of 4.23 g/cm^3. The value of 5.605 g/cm^3 were taken from [37]. In addition, the displacement energies of Zn and O atoms were taken to be 57 eV in [54, 108]. The calculations with the 57 eV displacement energies were conducted and the results were essentially the same as the those calculated with displacement energies of 25 and 28 eV for Zn and O atoms.

Belows are ouput results provided by SRIM after 60000 ions were run.

Figure 28 shows the stopped positions of i) Sn ions and ii) the recoils Zn (moving atoms: cyan dots and stopped atoms: violet dots) and O (moving atoms: orange dots and stopped atoms: green dots). The maximum range the ions can reach is approximately 53 nm. It can be observed that some recoils can reach as far as approximately 93 nm, which is much further than the ions can.
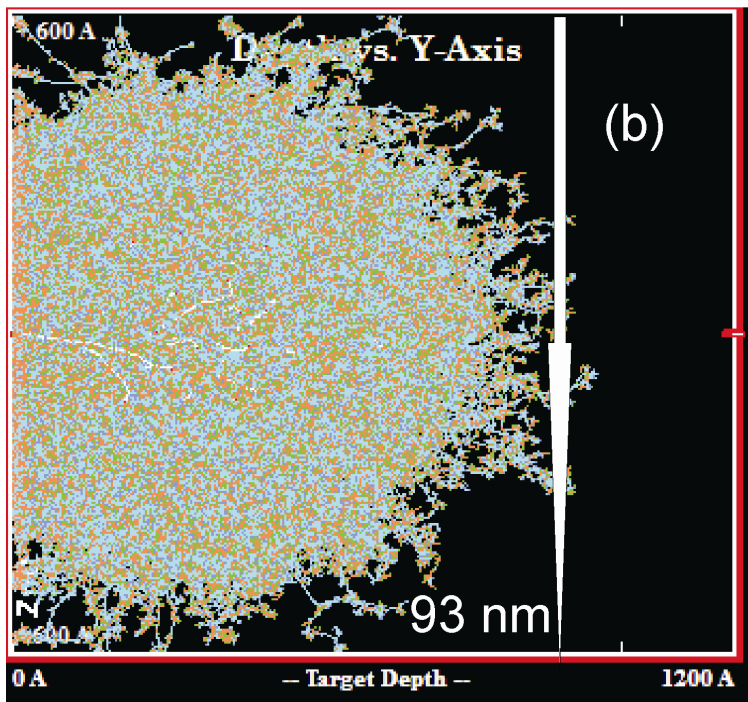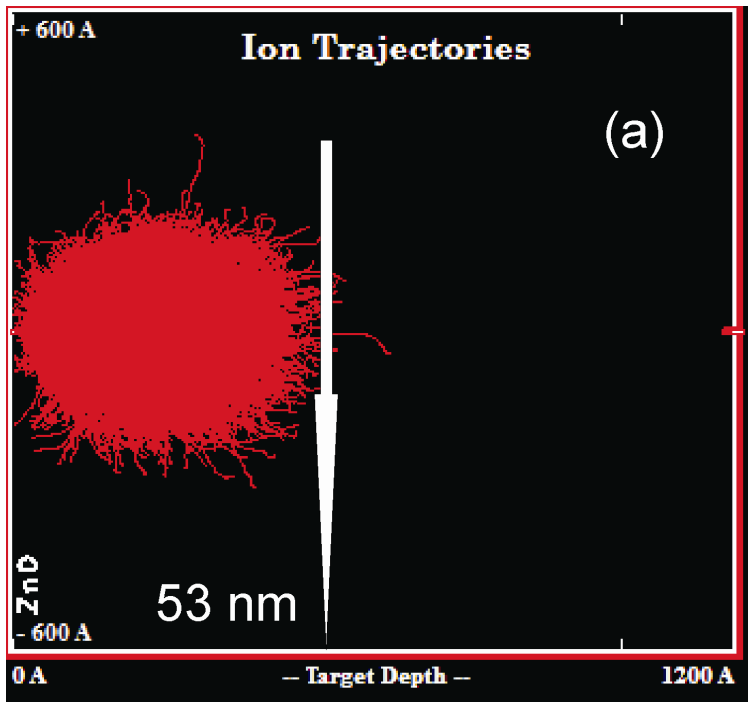
Figure 28. Stopped positions of (a) Sn ions (b) Zn and O host atoms.

Figure 29 depicts the 3D distribution of ions Sn, recoils Zn and O. The average range of Sn ions is about 19.8 nm.
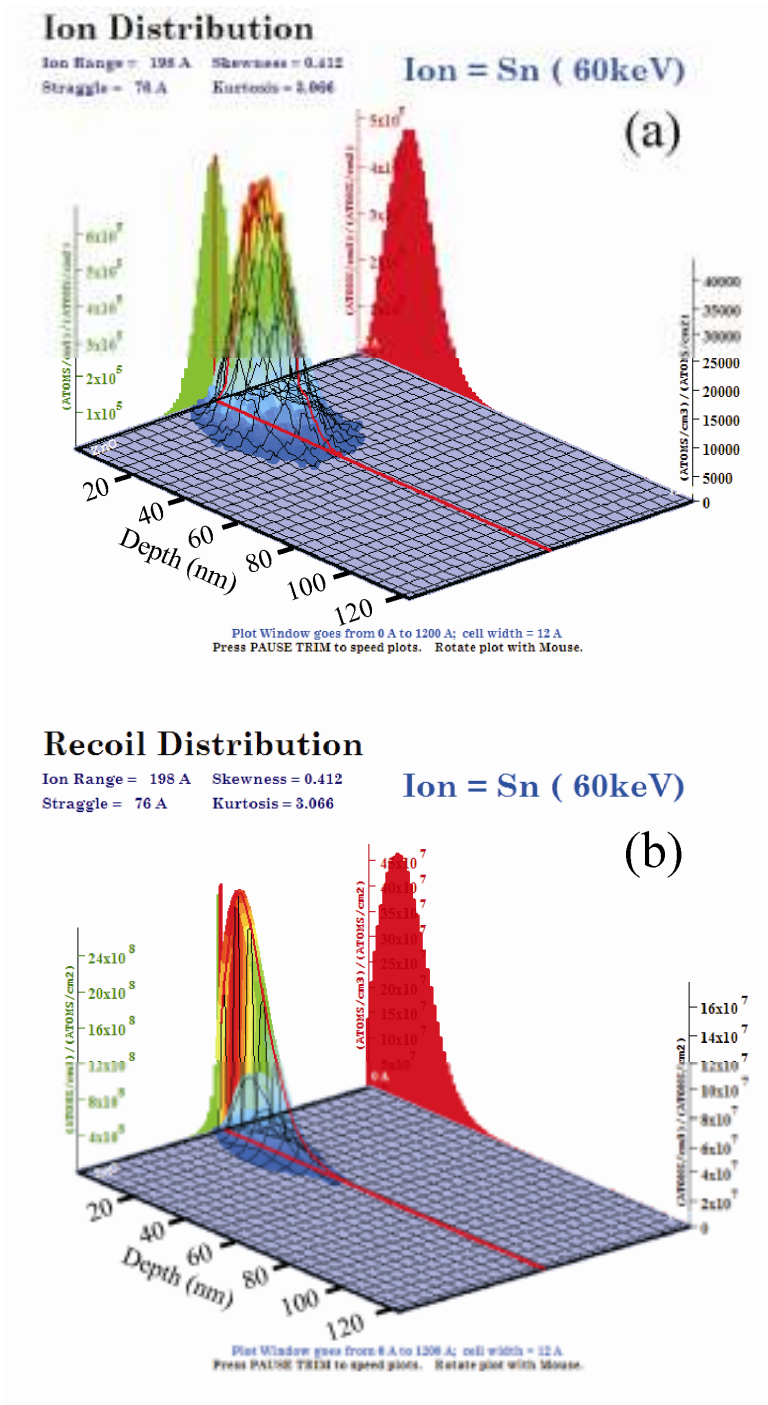
Figure 29. 3D-distribution of (a) Sn ions and (b) Zn and O host atoms.

Figure 30 depict the depth distribution of ions Sn, recoils Zn and O. From the figures the end of range (EOR) of the implanted Sn ions, Zn and O recoils were tentatively determined at approximately 50 nm, at which the ion and recoil concentrations were two- three orders of magnitude smaller than the corresponding maximum concentration. The average ranges of Zn and O recoils were calculated to be 15.6 and 15.5 nm, respectively. These average ranges were smaller than the average range of Sn ions (19.8 nm) because at the stopped position the ions have less energy to transfer to the host atoms as explained in the SRIM tutorial. Figure 31

illustrates the distributions of Zn and O vacancies and energey absorbed by Zn and O atoms over target depth. It can be seen in Figure 31(a) that the number of Zn vacancies is more than the number of O vacancies probably because Zn atoms absorbed more energy from Sn ions than the O atoms did [see Figure 31(b)]. Note that the displacement energies of Zn and O were 25 and 28 eV, respectively; the energies were filled automatically by SRIM. If not taking into account dynamic annealing, the SRIM calculations predicted that number of Zn interstitials and vacancies is more than that of O interstitials and vacancies.
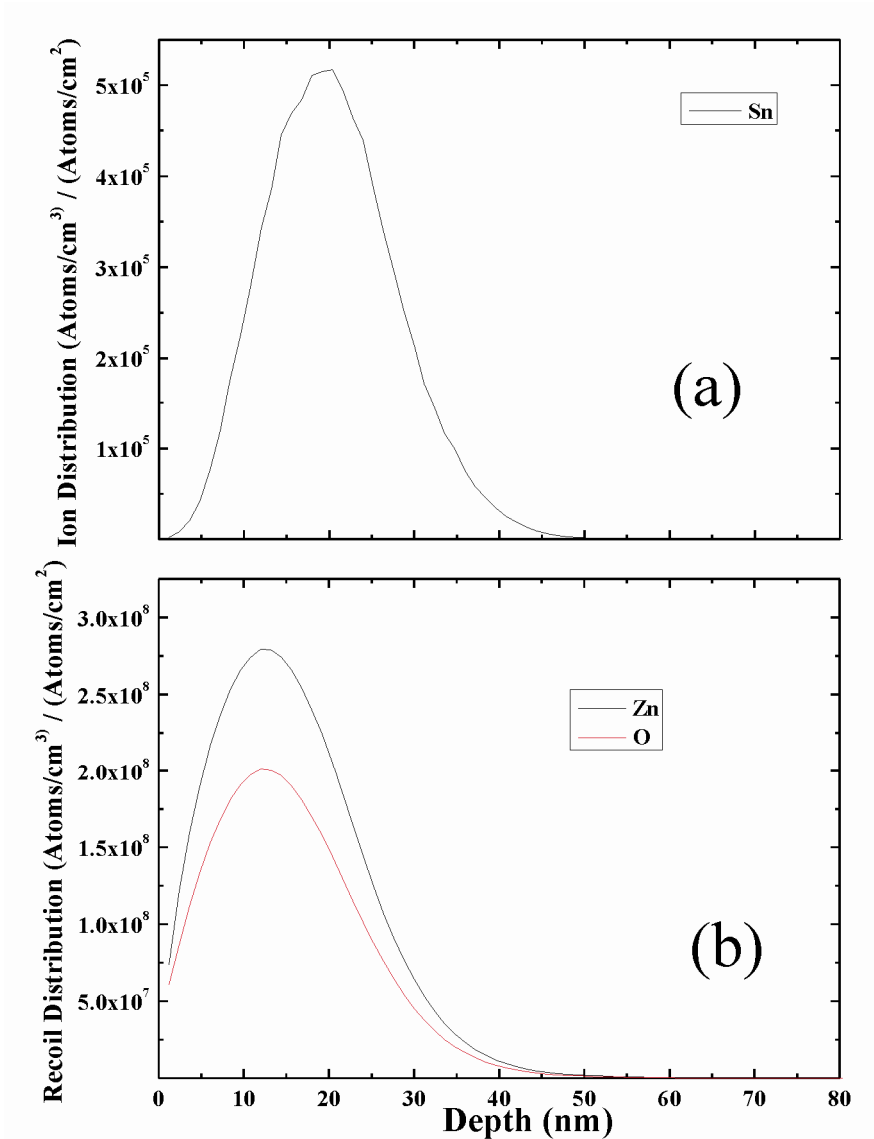

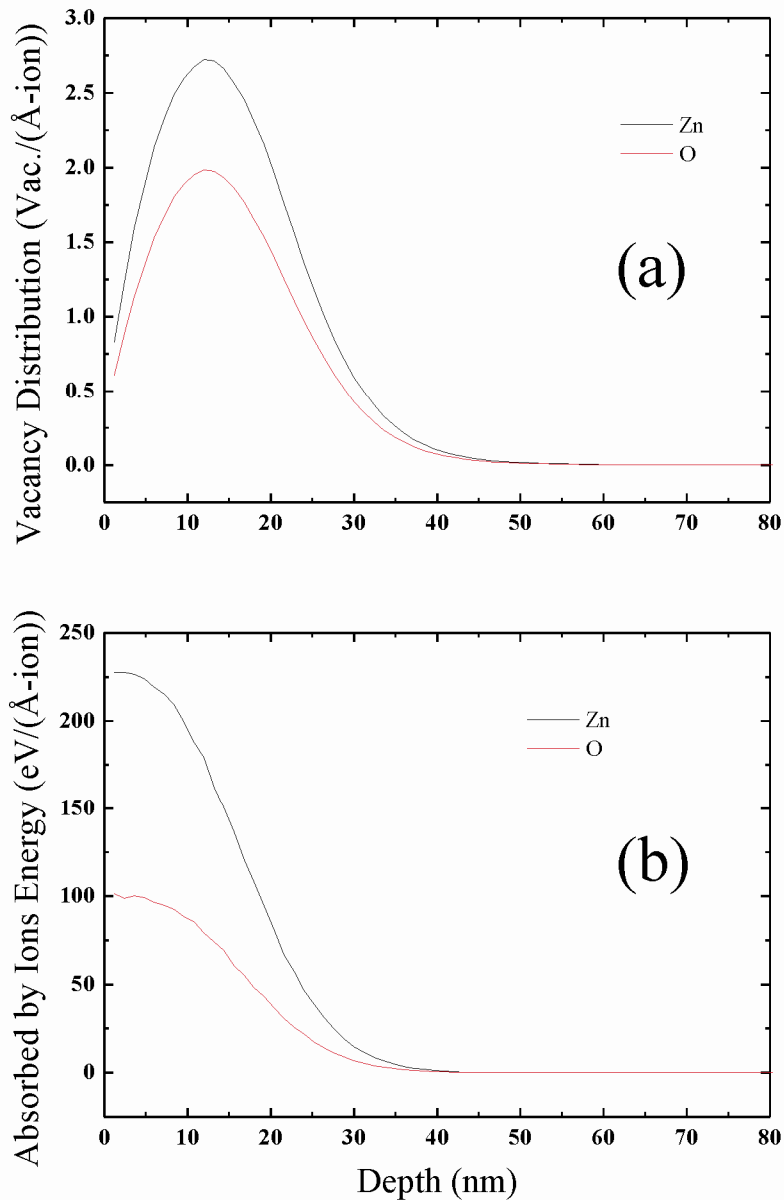**Figure 30. Depth distribution of (a) Sn ions and (b) Zn and O recoils (or interstitials).**

58

Figure 31. Depth distribution of (a) Zn and O vacancies and (b) energy absorbed by Zn and O atoms.

4.2 TEM, STEM, and EDS of ZnO wafers implanted with high doses of 60 keV Sn$^+$ ions

4.2.1 The batch 1 RT 8 × 10^{14} ions/cm^2 sample

Figure 32(a) and (b) show the BF and DF images of the batch 1 RT 8 × 10^{14} ions/cm^2 sample. The Au coating layer is indicated in Figure 32(a). No characteristic depths calculated by SRIM were discernible from the BF image; for example, maximum or average Sn$^+$ ions around 20 nm, or end of range (EOR) of Sn$^+$ ion distribution around 50 nm, or EOR of Zn and O recoil distribution around 15.5 nm. On the other hand, in the DF image, a layer of bright contrast could

be observed. The thickness of this layer was determined to be 77 nm. Previously, a sponge-like layer of 180 nm thick was observed in the GaSb implanted with the same 60 keV Sn^+ ions to nearly the same dose of 8.1×10^{14} ions/cm^2 [64]. A 130-nm-thick layer of cavities were observed in the 60 keV Sn+ ion 4.1×10^{14} ions/cm^2 sample [64]. In the current study, similar layers were not observed in implanted ZnO wafers. Coleman *et al.* [62] have reported a 15-nm-thick band of cavities in ZnO implanted at RT with 300 keV As+ ions to a dose of 1.4×10^{17} ions/cm^2. In the Figure 32(a), a ~14-nm-thick band of dark contrast appeared under the Au coating layer. However, it was not clear whether the band was caused by ion-implantation or by reaction of ZnO with Au during Au evaporation process. It should be noted that the ion acceleration voltage and ion dose in [62] were much higher than in the current study. In the DF image, in contrast, rather clear band of bright contrast appeared under the Au coating layer. The thickness of the band was determined to be approximately 77 nm. This thickness was well higher than the maximum range of Sn^+ ions but smaller than the maximum range of Zn an O recoils as calculated by SRIM.
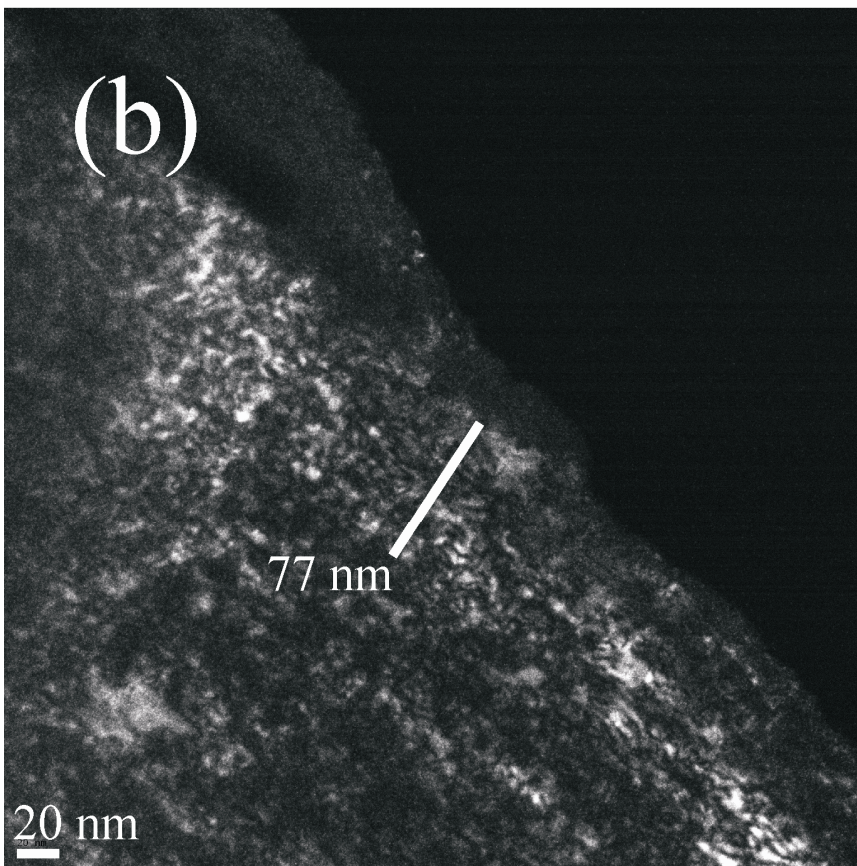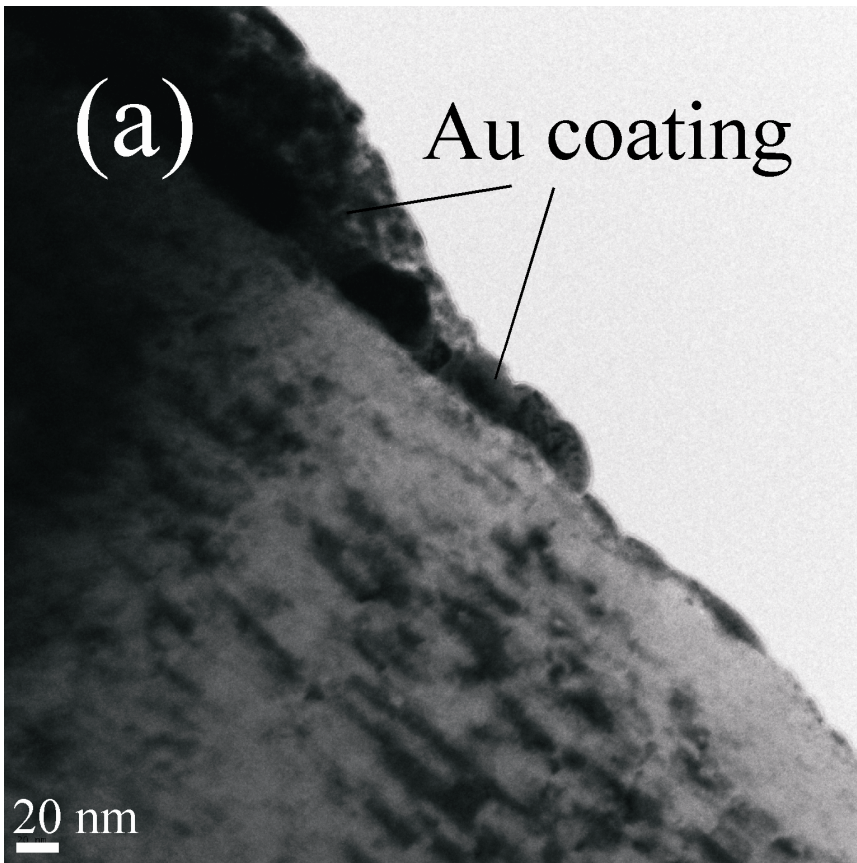
Figure 32. (a) BF and (b) DF images of the b1 RT 8 x 10^{14} ions/cm^2 sample.

The HRTEM image of the region near ZnO-Au interface is illustrated in Figure 33. The ZnO-Au interface was tentatively determined by the green line. As expected, the (001) and (100) directions indicated in the figure were perpendicular and parallel to the interface. The distances between two nearby spots along the (001) and (100) directions were approximately 7.89 and 4.35 Å, respectively. Interestingly, these distances were roughly one and half times of the lattice constants $c = 5.21$ Å and $a\sqrt{3}/2 = 2.81$ Å.
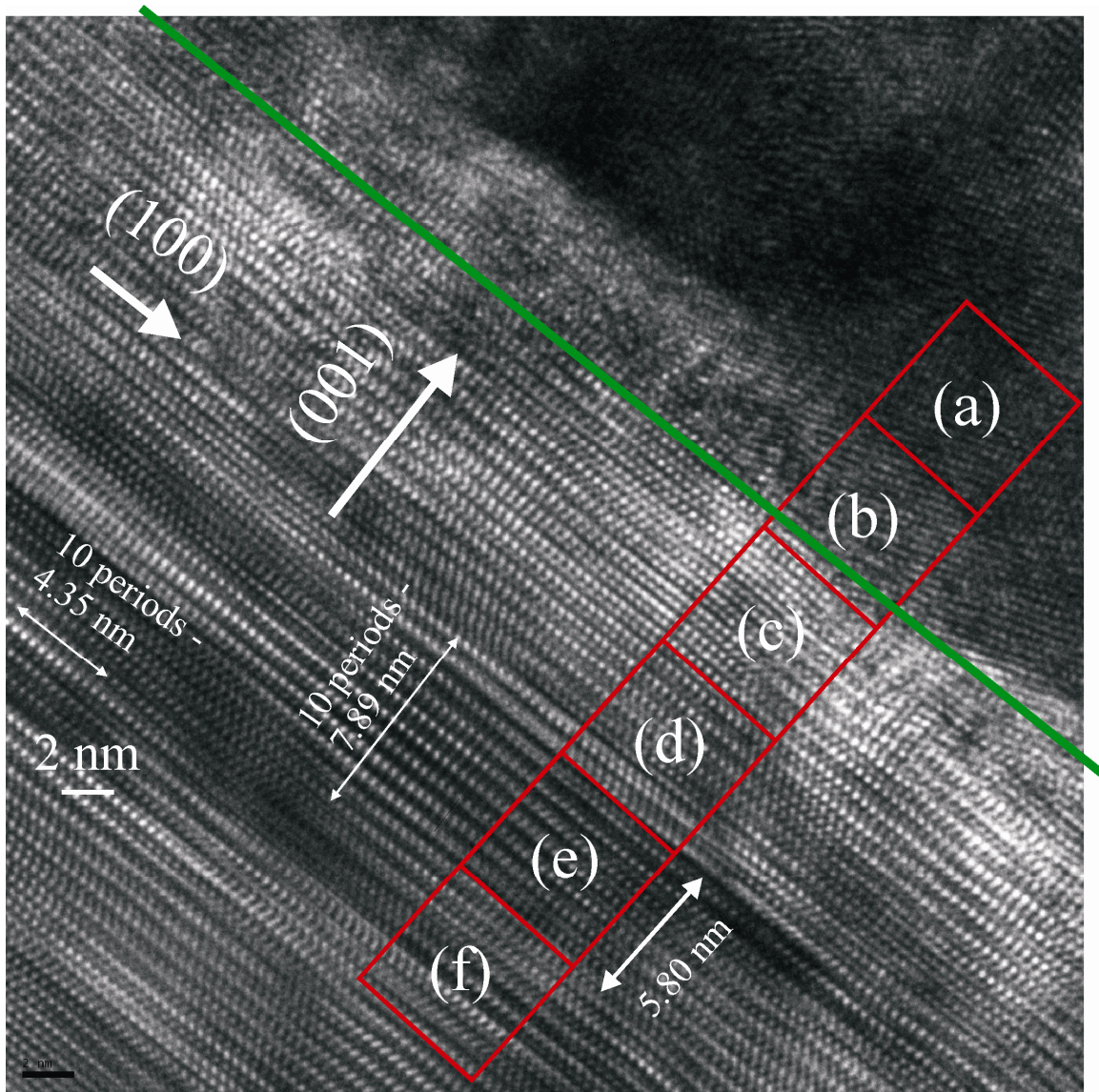
Figure 33. HRTEM image of the b1 RT 8 x 10^{14} ions/cm^2.

These photos were taken by means a CCD camera istalled in the JEOL JEM-2100F TEM. High intensity of the SAED spots could destroy the CCD camera. Therefore, SAED images were not taken, instead the Fourier Transform (FT) of interested regions was carried out. The regions subjected to FT are marked by red squares and numbered from (a) to (f) in Figure 33. The magnified pictures of those regions along with the corresponding FTs are depicted in Figure 34.

As can be seen, FT of the Au layer was significantly different from those of the ZnO regions. Spots also appeared in the FTs [see Figure 34(c)-(f)].

Figure 34. Magnified HRTEM images of the regions denoted as (a), (b), (c), (d), (e), and (f) in the previous figure. Corresponding 2D Fourier Transform images of the regions are also shown.

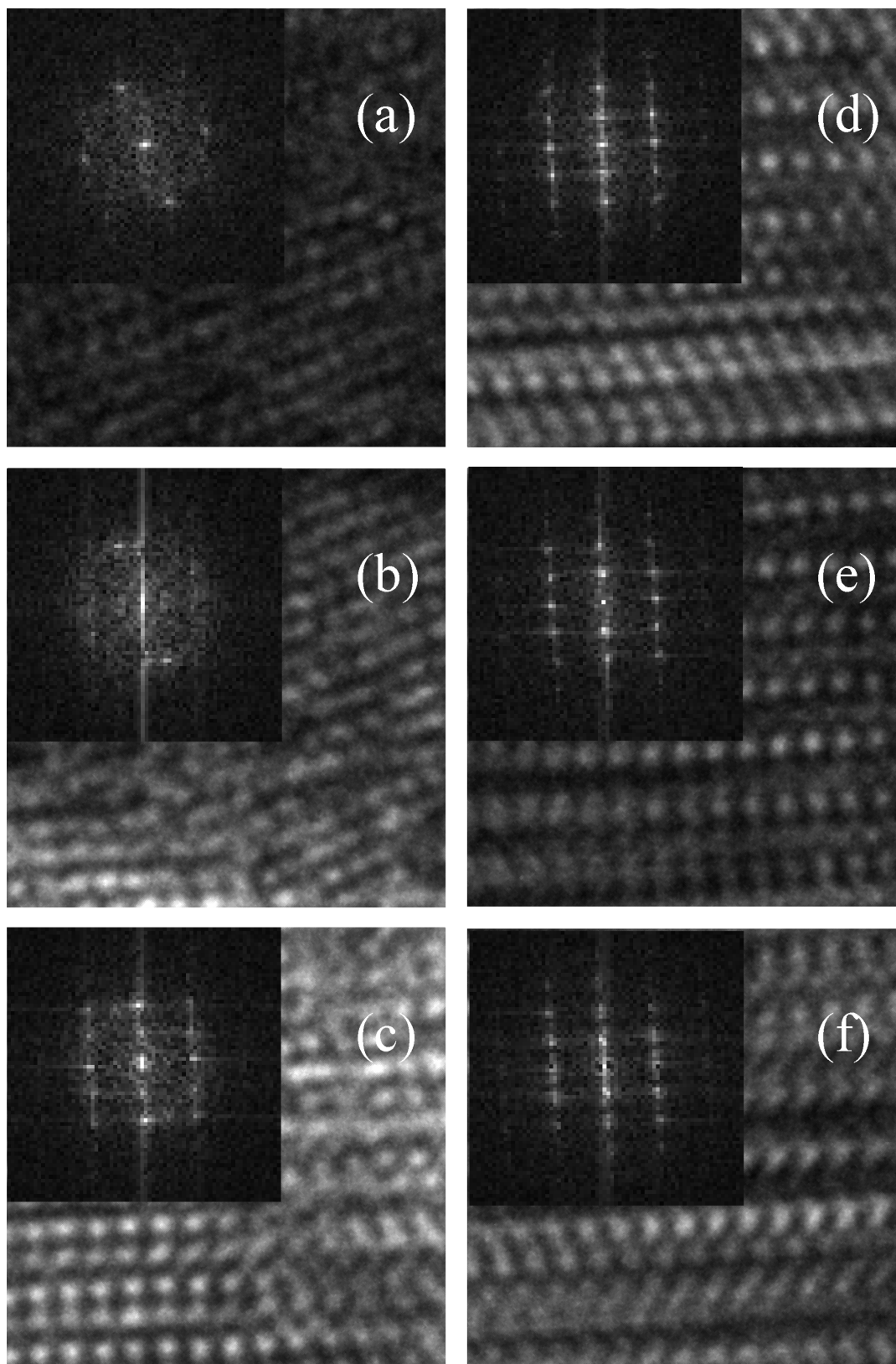As mentioned in the corresponding part in the methodology section, STEM and EDS measurements were performed in order to search for the change in relative concentration of Zn and O atoms in the implanted layers. Figure 35(a) show the STEM image of the b1 RT 8×10^{14} ions/sample. The STEM image was essentially similar to the BF CTEM image. In the figure, a straight line was drawn perpendicular to the ZnO-Au interface. Relative concentration of Zn and O atoms along the pink corridor will be measured by EDS technique. The EDS spectrum of the region limited by the STEM image was shown in Figure 35(b). Besides Zn, O peaks, Au and Pt peaks came from Au and Pt coating layers, the Cu peak probably resulted from the copper grid, the Co and Fe peaks may originate from the impurities in the sample, the Ga peak was the result of FIB manipulation. Note that Sn was not observed from the EDS spectrum, probably, because the Sn concentration was too low. The maps of Au, Sn, Zn, and O atoms in the interested region are shown in Figure 36. A bright region in Figure 36 confirms the presence of Au coating layer. It should be noted that the Sn distribution was not reliable, the demonstrated image was probably the background X-ray intensity rather than a characteristic Sn peak. Figure 37(a)-(d) plot the EDS intensities resulting from Au, Sn, Zn, and O atoms along the pink corridor drawn in the corresponding STEM image. Note that the origin of the "Depth" axis was taken at the position, which marked the end of the Au coating layer and the "depth" increased as one moved deeper inside the sample. The higher the intensities, the more number of atoms. As can be seen, the Zn and O intensities increased in the range from 125-150 nm and then saturated. This may be attributed to the increase in the thickness in the deeper region. Relative intensity of O and Zn atoms along the corridor is plotted in Figure 37 (e). The relative intensity is considered to be proportional to the relative concentration of O and Zn atoms. As can be seen the relative concentration fluctuated around an average value. Probably, the EDS measurement was not sensitive enough to detect any variation in relative Zn and O concentration.
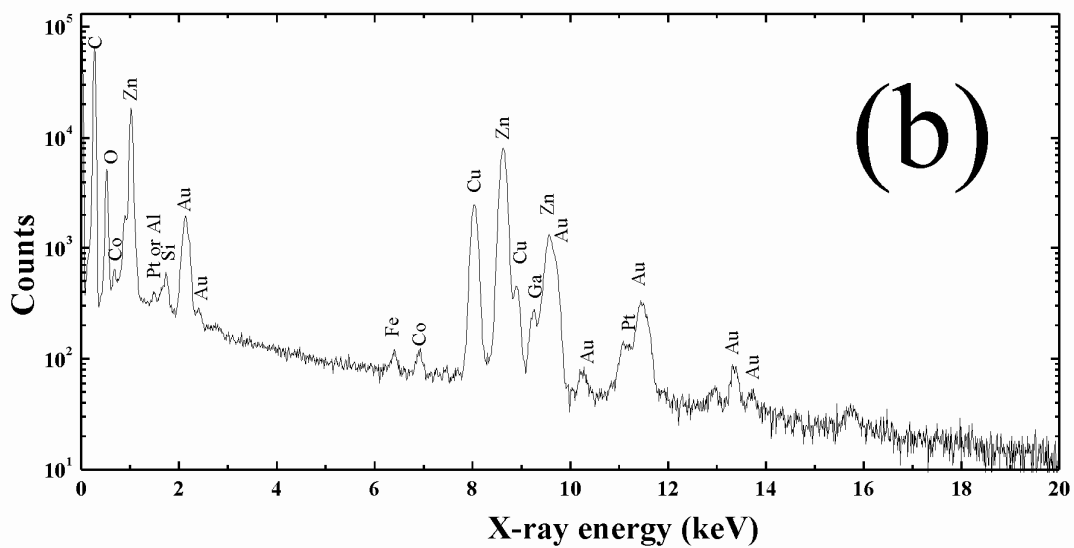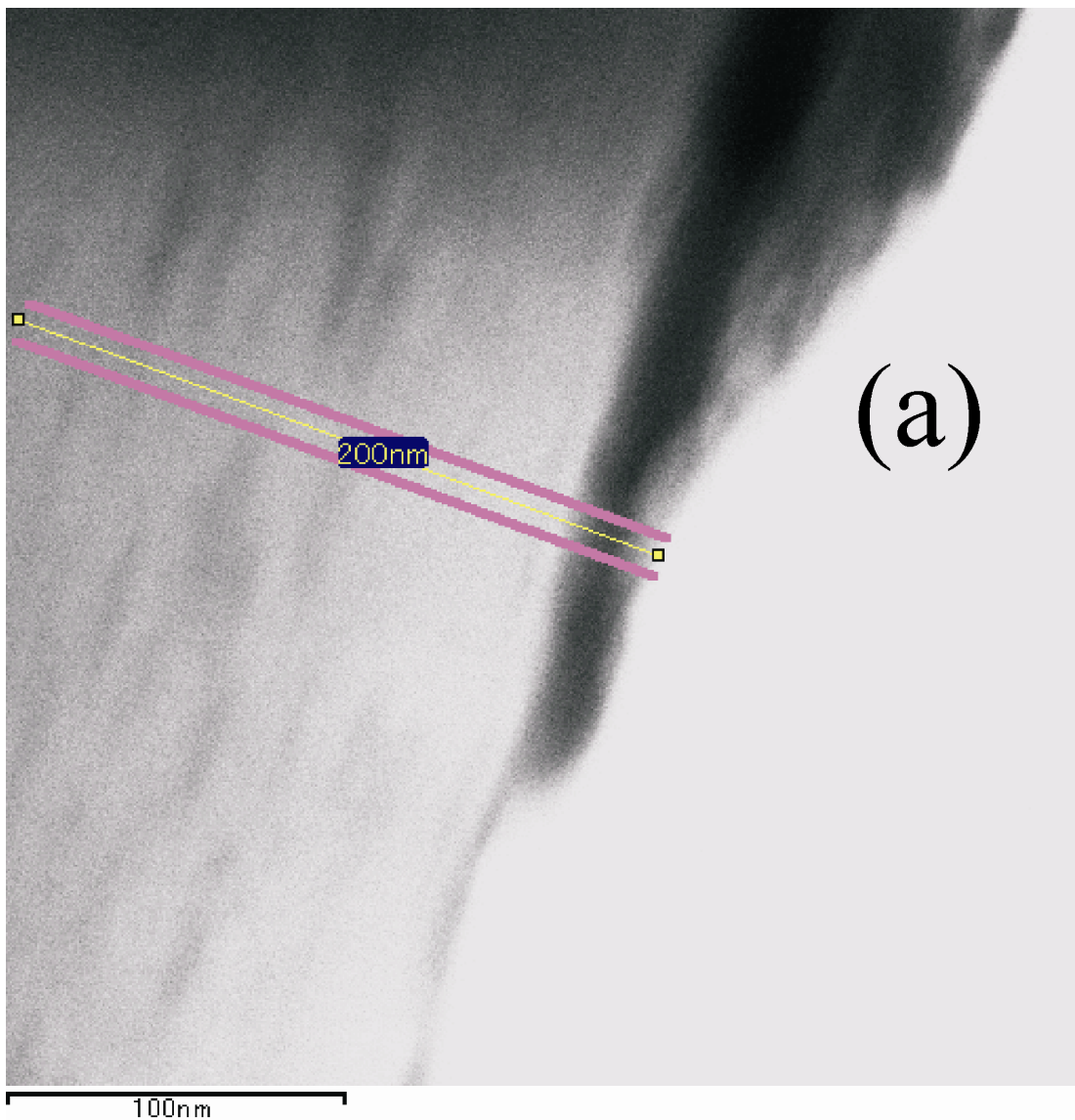
Figure 35. Batch 1 RT 8 × 10^14 ions/cm^2 sample: (a) STEM image and (b) EDS spectrum of the region depicted in the STEM image.
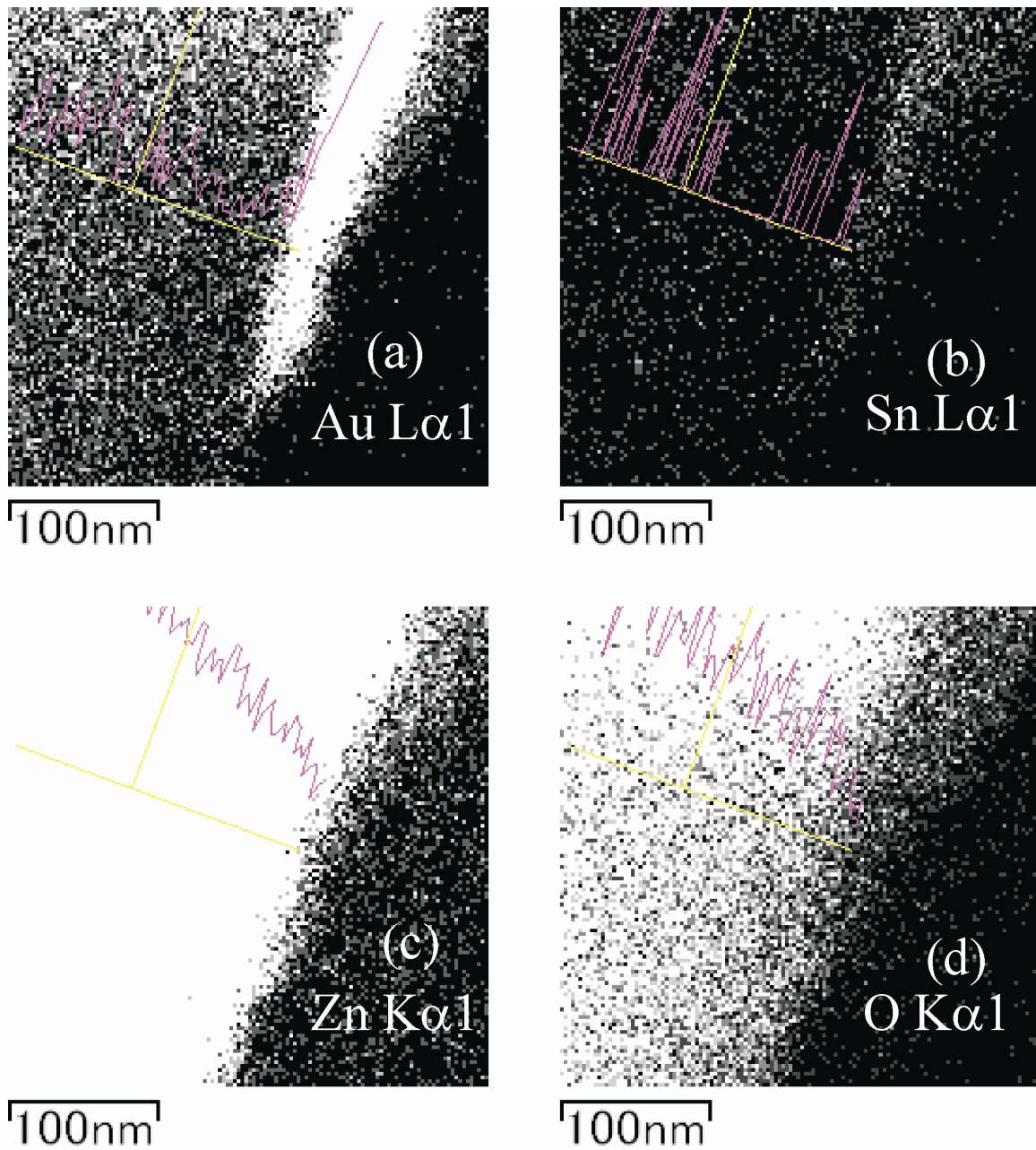
Figure 36. Distribution of (a) Au, (b) Sn, (c) Zn, and (d) O atoms in the b1 RT 8×10^{14} ions/cm^2 samples as obtained from the EDS measurements.
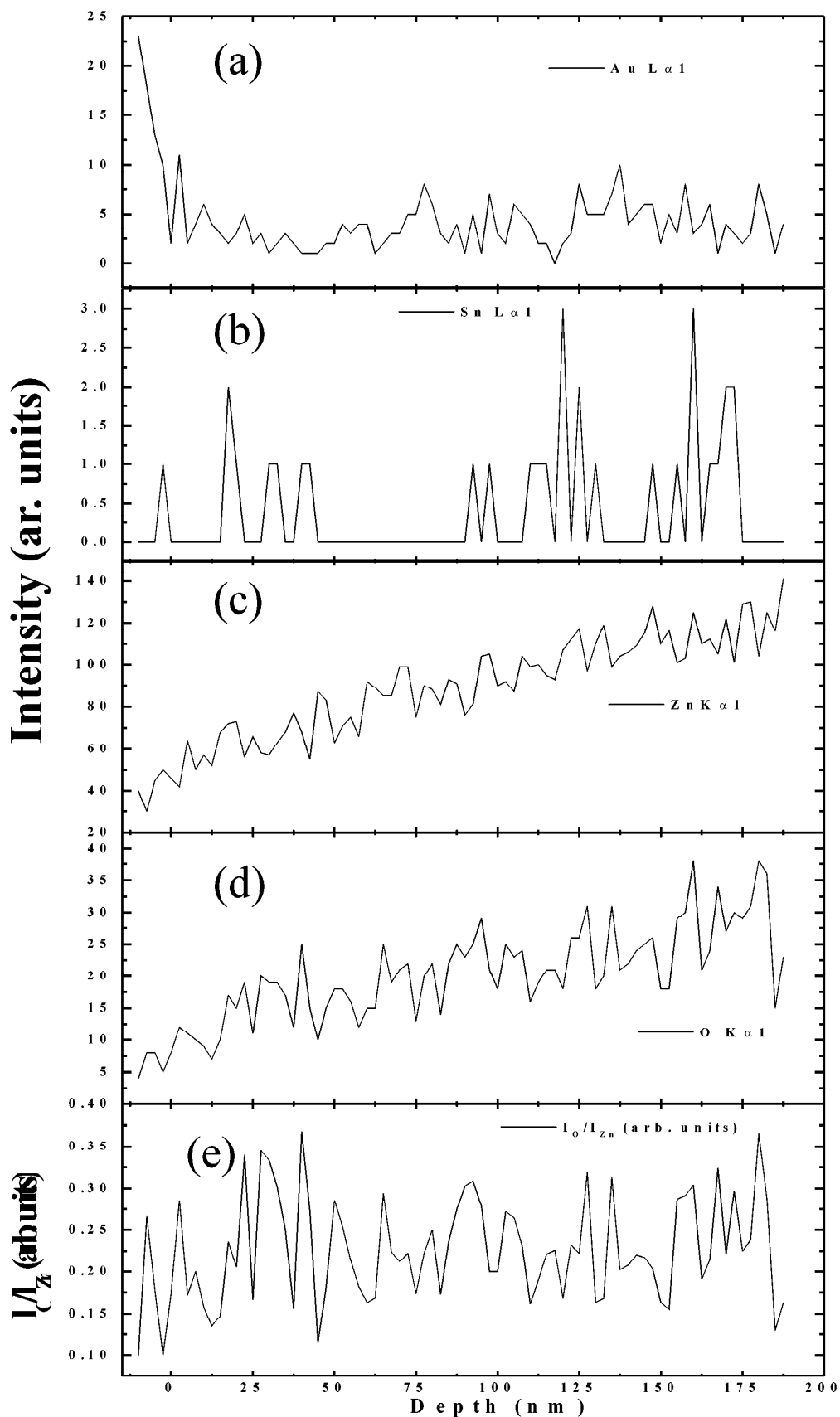
Figure 37. EDS intensities of (a) Au, (b) Sn, (c) Zn, (d) O atoms along the corridor drawn in the previous figures or in the corresponding STEM figure. The intensities are considered to be proportional to the number of atoms. (e) the relative count of O and Zn EDS intensities along the corridor. The relative count is considered to be proportional to the relative O and Zn concentration.

4.2.2   The batch 1 LT 1.5×10^{15} ions/cm^2 sample

Figure 38 (a) and (b) show the BF and DF images of the b1 LT 1.5×10^{15} ions/cm^2 sample. The Au coating layer is indicated in both figures. A band containing voids of bright contrast was observed in the BF image. The thickness of the band was approximately 16 nm, which was close to average ranges of Zn and O recoils and vacancies. In the DF image, a layer of bright contrast could be observed in the left side. The thickness of this layer was approximately 43 nm. Previously, a layer containing large ellipsoidal voids or cells was clearly observed in GaSb 180 implanted at LT with the same 60 keV Sn$^+$ ions to doses of 4.0×10^{14} ions/cm^2 or 8.9×10^{14} ions/cm^2 [64], respectively. In the current study, even though the 16–nm band of voids could be observed in the BF image, it was not as clear as in GaSb.
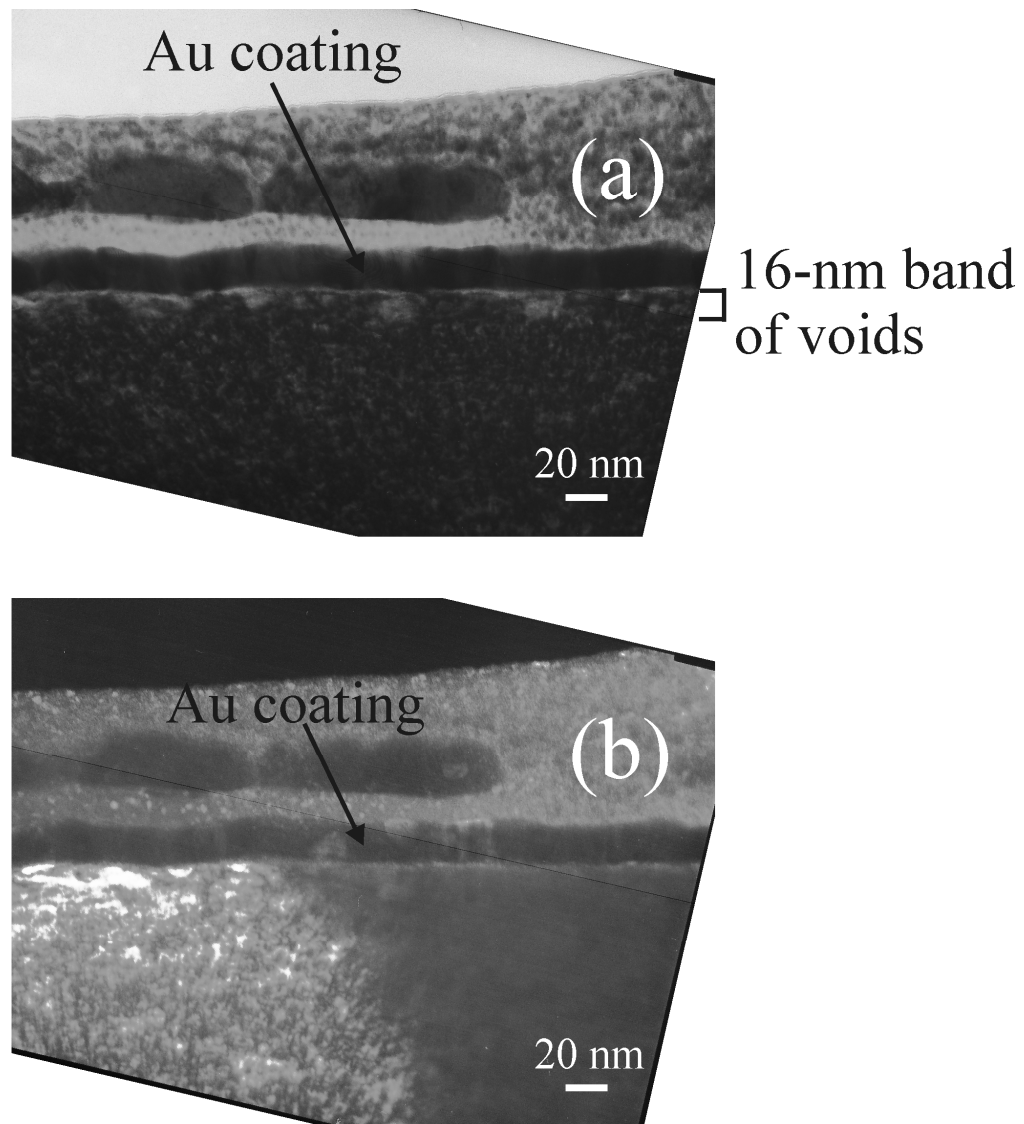
Figure 38. (a) BF and (b) DF images of the b1 LT 1.5×10^{15} ions/cm^2 sample.

The SAED of the implanted layer is demonstrated in Figure 39(a) and (b). Halos were observed along with the diffraction spots of single crystalline ZnO. Probably, ion implantation partly amorphized the implanted layer. Note that positions of the diffraction spots indicate that the electron beam was parallel to the $< 01\bar{1}0 >$ direction. Figure 39(b) showed the same SAED pattern but taken in the dark tilt configuration. Comparing the dark-tilt and bright-tilt SAED patterns, one could realize that the DF image shown in the previous figure was taken by the $\bar{2}110$ spot.
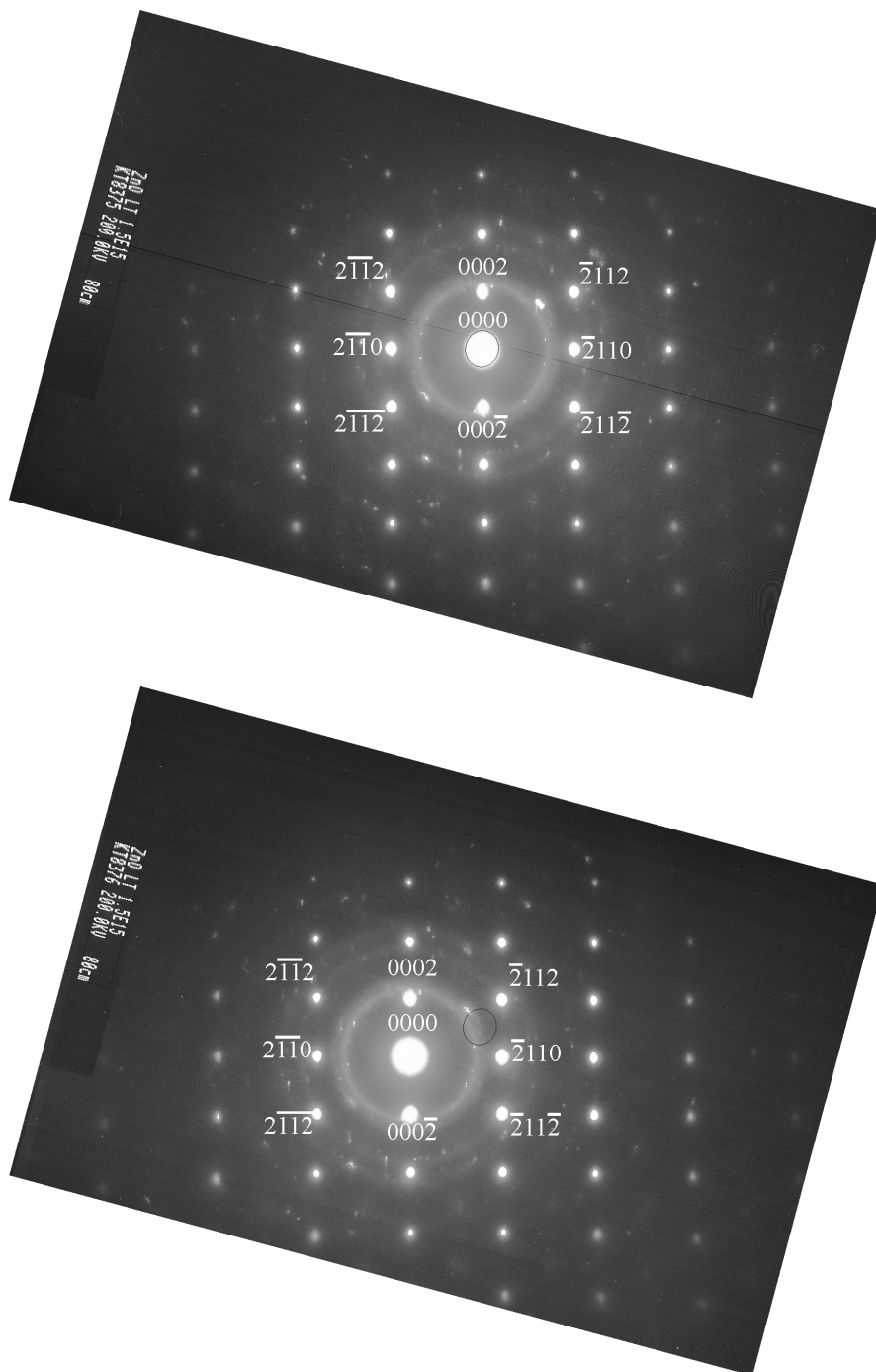
Figure 39. SAED of the implanted layer: (a) bright tilt (b) dark tilt..

The HRTEM image of the region near the ZnO-Au interface is illustrated in Figure 40 (a). A magnified image of the 10×10 nm^2 region marked with the number 4 was shown in Figure 40 (b). The region was nearly 20 nm under the ZnO-Au interface. The Fourier transform (FT) of the region showed bright spots [see Figure 40(c))], indicating that the region generally remained in crystalline phase. Note that the resolution of the original image [see Figure 40(b)] was not clear. However, if one reconstructed the image from the FT using low-pass filter [see Figure 40(e)], the resolution became better, and atomic rows can be readily distinguished [compare Figure 40(b),(d), and (f)]. Utilizing this approach, the length of 10 atomic rows was determined to be 2.81 nm [see Figure 40(f)]. The rows were parallel to the ZnO-Au surface. The distance between two continuous rows was close to the distance between two continuous $(10\bar{1}0)$ planes. It was unclear clear how the rows could appear in the HR image, given that the ZnO-Au interface was on the (0001) plane.

Figure 40. (a) HRTEM of the b1 LT 1.5 × 10¹⁵ ions/cm² sample, (b) magnified image of the region marked as 4 in a, (c) no-filter Fourier transform of b, d) figure reconstructed from the no-filter Fourier transform in c, (e) low-pass filter Fourier transform of b, and (f) figure reconstructed from the low-pas filter Fourier transform in e.

Figure 40. (a) HRTEM of the b1 LT 1.5×10^{15} ions/cm^2 sample, (b) magnified image of the region marked as 4 in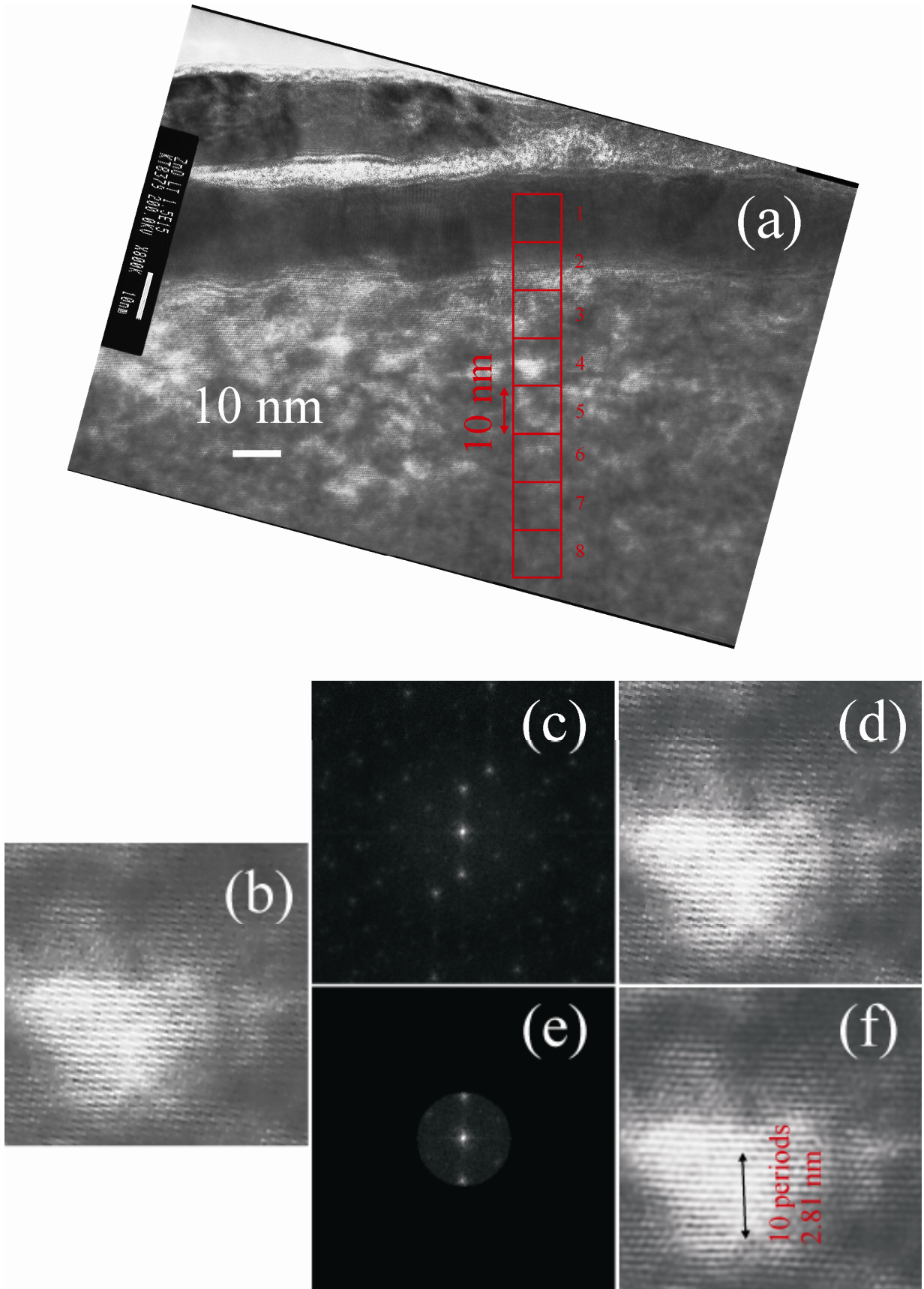 a, (c) no-filter Fourier transform of b, d) figure reconstructed from the no-filter Fourier transform in c, (e) low-pass filter Fourier transform of b, and (f) figure reconstructed from the low-pas filter Fourier transform in e.

Figure 41 (a) show the STEM image of the b1 LT 1.5 × 10^{15} ions/sample. The STEM image was essentially similar to the BF CTEM image. In the figure, a straight line was drawn perpendicular to the ZnO-Au interface. Relative concentration of Zn and O atoms along the pink corridor will be measured by EDS technique. The EDS spectrum of the region limited by the STEM image was shown in Figure 41(b). The spectrum was essentially the same as the spectrum shown in Figure 35(b). The maps of Au, Sn, Zn, and O atoms in the interested region are shown in Figure 42(a)-(d). A bright region in Figure 42(a) confirms the presence of Au coating layer. It should be noted that the Sn distribution was not reliable; the demonstrated image was probably the background X-ray intensity rather than a characteristic Sn peak. Figure 43(a)-(d) plot the EDS intensities resulting from Au, Sn, Zn, and O atoms along the pink corridor drawn in the corresponding STEM image. Note that the origin of the "Depth" axis was taken at the position, which marked the end of the Au coating layer and the "depth" increased as one moved deeper inside the sample. As can be seen, the Zn intensities increased in the range from 0-10 nm and then saturated. It appears that there existed one step in Zn intensity at approximately 60-nm depth. Differing from the corresponding image of the b1 RT 8 × 10^{14} ions/sample, the O intensity was small and shows no regularities. This may be attributed to the increase in the thickness in the deeper region. Relative intensity of signals resulting from O and Zn atoms is plotted in Figure 37(e). Again, no regularities could be observable. Probably, the EDS measurement was not sensitive enough to detect any variation in relative Zn and O concentration.
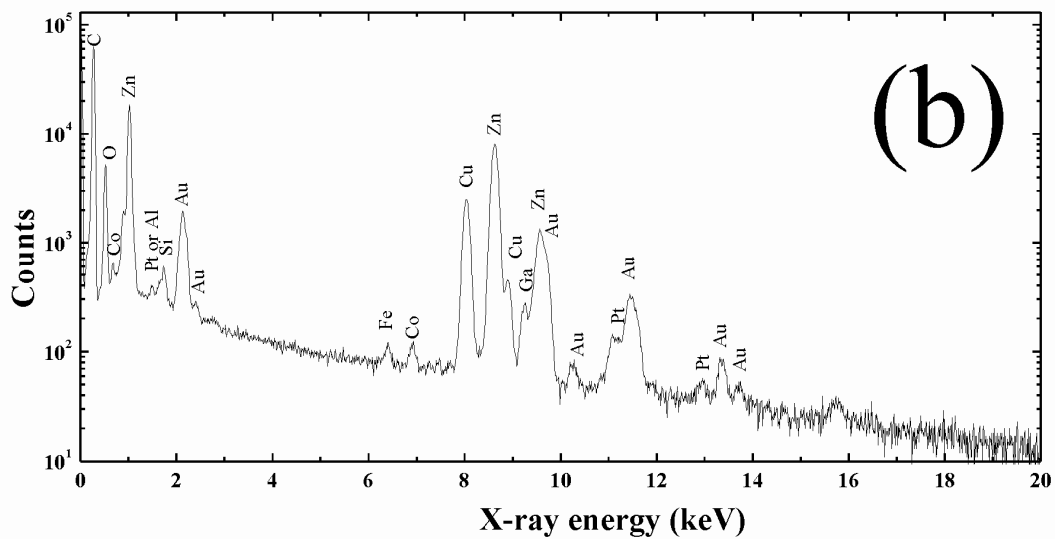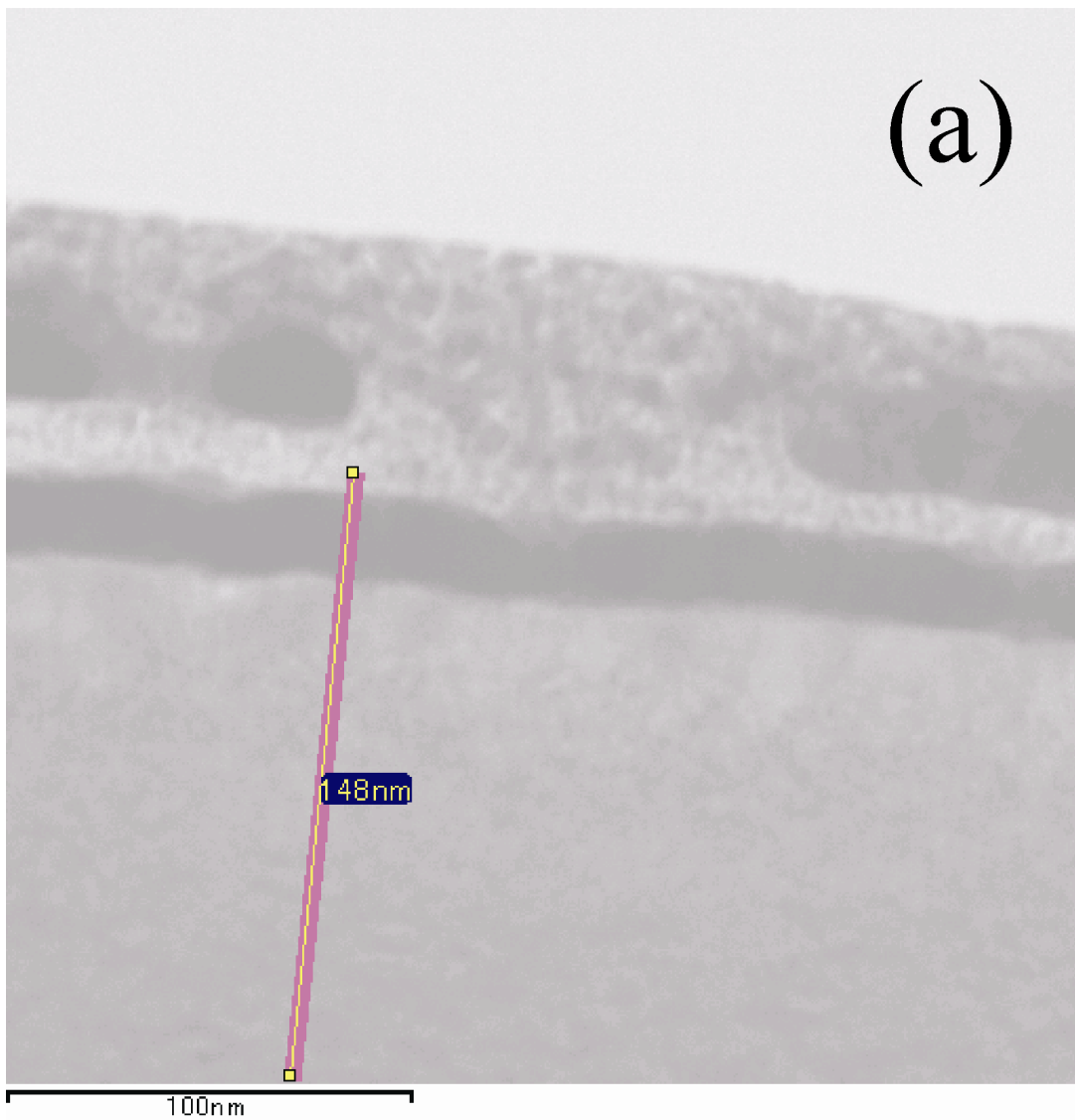
Figure 41. Batch 1 LT 1.5 × 10^{15} ions/cm^2 sample: (a) STEM image and (b) EDS spectrum of the region depicted in the STEM image.
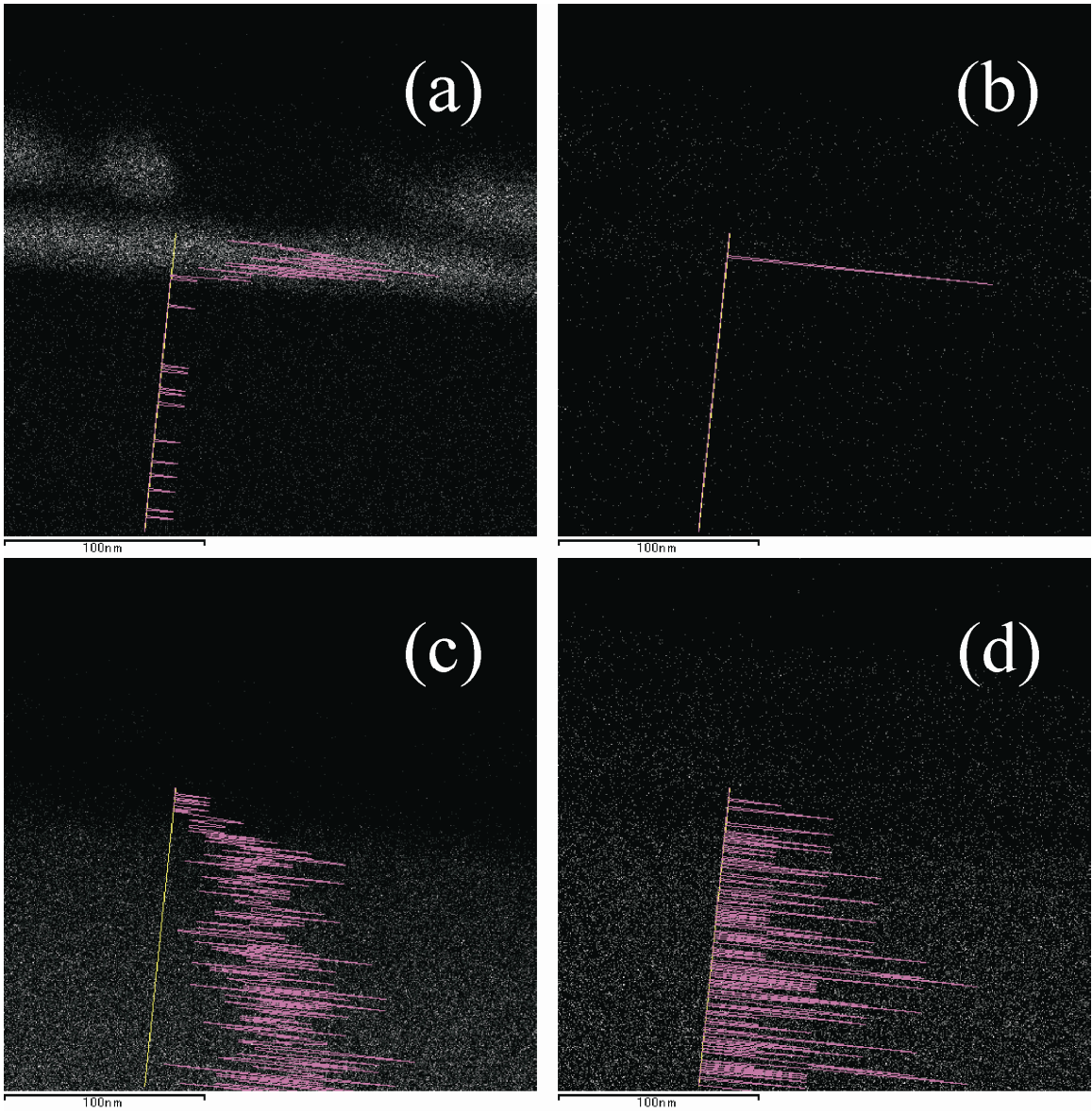
Figure 42. Distribution of (a) Au, (b) Sn, (c) Zn, and (d) O atoms in the b1 LT 1.5 × 10^{15} ions/cm^2 samples as obtained from the EDS measurements.
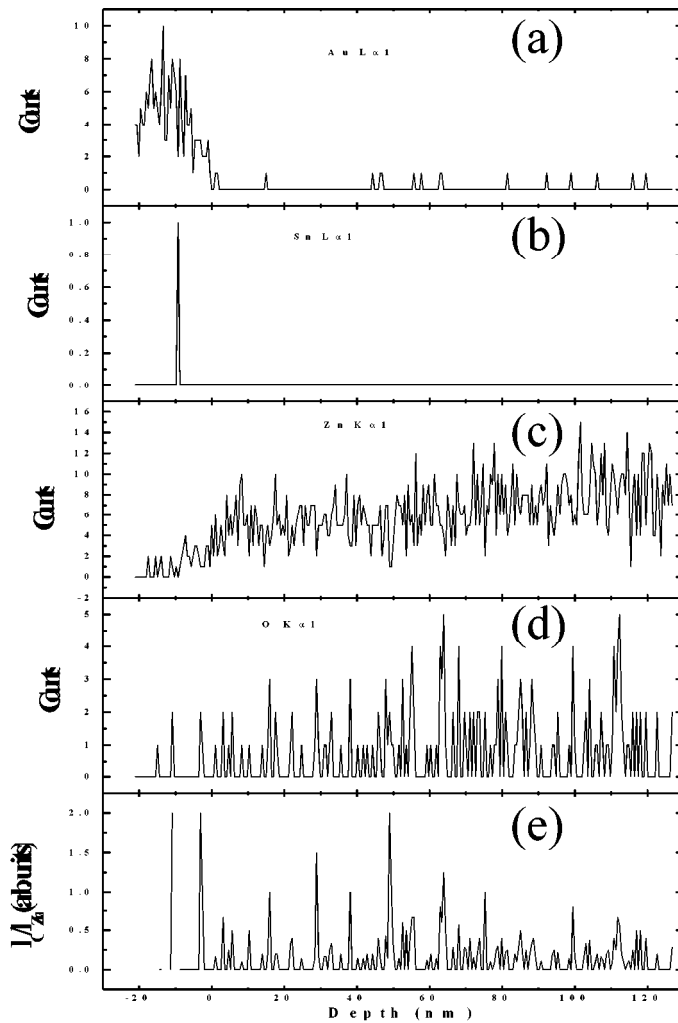
Figure 43. EDS intensities of (a) Au, (b) Sn, (c) Zn, (d) O atoms along the corridor drawn in the previous figures or in the STEM image of the b1 LT 1.5 × 10^{15} ions/cm^2 sample. The intensities are considered to be proportional to the number of atoms. (e) The relative count of O and Zn EDS intensities along the corridor. The relative count is considered to be proportional to the relative O and Zn concentration.

4.3 XRD of the batch 2 samples

The wide-range XRD patterns of the batch 2 samples are shown in Figure 44. Three peaks were observed at 34.42, 52.68, and 72.56 $^{\circ}$ [(see Figure 44(a)]. They were attributed to 0002, 0003, and 0004 reflections, respectively. Note that the interplanar spacings of the 0002, 0003, and 0004 planes were determined from the 2θ angles to be 2.6055, 1.7374, and 1.3028 Å, respectively. As required, these values within the experimental errors satisfy the equation: $2/d_{(0003)} = 1/d_{(0002)} + 1/d_{(0004)}$, where $d_{(0002)}$, $d_{(0003)}$, and $d_{(0004)}$ are interplanar spacings of the 0002, 0003, and 0004 planes, respectively. Note that the interplanar spacing of the (*hkl*) plane in the hexagonal lattice is calculated by the formula [96]: $\frac{1}{d^2} = \frac{4}{3a^2}(h^2 + hk + k^2) + \frac{l^2}{c^2}$. The high sharpness of the 0002 and 0004 peaks indicates high crystallinity of the samples used in this

75

thesis. Although the reflection from the (0003) planes is forbidden according to the structure factor theory [96], the appearance of the (0003) peak indicates that the samples used in this thesis contained some defects (probably twins).

Figure 44. Wide-range XRD patterns of the batch 2 (a) RT 3.6 × 10^{12}, (b) RT 4.1 × 10^{13}, (c) RT 8.0 × 10^{13}, (d) RT 1.6 × 10^{14}, (e) RT 2.4 × 10^{14}, (f) LT 8.8 × 10^{13}, (g) LT 4.1 × 10^{13}, (h) LT 2.4 × 10^{14}, (i) LT 4.9 × 10^{14} ions/cm^2 samples.
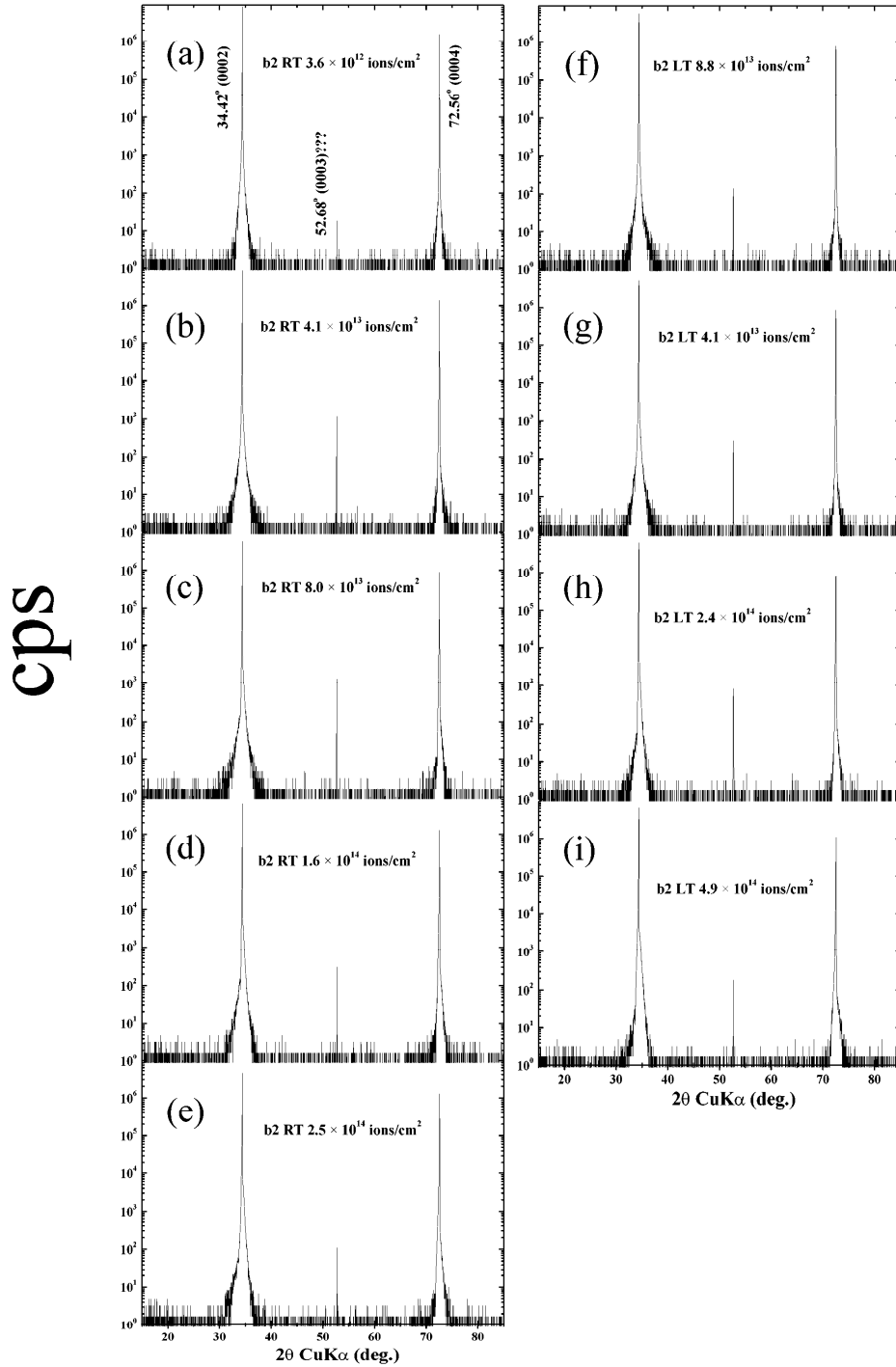
Figure 45(a) and (b) plot the detailed XRD view of 0002 and 0004 reflections of the RT (top) and LT (bottom) samples. The peaks from the b2 LT 8.8×10^{13} ions/cm^2 sample were highly symmetric, which remarkably differed from those from other LT samples including the lower dose LT 4.1×10^{13} ions/cm^2 sample. Probably, the dose of the LT 8.8×10^{13} ions/cm^2 was much lower than denoted. For RT samples, although the 0002 and 0004 peaks resulting from the RT 3.6×10^{12} ions/cm^2 were also highly symmetric, a low-angle shoulder appeared in the samples implanted to doses of 4.1×10^{13} ions/cm^2 and higher and it moved further in the low-angle direction as the implantation dose was increased [see top parts of Figure 45(a) and Figure 45(b)]. This was observed in both the 0002 and 0004 reflections. At first, the shoulder was thought to be due to polycrystalline aggregates [86] because a high-angle shoulder also appeared in the RT 2.5 $\times 10^{13}$ ions/cm^2 and LT 4.9×10^{13} ions/cm^2 samples (see Figure 45), for example. The low- and high- shoulders would result from solely one polycrystalline-originated peak. However, high-resolution triple crystal X-ray diffraction (TCD XRD) [89] measurements revealed that the high- and low-angle shoulders resulted from separate peaks as demonstrated in Figure 46. This can be clearly observed in the XRD spectrum of the RT 1.6×10^{14} ions/cm^2. Previously, similar low-angle shoulders have been observed in numerous ion-implanted sample [83, 84, 109]. Sousbie *et al.* [109] attributed the origin of the low-angle shoulder to a strain profile resulted from high concentration of hydrogen implants in their experiments. Meanwhile, Cheng *et al.* also assigned the low-angle shift with implantation dose to the increasing point defect density, but they did not specify which concrete point defects they meant. Zaumseil *et al.*[84] claimed that the shoulder originated from dislocation loops and they even constructed a model to calculate the loop size from the measured XRD data. Formation of interstitial dislocation loops in ZnO irradiated with >300 keV electrons has been reported by Iwanaga *et al.* [61]. Probably, the low-angle shoulder observed in this study resulted from dislocation loops.
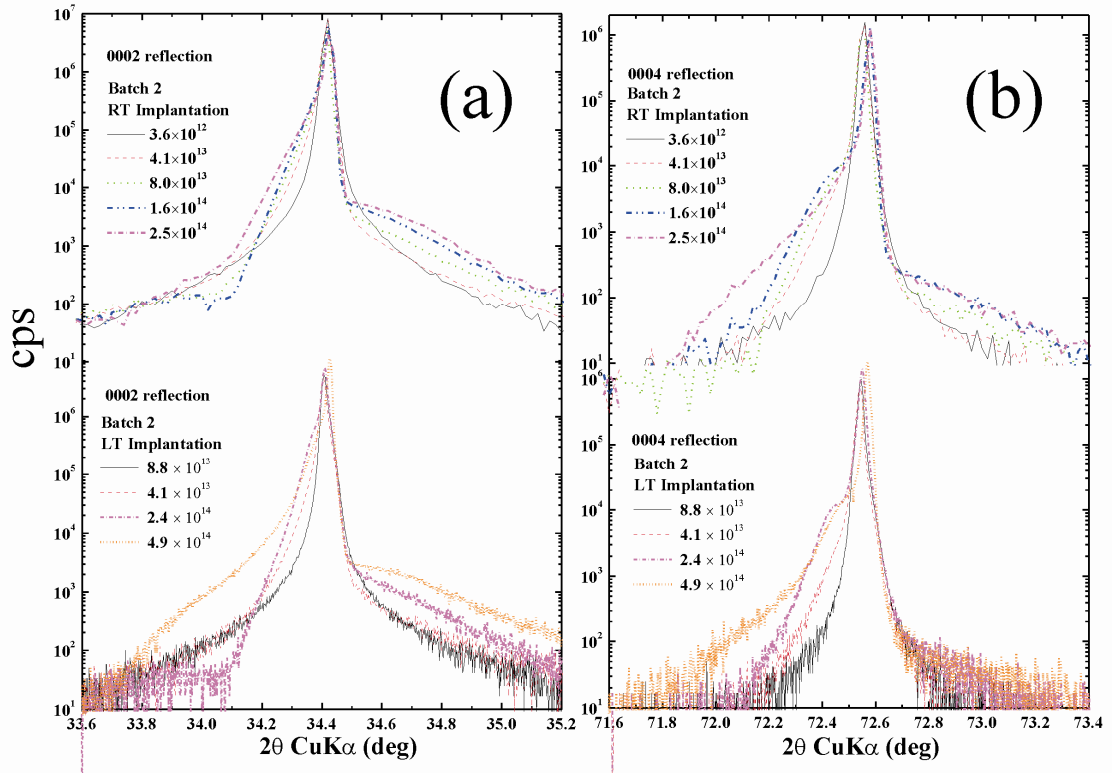
Figure 45. XRD detailed scans around the (a) 0002, (b) 0004 reflections. The top figures show the data measured in batch 2 RT samples, and bottom figures in batch 2 LT samples.
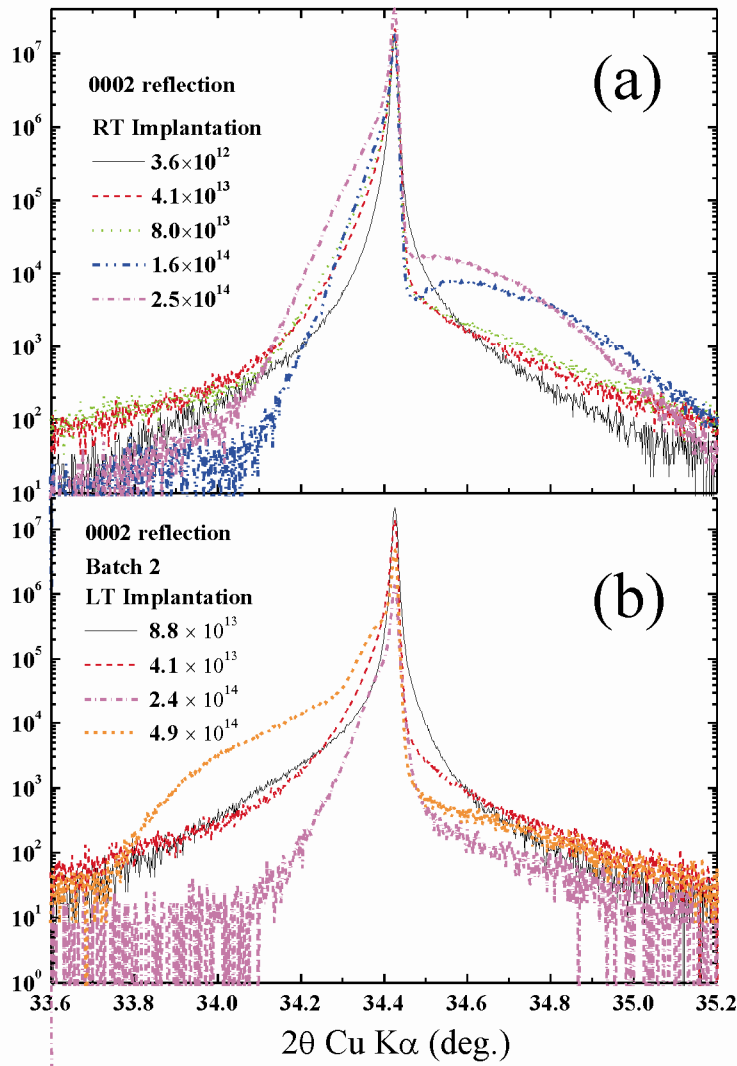
Figure 46. X-ray Tripple-Crystal Diffractometry (TCD XRD) patterns around the 0002 reflection of the batch 2 (a) RT and (b) LT samples.

4.4 AFM images of the batch 2 RT samples

Figure 47(a)-(e) show the AFM images of all the b2 RT ZnO wafers. As can be seen in these figures, no significant variations in morphology were observed. In each image, root mean square (RMS) roughness of five approximately-200-nm-long lines was calculated. These lines were selected so that they did not cross scratches on the sample surface, as shown by arrows in Figure 47(a)-(e). Figure 47(g) depicts Z-position of points along the five lines drawn in Figure 47(e). Each sample was imaged at various imaging parameters (measurement times were 0.167 ms and 0.333 s, feedback filter frequencies were 5 and 10 Hz, the gain levels were 2 and 3 if considered the highest gain level was 4). Subsequently, the RMS roughness was averaged over all recorded images. It should be noted that although the changes in measurement parameters (the measurement time, feedback filter frequency, gain level) slightly deviated the RMS roughness, the calculation procedure was essentially the same for all samples. The calculated RMS

roughness is plotted in Figure 47(f) as a function of implantation dose. As can be seen in the figure, the RMS roughness of the wafers implanted to doses of 3.6×10^{12}, 4.1×10^{13}, 8×10^{13}, and 1.6×10^{14} ions/cm^2 was just slightly different.
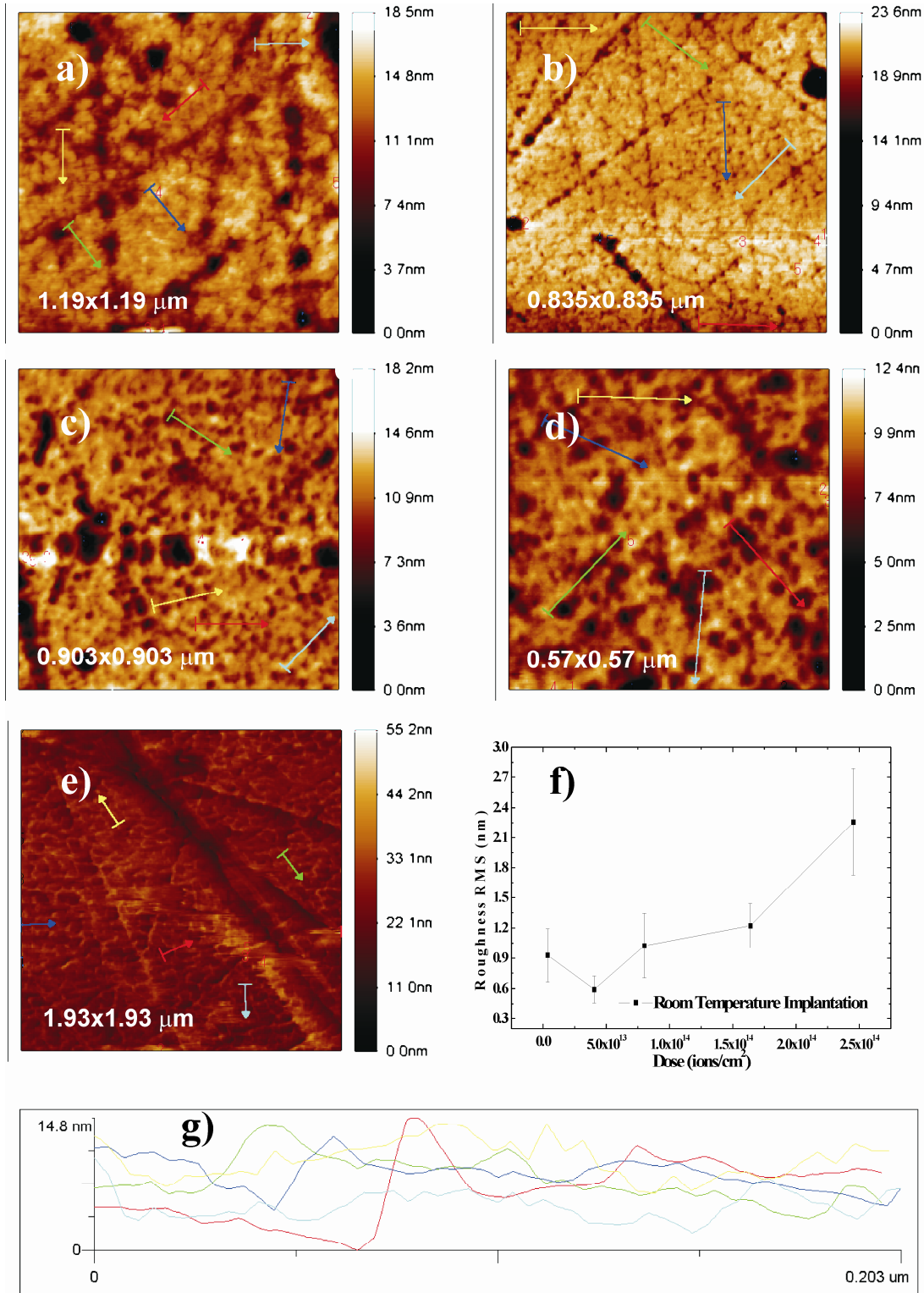
Figure 47. AFM images of batch 2 ZnO wafers implanted at room-temperature to doses of (a) 3.6×10^{12}, (b) 4.1×10^{13}, (c) 8.0×10^{13}, (d) 1.6×10^{14}, and (d) 2.5×10^{14} ions/cm^2; (f) implantation dose dependence of RMS roughness; (g) Z-position of points along 5 lines depicted in (e).

Previously, Singh *et al*. [110] have reported RMS roughness of 0.7 nm in the "un-exfoliated" area of ZnO implanted with 100 keV H_2^+ ions to a dose of 2.7×10^{17} ions/cm^2. In addition, Coleman *et. al*.[62] have reported RMS roughness of ZnO single crystal implanted at RT with 300 keV As^+ ions to a dose of 1.4×10^{17} ions/cm^2 and that of unimplanted ZnO to be 2.5 nm and 0.6 nm, respectively. These values are in the same order of magnitude as the RMS roughnesses of the 2.5×10^{14} (2.3 nm) and 3.6×10^{12} (0.9 nm) samples in the current study. It appears that RMS roughness did increase with implantation dose.

4.5 Electrical properties of samples in batches 1 and 2

Figure 48(a)-(f) plots sheet resistance R_s, resistivity ρ, Hall coefficient R_{Hs}, mobility μ_H, sheet carrier concentration n_s, and carrier concentration n of the ZnO wafers as functions of implantation dose. Note that the resistivity and carrier concentration should be considered as "effective" values because the implanted samples were not uniform across their thickness. The implanted layers were certainly different from the unimplanted layers below. It can be seen that the implantation dose dependences of resistances and carrier concentrations show no regularities; whereas mobility appears to decrease with implantation dose in all samples of batches 1 and 2 [see Figure 48(d)]. The decrease in mobility probably resulted from scattering of carriers by Sn impurities or implantation-induced defects. However, the order of mobility did not change (the mobility varied in the range from 20 to 80 cm^2/(V.s)). Therefore, variation of resistivity was probably determined mainly by variation of carrier concentration. Two possibilities may account for the irregular variation of carrier concentration in the samples. First, the original wafers before implantation were not identical and possessed different carrier concentrations. Second, the production and annihilation of charge carriers were complicated during ion-implantation process.
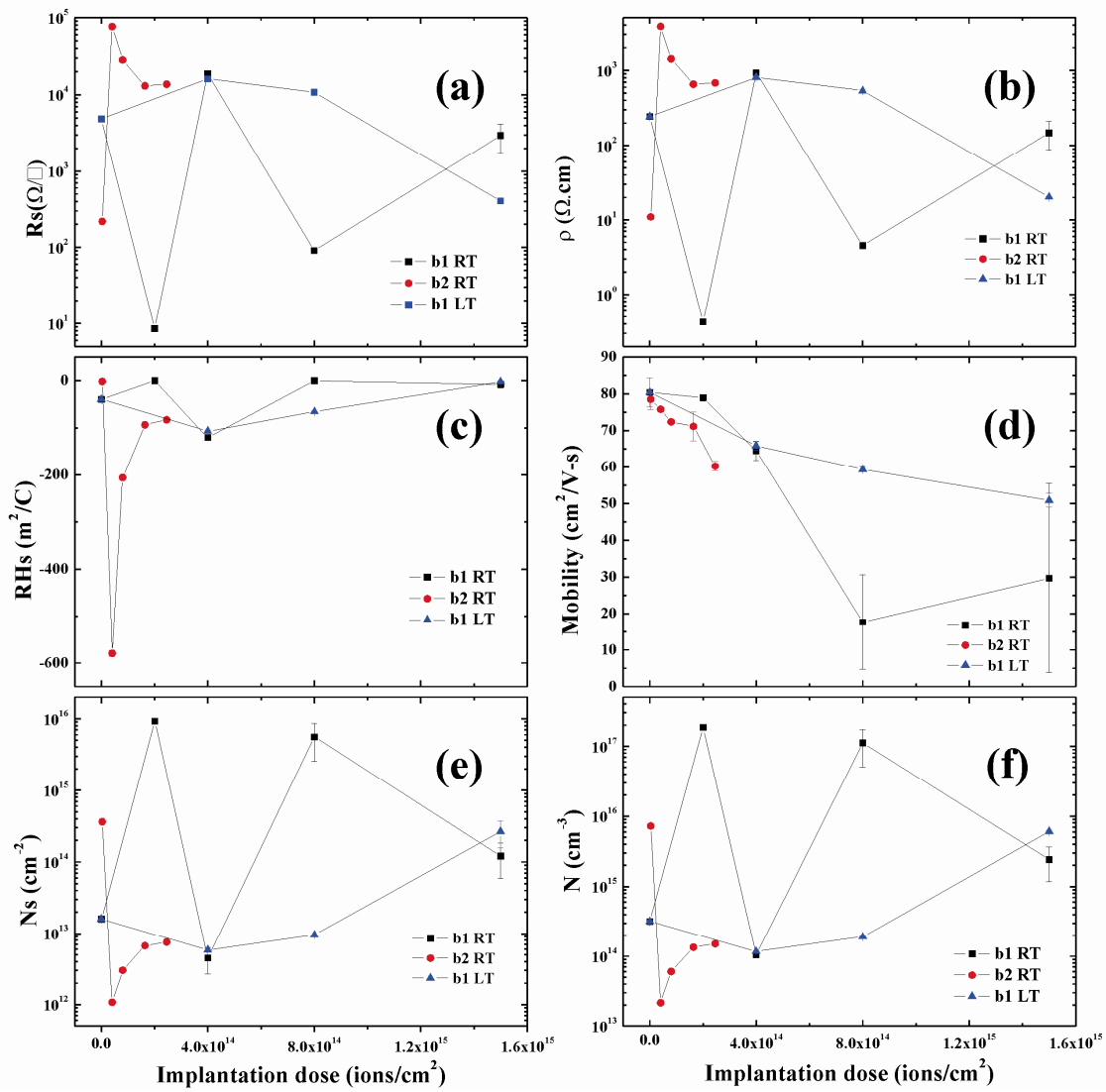
Figure 48. Implantation dose dependences of (a) sheet resistatnce, (b) resistivity, (c) Hall coefficient, (d) carrier mobility, (e) sheet carrier concentration, and (f) carrier concentration.

4.6 Transmittance, reflectance, and absorbance of batches 1 and 2 samples

Figure 49(a) shows the transmission spectra measured in the batch 2 wafers. The wafers were almost transparent for the photon energy in the range from 1.6 to 2.6 eV with transmission of approximately 80%. At the photon energy of approximately 3.2 eV, the transmission became zero, marking the energy edge of ZnO. As confirmed by the XRD and PL measurements, effect of implantation on the batch 2 RT 3.6×10^{12} ions/cm^2 sample was negligible. Therefore, transmission of this sample can be considered as transmission of an unimplanted ZnO wafer. As can be seen in the Figure 49(a), the deviation from the unimplanted wafer transmission increased with implantation dose, namely in the photon energy range from 2.5 to 3.2 eV the transmission decreased with implantation dose. This was observed in both RT and LT samples. Especially, in the LT samples the monotonic deviation was evident except for the b2 LT 8.8×10^{13} ions/cm^2 samples, whose transmission spectrum was essentially the same as that of the b2 RT 3.6×10^{12}

ions/cm^2 sample. XRD and PL measurements also confirmed that the denoted dose was not correct; the dose should be much lower than 8.8×10^{13} ions/cm^2 because the XRD peak was symmetric and the PL intensity was very intense in this sample. Again, the sample can be considered as unimplanted. The strong absorption was due to implantation induced defects.

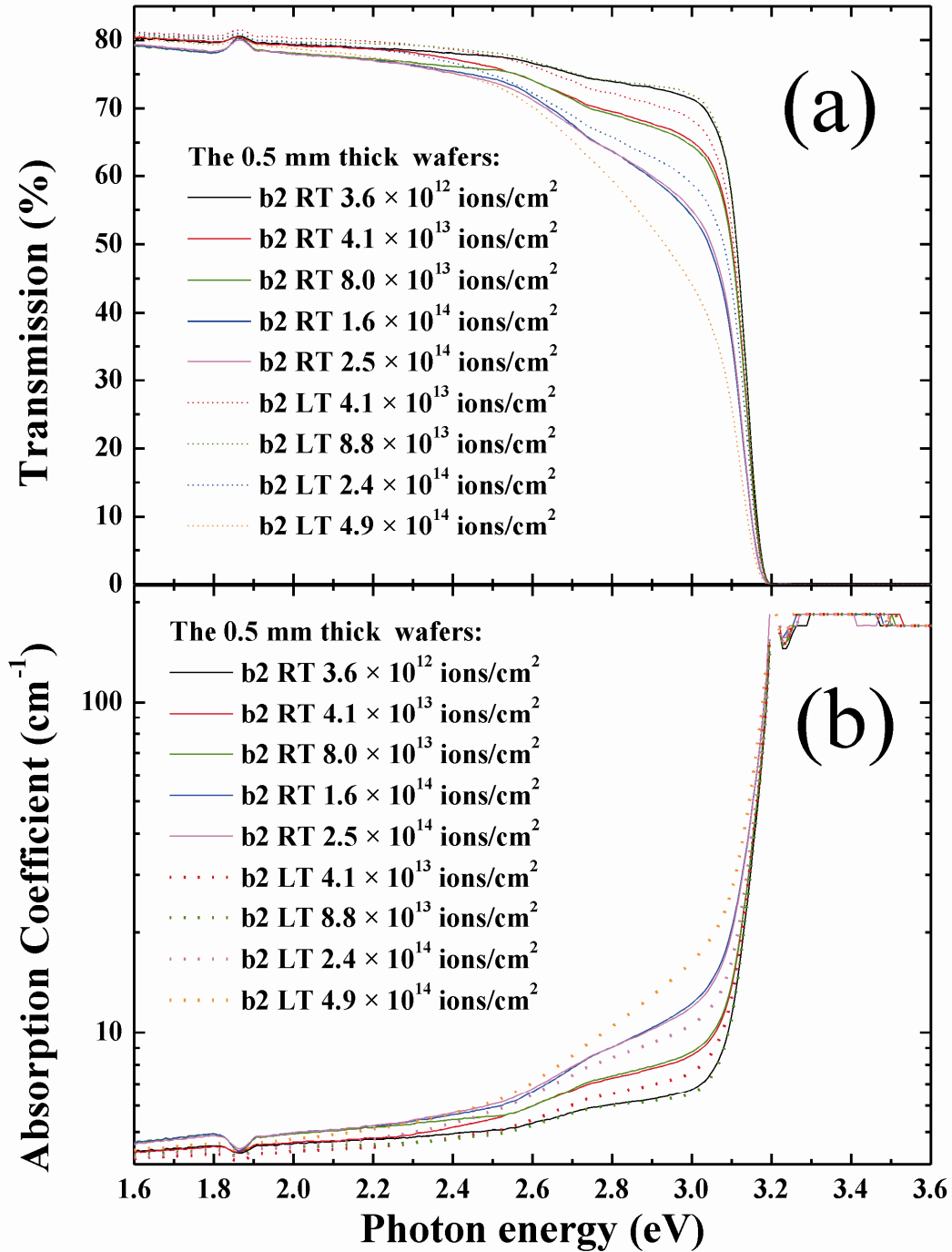**Figure 49. (a) Transmision and (b) Absorption spectra of the batch 2 wafers implanted at room and low temperature.**

Figure 49(b) shows the absorption coefficients of the batch 2 wafers as functions of photon energy. When calculating absorption, it was considered that the samples were uniform across their thickness and the sample thickness was taken to be 0.5 mm. The absorption of the b2 RT 3.6×10^{12} and b2 LT 8.8×10^{13} ions/cm^2 samples at 2.8 eV was approximately 6 cm^{-1}. Strictly speaking, the consideration that the samples were uniform across their thickness was not completely correct because the absorption coefficients of the ultra-thin implanted layers were much larger than the absorption coefficients of unimplanted layers. The absorption coefficients of the implanted layers α_i can be calculated from the relative transmission of the implanted wafers T and b2 RT 3.6×10^{12} ions/cm^2 sample T_0 by the formula:

$$\alpha_i = -\ln(T/T_0)/d$$

where d is the thickness of the implanted layer. According to the SRIM calculation, d was taken to be 50 nm. This formula was derived with assumptions that i) absorption of 50-nm-thick unimplanted layer was negligible in comparison with absorption of the implanted layer of the same thickness and ii) the absorption was uniform across the implanted layer thickness. The second assumption was very rough because the implanted ions did not distribute uniformly across the implanted layer as inferred from the SRIM calculations. Despite this shortcoming the absorption coefficients of the implanted layers are plotted in Figure 50. As can be seen, the absorption coefficients of the implanted layers at 2.8 eV were 5 to 6 orders of magnitude more than that of the "unimplanted" sample. This justifies the first assumption. In addition, in the LT samples the absorption tended to expand to lower photon energy direction as the implantation dosed was increased, namely, abrupt falls (see the dotted lines) occurred at ~2.6, 2.3, and 1.9 eV in the b2 LT 4.1×10^{13}, 2.4×10^{14}, and 4.9×10^{14} ions/cm^2 samples, respectively. In the RT samples, the absorption coefficients' behaviors were qualitatively the same but not as profound as in the LT samples. The abrupt fall at ~2.6 eV was observed in all RT samples and the lower-energy tail was observable in the b2 RT 8.0×10^{13}, 1.6×10^{14}, and 2.5×10^{14} ions/cm^2 samples but not in the b2 RT 4.1×10^{13} sample.
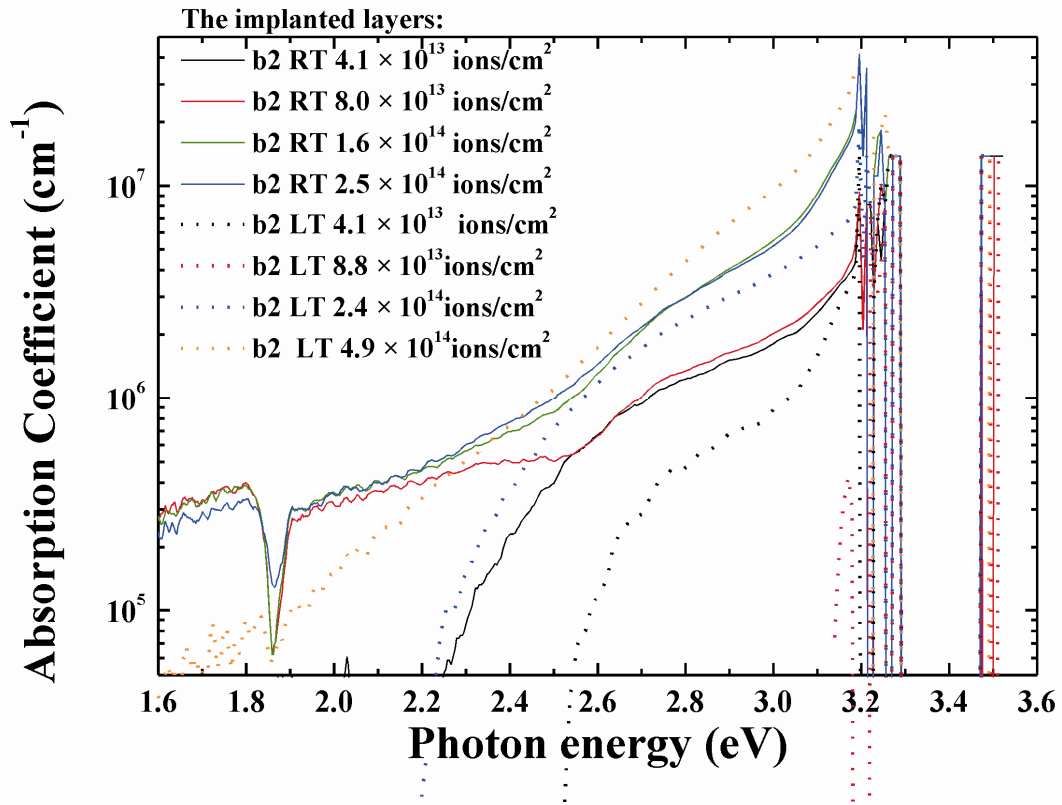
Figure 50. Absorption of the implanted layers (see text).

Reflectance spectra of the b2 samples are depicted in Figure 51. A typical feature of reflectance spectra was observed in the b2 RT 3.6×10^{12} ions/cm^2 and b2 LT 8.8×10^{13} ions/cm^2 samples, namely, reflectance abruptly declined in the photon energy range from 3.05 to 3.2 eV and subsequently increased from 3.2 to 3.3 eV. As the implantation dose was increased, the falling and the rising part became less profound and in the b2 LT 4.9×10^{14} ions/cm^2 the rising part disappeared. Previously, the negative minimum and high-energy-wing maximum were attributed to exciton transitions [111]. It was stated [112, 113] that when the carrier concentration exceeded a screening concentration n_s, electrons and holes could not form an excitons. This may account for the degradation of the mentioned above typical feature with increasing implantation dose. It was also specified [112] that the screening concentration n_s determined an exiton-free layer, whose thickness depended on implantation dose and voltage. This exciton-free layer strongly affected the reflectance spectra. Calculations were conducted to fit the experimental reflectance spectra by the authors of [112]. Similar studies are desirable for the samples in this thesis.

Figure 51. Reflectance spectra of the batch 2 wafers implanted with 60 keV Sn+ ions at room and low temperatures.

4.7 Photoluminescence of the batch 2 RT samples

4.7.1 Excitation-power and temperature dependent PL of the batch 2 RT 3.6×10^{12} ions/cm^2 sample
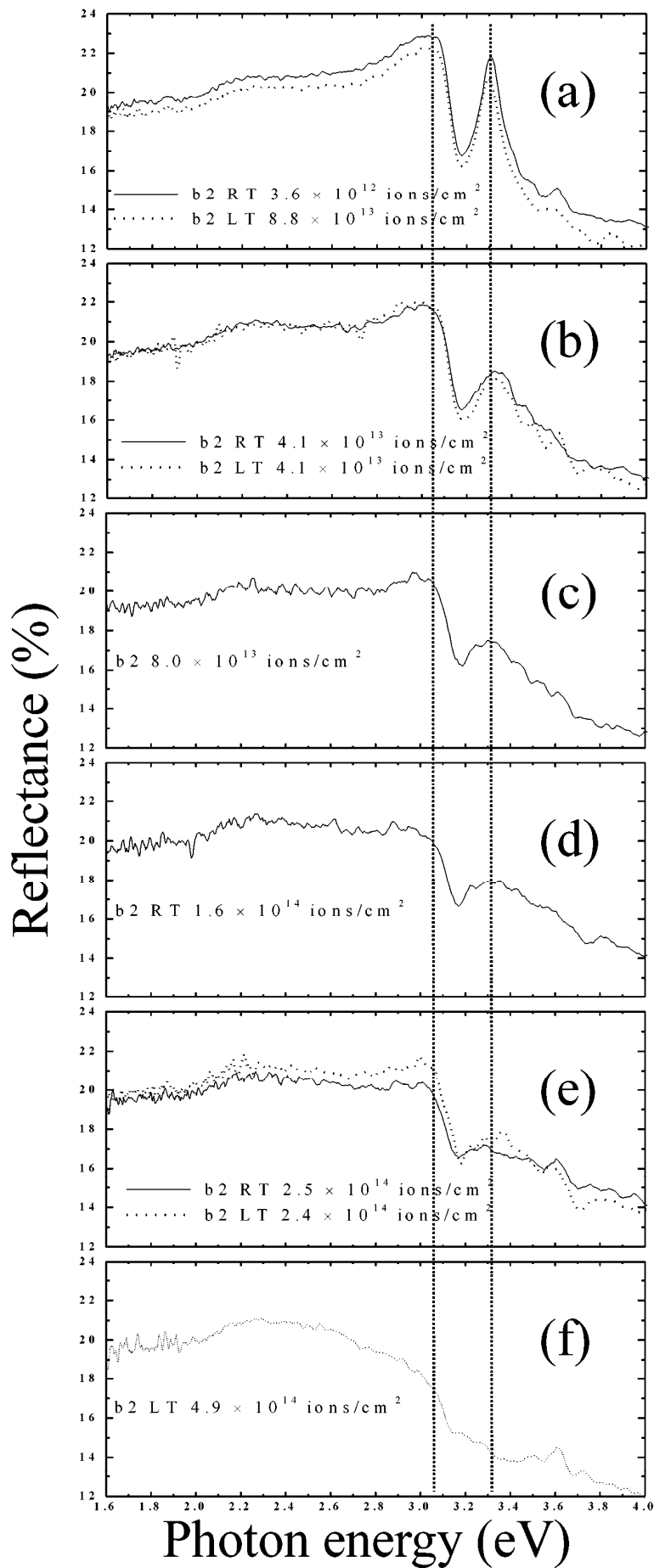
All measurements in this section was conducted in the b2 RT 3.6×10^{12} sample, whose PL was considered to be similar to that of bulk hydrothermal ZnO

Excitation dependence of ZnO NBE PL in the temperature range from 5 to 300 K.

Figure 52(a) shows the PL spectra measured at 5 K with numerous excitation powers. In the spectrum measured at 0.36 mW two intense peaks can be observed at 3.356 and 3.361 eV; they were attributed to the neutral-donor-bound A exciton (DBX$_A$) transitions I$_9$ and I$_6$, respectively [2, 55, 66]. Faint shoulders appeared around 3.32, 3.366, 3.379, and 3.390 eV; they were assigned to the two-electron satellite (TES), DBX I$_3$, free A exciton (FX$_A$), and free B exciton (FX$_B$) transitions, respectively [2, 55]. Several authors [114, 115] have assigned the transitions at 3.315 eV or 3.325 eV to the acceptor-bound exciton (ABX) transition. Due to the n-type conductivity nature of the current sample, I consider the assignment of the transition at 3.32 eV [see Figure 52(a)] to the ABX transition unlikely. As the excitation power was increased, the broadening of the I$_9$ peak occurred, which caused the I$_6$ and I$_3$ transitions indiscernible. In addition, the I$_9$ peak red-shifted with excitation power. The red-shift of the most intense peak (I$_9$ at low temperature and low excitation power) with excitation power appeared in PL spectra measured at every fixed temperature in the range from 5 to 298 K. This was partly illustrated in Figure 52(b), which plots PL spectra measured at 298 K. The peak shifted from 3.272 eV at 0.36 mW excitation power to 3.262 eV at 7.51 mW. It should be noted that a faint shoulder appeared at approximately 3.12 eV when the excitation power exceeded 0.76 mW. This feature was attributed to the second LO-phonon replica of the most intense peak due to the separation of approximately 140 meV with respect to the most intense peak [116, 117]. The first LO-phonon replica probably merged into the TES transition and/or the most intense peak itself.
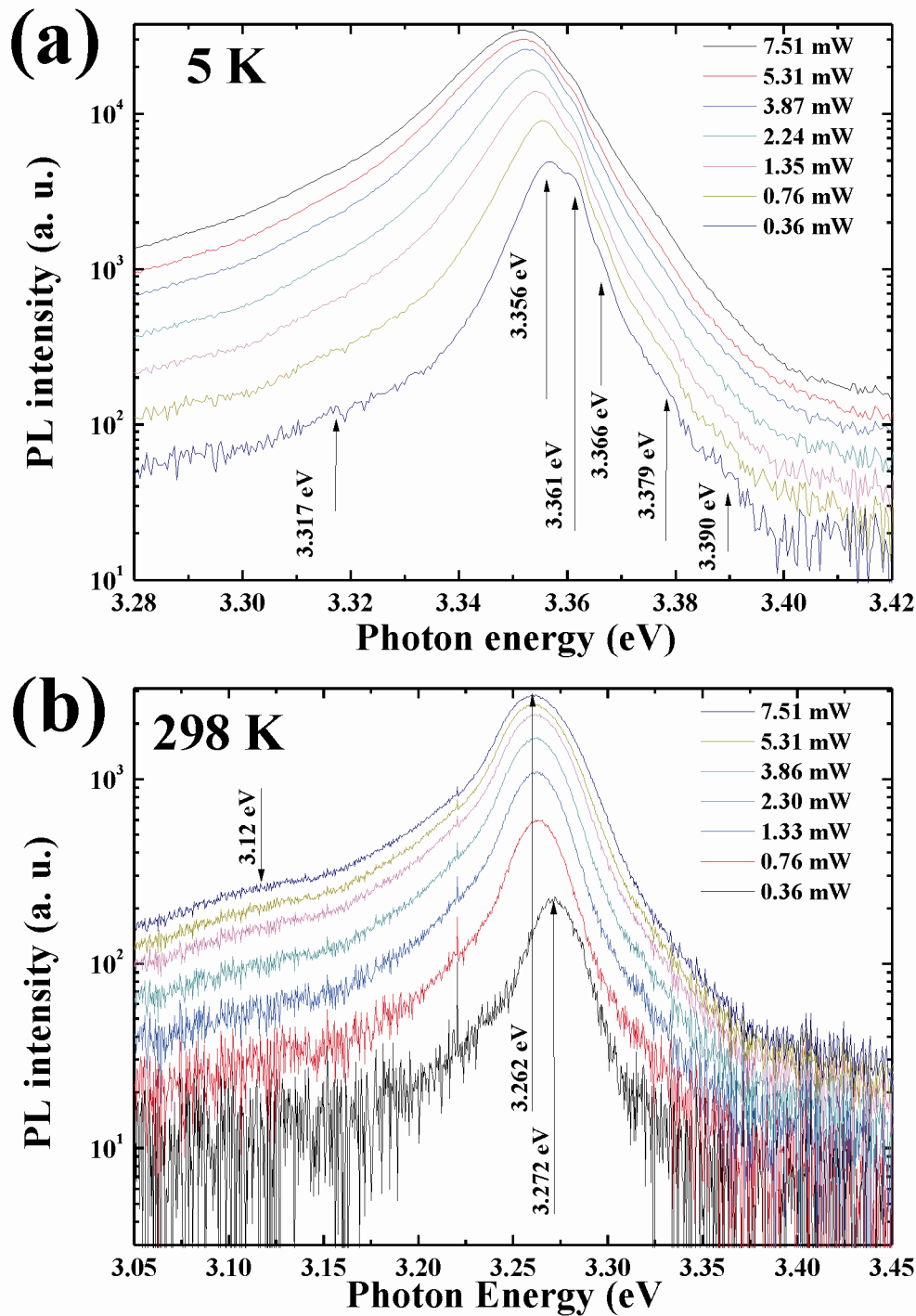
Figure 52. PL spectra measured by means of a Q-switched pulsed laser with numerous excitation powers in the range from 0.33 mW to 7.51 mW at (a) 5 K and (b) 298 K. (Princeton system).

At first, local heating was suggested as a primary reason for the red-shift, e.g. when the excitation power was increased, the excited area was heated up locally, and a temperature increase led to the red-shift in the most intense peak. Below, evidence is put forward to show that the suggestion was not correct in this case. Figure 53 demonstrates the PL spectra measured in the second-order dispersion of the grating at 5 K with numerous excitation powers. In comparison with the spectra measured in the first-order grating configuration [see Figure 52(a)],

the transitions were better resolved, and the energies of the transitions were slightly different but within the experimental error except for the TES transition at 3.311 eV, which was approximately 10 meV below the position determined in Fig. 1(a). Due to the better resolution, it can be clearly seen that i) relative intensities of the transitions I_9 and I_6 increased with excitation power and ii) the red-shift with excitation power occurred just in the position of the DBX_A transition I_9, position of other transitions remained almost unchanged. If the red-shift was caused by the temperature increase, it should occur in all transitions. The last contention was evident in Figure 54, which plots the PL spectra measured at temperatures from 5 to 65 K. Though rather difficult, one could realize that both the DBX transitions I_9 and I_6 red-shifted with increasing temperature. However, one could argue that the temperature increase caused by the increase in excitation power at 5 K was much smaller than 65 K. The argument can be refuted as follows. At 5 K, the increase in excitation power from 0.33 to 7.50 mW caused the peak to shift from 3.3566 to 3.3517 eV. Suppose that the temperature did not increase at the minimal excitation power of 0.33 mW, the peak at 3.3517 eV would correspond to the temperature of approximately 70 K (see below), which was well higher than 65 K. Thus, it was conclusively proven that red-shift in the I_9 peak with excitation power was not caused by local heating.
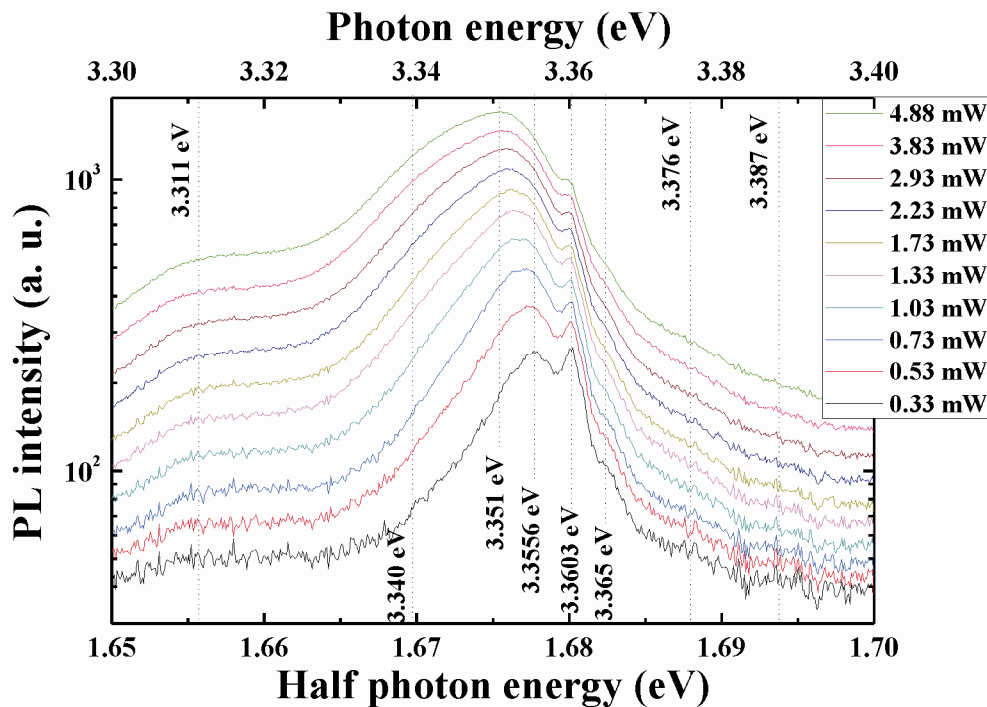

Figure 53. PL spectra measured in the second-order grating configuration at 5 K by means of a Q-switched pulsed laser. (Princeton system).
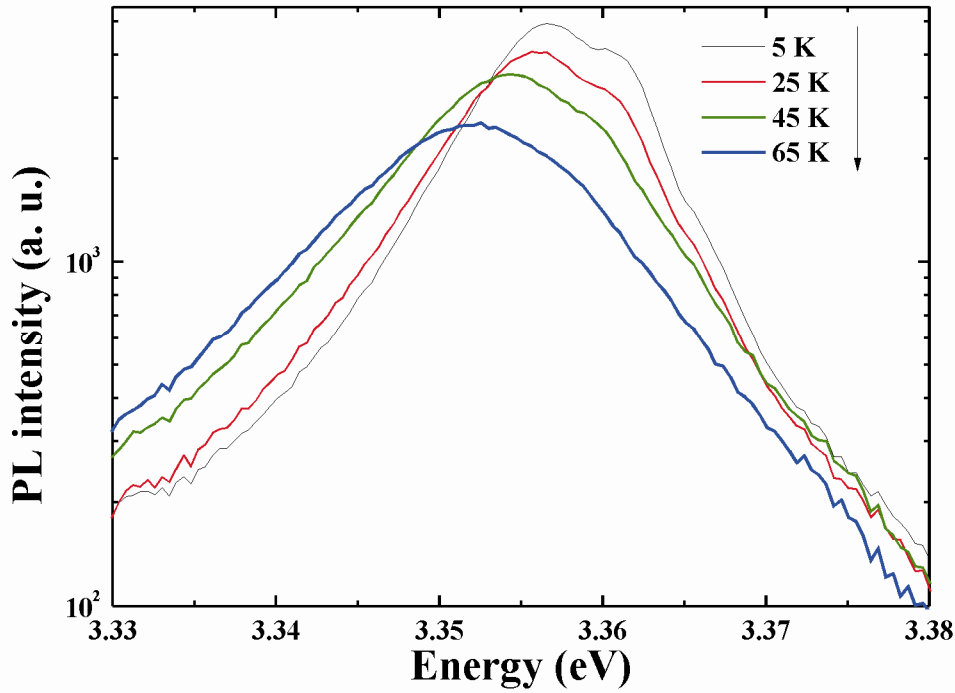
Figure 54. PL spectra measured in the temperature range from 5 to 65 K by means of a Q-switched pulsed laser at 0.33 mW excitation power. (Princeton System).

Figure 53 also suggests another explanation for the red-shift. It can be seen that at the maximal excitation power of 4.88 mW a faint shoulder appeared around 3.34 eV. This shoulder was not discernible at low excitation powers, but its intensity became comparable with the I_9 peak at 4.88 mW excitation power. The shoulder can be attributed to the TES transition of the DBX transition I_3 [55]. Apparently, as the excitation power was increased, the DBX I_9 transition was saturated, more and more photo-excited carriers relaxed to lower (than I_9) energy levels, therefore, lower energy transitions became more intense. These transitions also overlapped with the DBX_A I_9 transition. As a result, the merged peak shifted toward lower energy position. The lower energy transitions, which caused the red-shift of the I_9 peak, could be the TES transition at 3.34 eV, but more likely were the bound excitons I_{10} at 3.3530 eV and/or I_{11} at 3.3481 eV [55].

Figure 55 (a) and Figure 55(b) depict room-temperature PL spectra excited by the 266 nm line of a Q-switched pulsed laser and the 325 nm line of a cw He-Cd laser, respectively. As the excitation power was increased from 0.02 mW to 1.70 mW, pulsed laser excitation caused the PL peak to shift from 3.303 eV to 3.281 eV, whereas the cw laser excitation caused no shifts, the peak remained at approximately 3.302 eV. At 1 mW excitation power of the Q-switched pulsed laser, the photon density of one pulse was estimated to be 6.9×10^{13} photons/cm^2. During the time period equal to the pulse duration of 10 ns, the photon density of the cw laser 1 mW excitation power was approximately 6.3×10^{10} photons/cm^2. This density was by three orders of magnitude smaller than the pulse photon density; therefore, it was probably insufficient to

saturate the I_9 transition. In fact, when the pulsed excitation power was decreased to 0.02 mW (1.4×10^{12} photons/cm^2), the peak position (3.303 eV) was close to the cw laser excited peak (3.302 eV). It should be noted that a rather large variance exists in peak position observed in Figure 55 and that in Figure 52(b). This problem may result from i) the fact that higher photon density was utilized to measure the PL spectra in Figure 52(b) and/or ii) different calibration precision in the two measurement systems. However, the red-shift was unique to pulsed laser excitation as confirmed by both measurement systems.
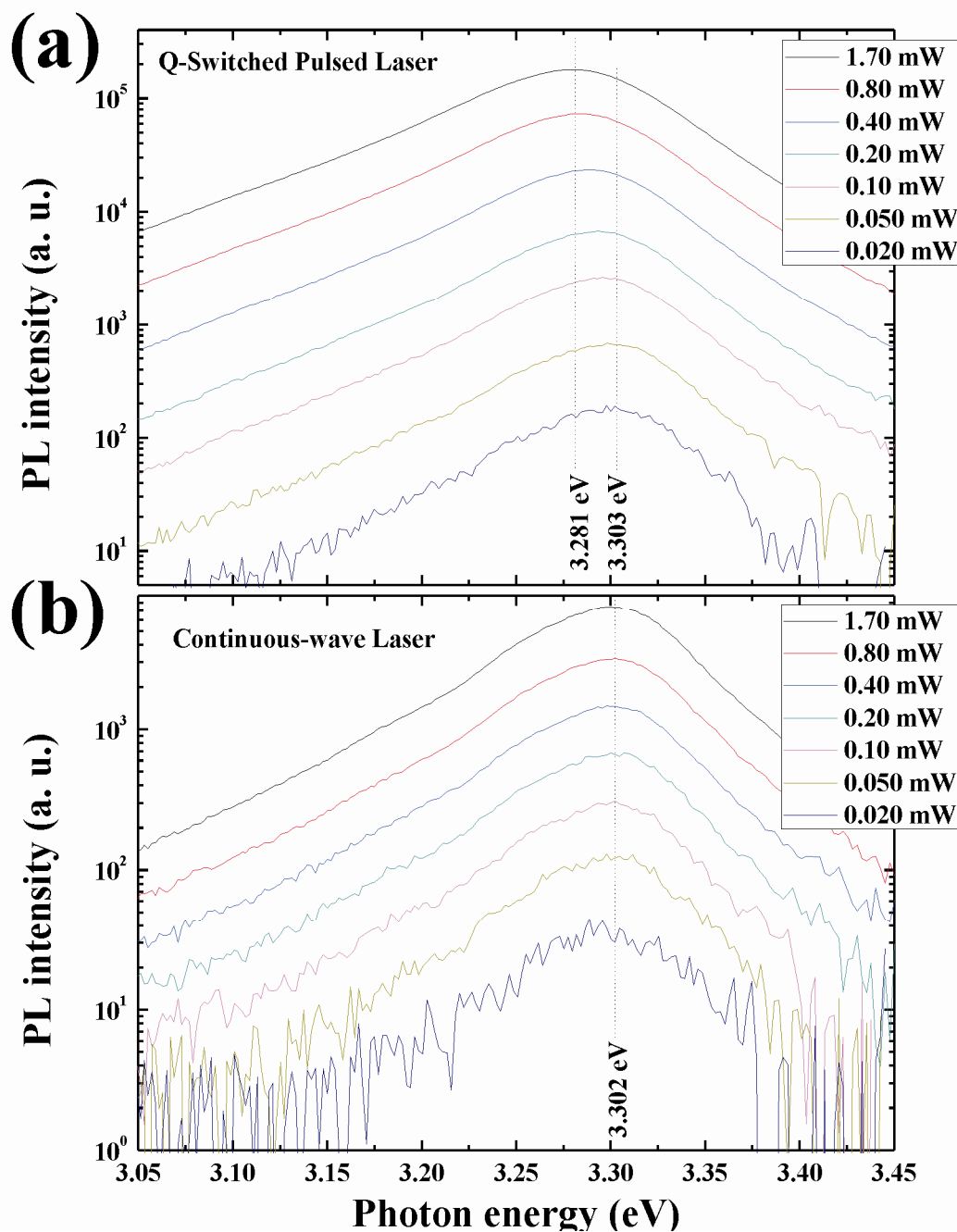

Figure 55. Room temperature PL spectra excited by means of (a) a Q-switched pulsed laser and (b) a continuous-wave He-Cd laser. (Hobira system)

Following the approach of Zhang *et al.* [68], we plotted the position of the most intense peak (I_9 at low temperature and low excitation power) as a function of temperature for all excitation powers. A typical variance of less than 3% was maintained for every excitation power except for the lowest excitation power of 0.33 ± 0.02 mW. Subsequently, the temperature dependences were fitted with the Varshni equation [118]: $E(T) = E(0) - \alpha T^2 /(T + \beta)$; where $E(0)$ and $E(T)$ are energies at temperatures 0 and T, respectively, α and β are so-called Varshni coefficients. In the original paper of Varshni [118], $E(0)$ and $E(T)$ denoted band gap energies; however, in later studies, they also denoted energies of various excitonic transitions [67-74]. Shown in Figure 56 are representative experimental data for the excitation powers of 0.33 ± 0.02, 1.34 ± 0.04, and 7.50 ± 0.05 mW and corresponding Varshni fits. It can be seen that the Varshni equation satisfactorily fitted the experimental data points. The arrows in Figure 56 indicate that the peak position in the PL spectrum measured at 5 K and 7.50 mW would correspond to that measured at 70 K and 0.33 mW. Excitation power dependences of the fitting parameters $E(0)$, α, and β are demonstrated in Figure 57(a)-(c), respectively. Generally, $E(0)$, α, and β decreased with excitation powers and asymptotically reached the values of approximately 3.352 ± 0.001 eV, $(5.0 \pm 0.5) \times 10^{-4}$ eV/K, and 200 ± 50 K, respectively. In addition, α varied in the range $5.0-16 \times 10^{-4}$ eV/K as excitation power decreased from 7.50 mW to 0.33 mW, whereas β in the range 200–1400 K.
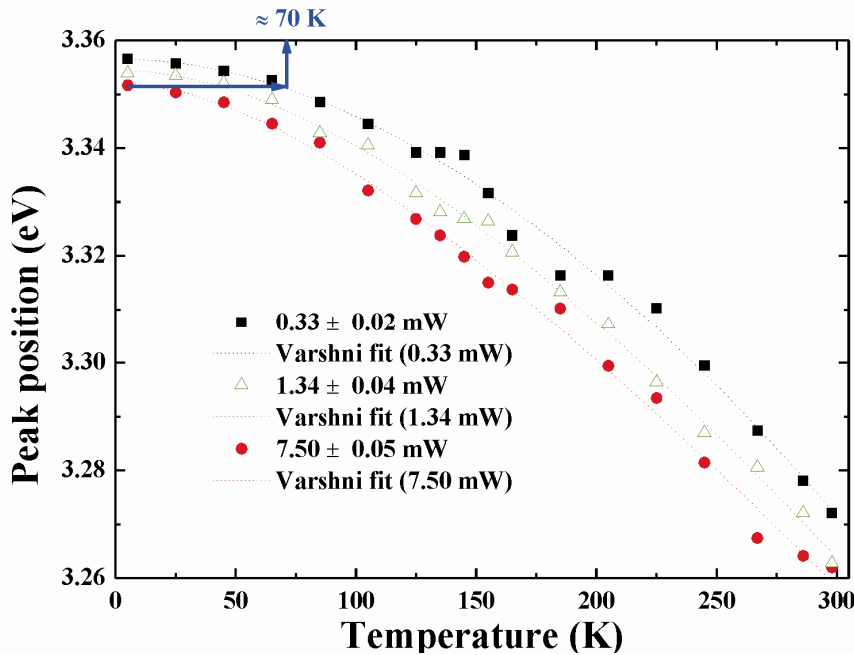
Figure 56. Temperature dependences of the most intense PL peak (the DBXA I9 peak at low temperature and low excitation power) energy measured with excitation powers of 0.33 ± 0.02 mW (solid squares), 1.34 ± 0.04 (empty triangles), and 7.5 ± 0.05 mW (solid cirles) along with corresponding Varshni fits (dotted lines).
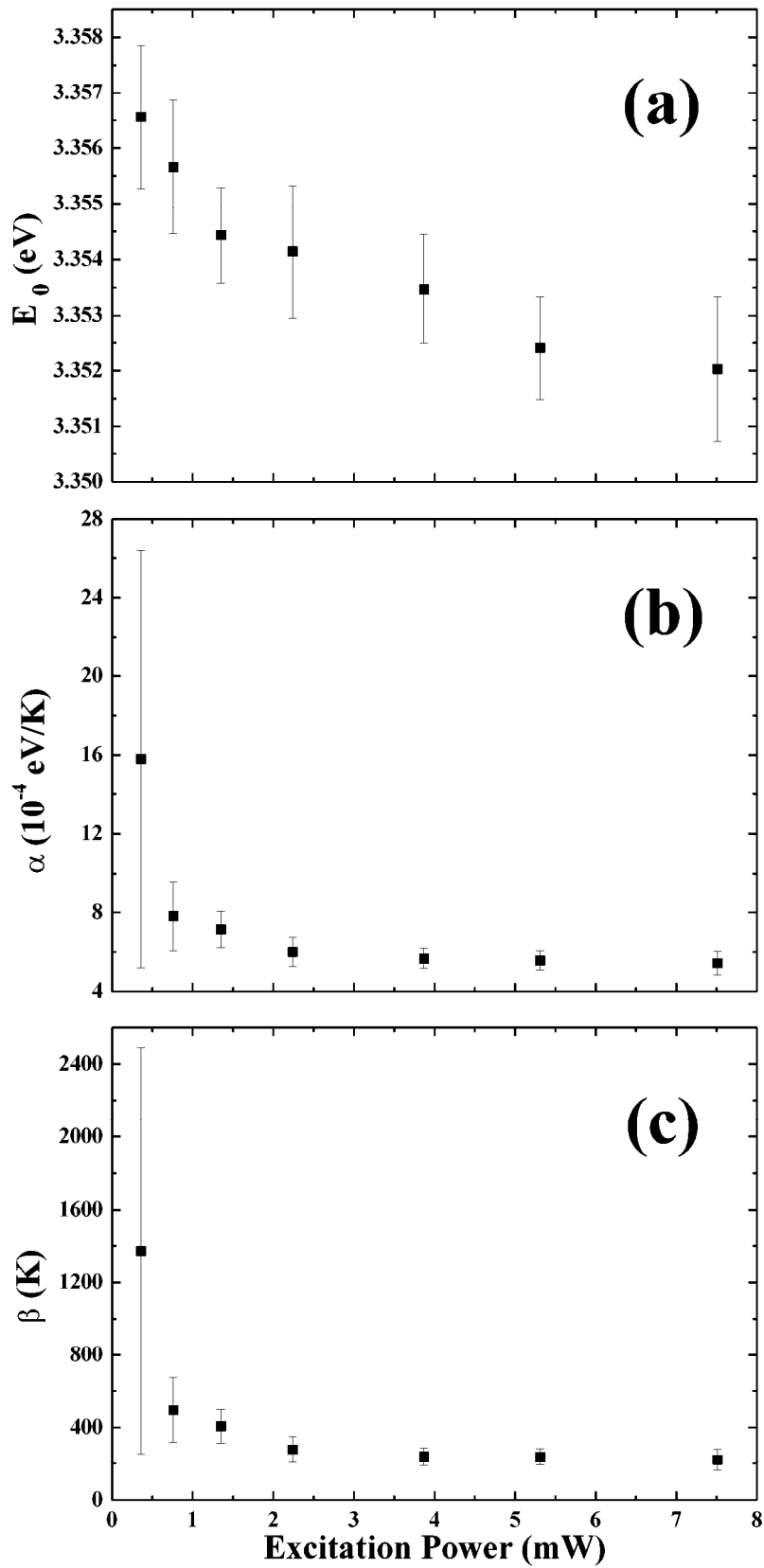
Figure 57. The pulsed laser excitation power dependences of the Varshni fitting parameters (a) E(0) , (b) α, and (c) β.

93

Table 3 lists the values of the coefficients α and β reported in previous studies [67-74]. As can be seen, the reported values of α and β varied in the range 6.7–13.9 × 10^{-4} eV/K and 700–1077 K, respectively, except for the reported by Li *et al.* [72] data, which were unrealistically high ($\alpha = 58.7 \times 10^{-4}$ eV/K and $\beta = 4249$ K). In the current study, the values of α and β at 0.33 mW excitation power could not be precisely determined due to the large experimental error. However, those at 0.76 mW excitation power [$\alpha = (7.8 \pm 1.8) \times 10^{-4}$ eV/K and $\beta = 500 \pm 180$ K] were comparable with results of previous studies. At higher excitation powers, α and β became considerably smaller than the reported values. It should be noted that most studies[67, 69-73] cited in Table I utilized a cw He-Cd laser as a excitation source except for the study of Zhang *et al.* [68] and Cao *et al.* [74], which utilized 150 fs laser pulses and a quasi-continuous-wave Ti: sapphire laser, respectively. Our study indicates that if one utilizes pulsed laser excitation, the effect of excitation power on the coefficients α and β can not be neglected.

Table 3. Varshni equation's fitting parameters E(0), a, and b in literature.

Structure, growth method	E(0) (eV)	Claimed origin	α (10^{-4} eV/K)	β (K)	Excitation source
Thin film, mist chemical vapor deposition[a]	3.360	DX	8.0	775	cw He-Cd laser (325 nm)
Nanorods, vapor phase transport[b]	3.355	FX	10.7	727	Ti: sapphire 150 fs pulse (325 nm)
Polycrystalline thin films, rf-magneton sputtering[c]	3.366	FX	13.9	900	cw He-Cd laser (325 nm)
Film, rf-plasma assisted MBE[d]	3.3772	FX	7.2	1077	cw He-Cd laser (325 nm)
	3.3651	DBX			
	3.3312	ABX			
Bulk[e]	3.377	FX	11	920	cw He-Cd laser (325 nm)
	3.360	DBX	6.7	920	
Nanorods, vapor-phase[f]	3.381	FX	58.7	4249	cw He-Cd laser (325 nm)
Bulk seeded-chemical-vapor-transport[g]	3.380	FX$_A$	8.2	700	cw He-Cd laser (325 nm)
Nanoneeddle array, template-free electrochemical deposition[h]	3.379		7.5	1050	Quasi-continuous-wave Ti: sapphire (267 nm)

[a]See [67]

[b]See [68]

[c]See [69]

[d]See [70]

[e]See [71]

[f]See [72]

[g]See [73]

[h]See [74]

ZnO deep-level PL in the temperature range from 5 to 300 K.

The wide-range PL spectra measured at 5 K by means of the Q-switched pulsed-laser excitation are shown in Figure 58. Similar to the NBE I_9 peak, the DL band appeared to red-shift with excitation power. For instance, at 0.33 mW excitation power the band peaked at ~2.096 eV and at 4.88 mW peaked at ~2.060 eV. Figure 59 plots representative PL spectra measured at 4.88 mW excitation power at temperatures in the range from 5 to 300 K. Interestingly, the DL band blue-shifted with temperature instead of red-shift as in the case of the NBE peak. Such abnormal dependence of the DL band was also reported previously by Cao *et al.* [74] and Ahn *et al.* [119]. Figure 60 depicts temperature dependence of the DL band peak. Due to the broad FWHM of the band and the low signal-to-noise ratio, the error in the peak position was estimated to be 0.014 eV. The band peak energies belonged to the orange-yellow region. Figure 61(a) and (b) show the wide-range RT spectra measured at numerous excitation powers from the Q-switched pulsed and cw lasers. Differing from the PL spectra measured at 5 K by means of the Q-switched pulsed laser excitation, the DL band measured by means of the cw laser excitation blue-shifted with excitation power [see Figure 61(b)]. For example, the DL band peaked at 2.42 eV at 0.020 mW excitation power and peaked at ~2.52 eV and at 1.7 mW. Meanwhile, determination of the DL band peak in the Q-switched pulsed laser excitation room-temperature PL spectra was difficult [see Figure 61(b)] due to the broadening of the NBE band. Nevertheless, it appears that the band red-shifted with excitation power and the intensity of the orange-yellow region (around 2.1 eV) was comparable with that of the green region (around 2.5 eV). Another interesting feature is that the relative intensity of DL and NBE bands in the Q-switched pulsed laser excitation was roughly one order of magnitude smaller than that in the cw laser excitation (see Figure 61). The mentioned above characteristics would be useful in determination of the origins of the green and yellow-orange PL bands.
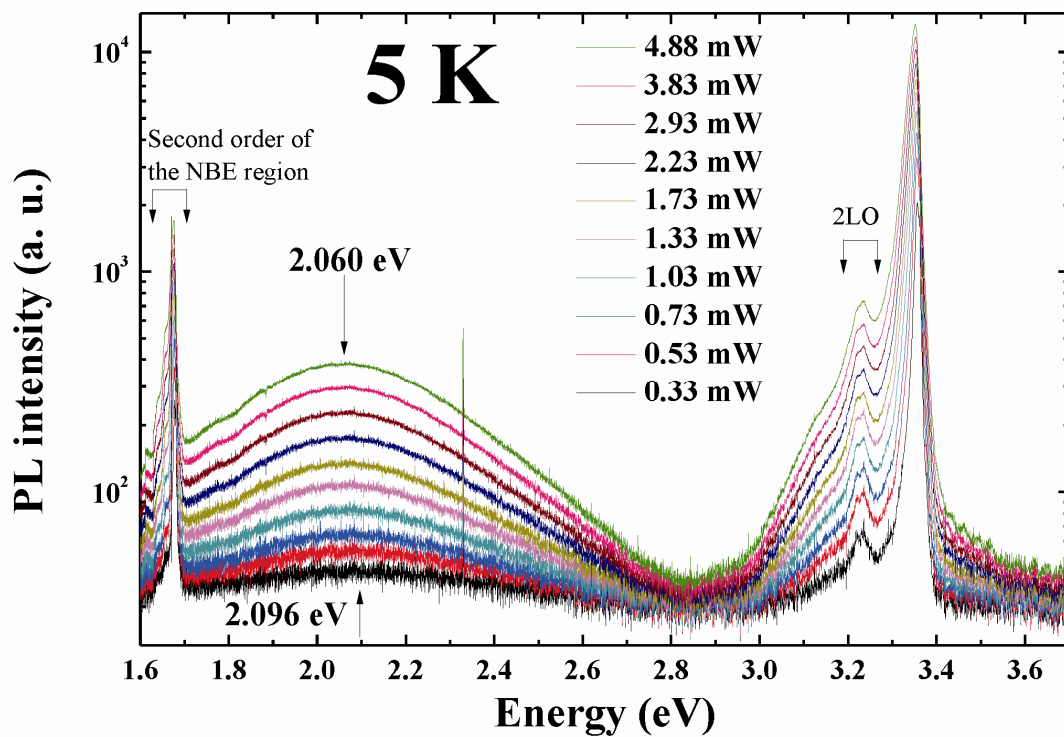
Figure 58. Wide-range PL spectra measured by means of a Q-switched pulsed laser with numerous excitation powers in the range from 0.33 mW to 7.51 mW at 5 K. (Priceton system).
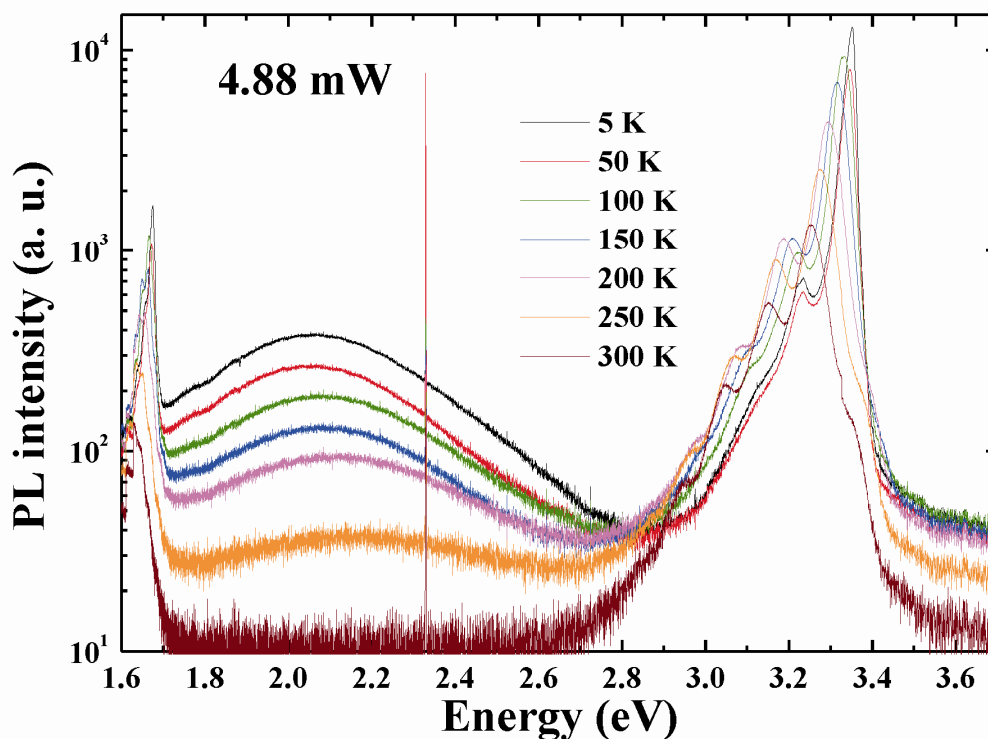
Figure 59. Some representative wide-range PL spectra measured in the temperature range from 5 to 300 K by means of a Q-switched pulsed laser at 4.88 mW excitation power. (Princeton system).
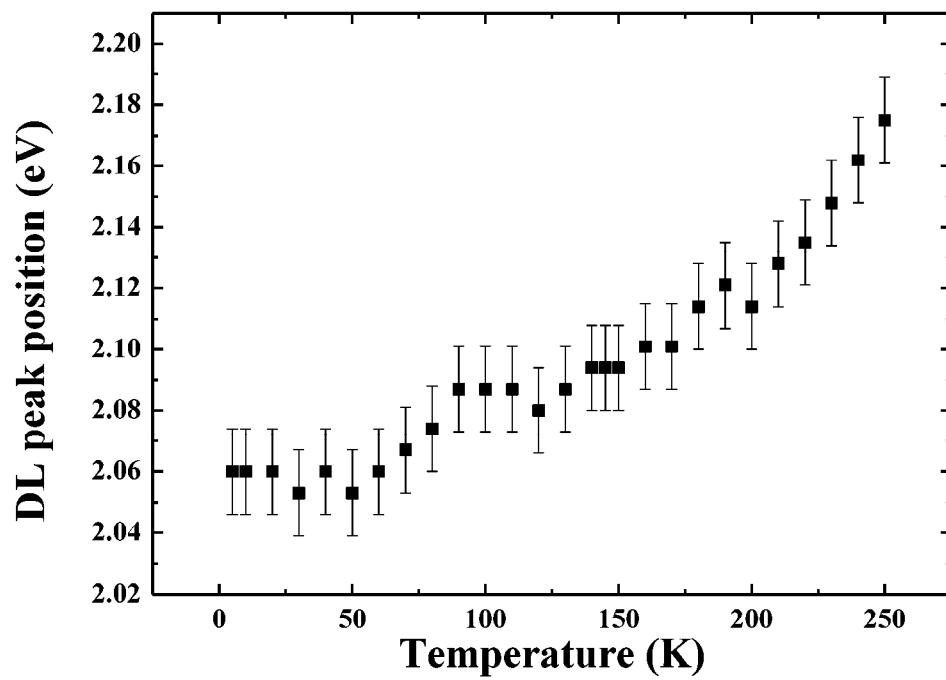
Figure 60. Temperature dependence of the near-band-edge PL peak.
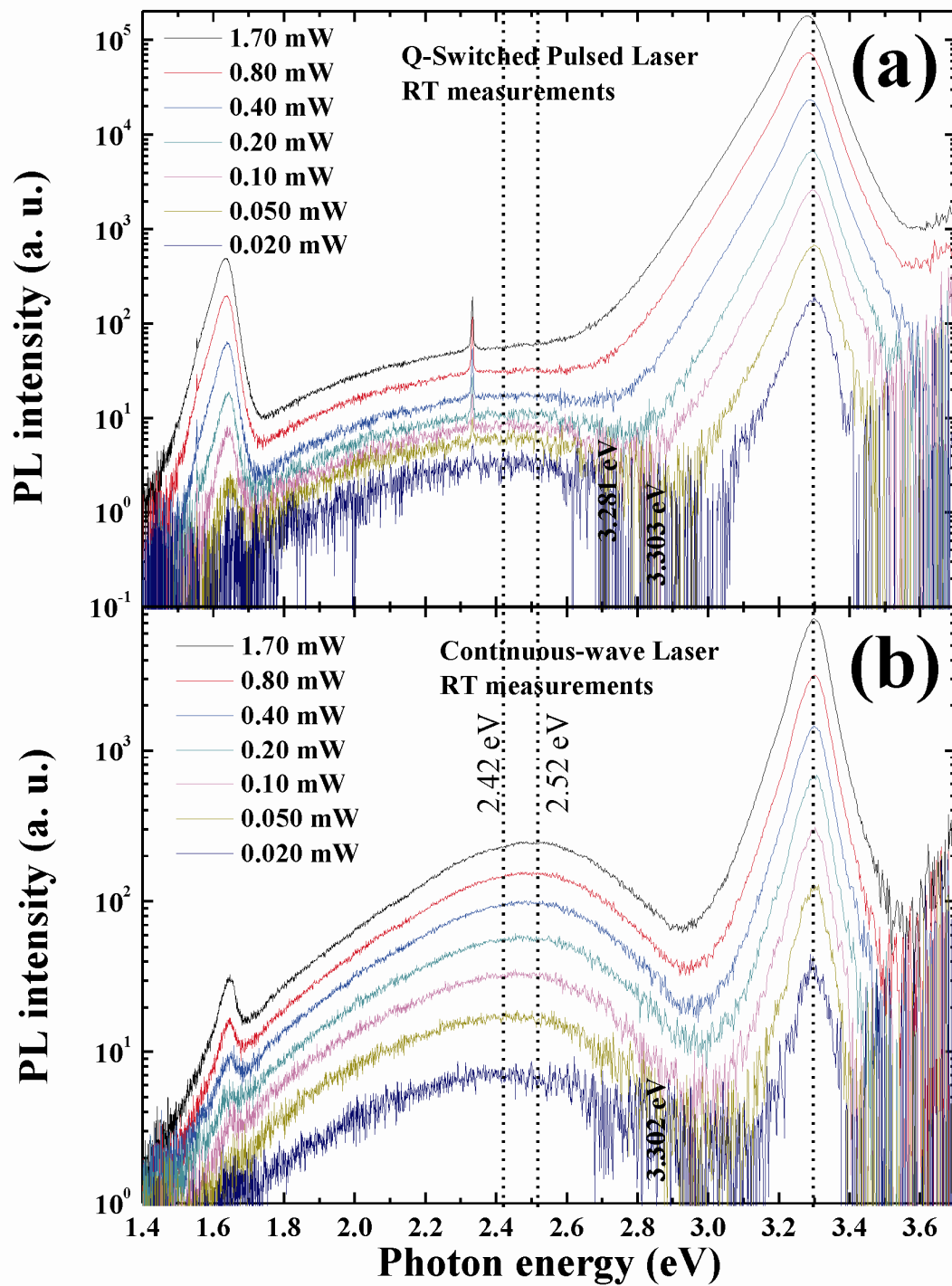
Figure 61. Wide-range room temperature PL spectra excited by means of (a) a Q-switched pulsed laser and (b) a continuous-wave He-Cd laser.(Honbira system).

4.7.2 Room temperature PL of the batch 2 RT samples

PL spectra of the batch 2 RT samples are depicted in (Figure 62). Note that the unimplanted ZnO PL spectrum was measured in the unimplanted area on the surface of the 3.6×10^{12} sample. As can be seen, two regions appeared in the unimplanted ZnO PL spectrum: the near-band-edge (NBE) region peaking at 3.278 eV (378 nm) and the deep level (DL) region peaking at 2.48 eV

(500 nm). At an implantation dose as low as 3.6×10^{12} ions/cm^2, the ZnO wafer remained intact, which was evident in the similarity of the PL spectra of the unimplated and implanted areas. However, when the implantation dose was increased to 4.1×10^{13} ions/cm^2, the PL intensity decreased significantly, by more than two orders of magnitude. This casts doubt on the previous claim that a high level of dynamic annealing makes ZnO highly resistant to implantation-induced damages [54]. A further increase in implantation dose caused a gradual decrease in PL intensity of both NBE and DL regions. In addition, the DL region peak red-shifted with implantation dose. Absorbance of the implanted samples also illustrates the same tendency; namely, the absorbance edge red-shifted with implantation dose (see Figure 50). The red-shift was reported previously in hydrothermal ZnO irradiated with 4 MeV electrons [82]. According to [82], electron irradiation could not introduce new impurity-related defects but the red-shift still occurred; similarly, in the current study most likely Sn$^+$-related defects did not cause the red-shift of the DL band. AFM measurements (see Figure 47) show that the RMS roughness of the wafers implanted to doses of 3.6×10^{12}, 4.1×10^{13}, 8×10^{13}, and 1.6×10^{14} ions/cm^2 was just slightly different, whereas the PL intensity of the 3.6×10^{12} sample was by more than two orders of magnitude larger than that of the other samples (see Figure 62). The AFM measurements indicate that surface variation was not the main reason for the abrupt decrease in PL intensity. The sharpness of the characteristic feature in the reflectance spectra (see Figure 51) also did not degrade abruptly like in the PL case. This suggests that number of electron-hole pairs created by the laser excitation did not decrease abruptly; whereas the lifetime of these electron-hole pairs may abruptly decrease via non-radiative channels. The PL decrease was probably caused by implantation-induced non-radiative defects inside the implanted layer rather than on the surface.
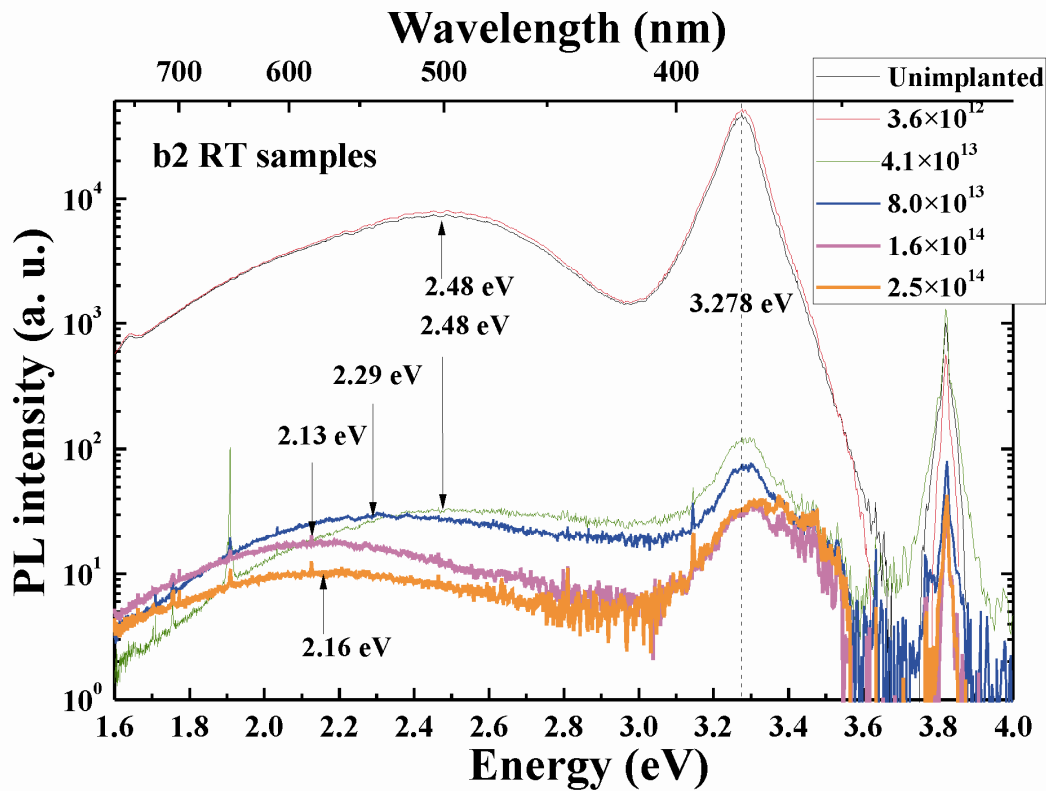
Figure 62. PL spectra of batch 2 ZnO wafers implanted at RT with 60 keV Sn+ to doses in the range from 3.6 × 10^{12} to 2.5 × 10^{14} ions/cm².

In Figure 63, the effect of illumination on PL behaviors of the ZnO wafers is demonstrated. The samples were illuminated with 60 W/cm² laser (the same 325 nm He-Cd laser line) for numerous illumination times. Shown in Figure 63(a)-(d) are the PL spectra of the b2 RT 4.1 × 10^{13}, 8.0 × 10^{13}, 1.6 × 10^{14}, and 2.5 × 10^{14} samples, respectively, after numerous illumination times. As can be observed, in the four samples the PL intensity and position of the NBE peak remained almost unchanged; whereas the DL peak blue-shifted. The DL band intensity of the b2 RT 4.1 × 10^{13} sample decreased with illumination time. Meanwhile, the DL band intensity of other samples first increased and then steadily decreased with illumination time. Note that all these variations were irreversible. The observations are quantitatively detailed in Figure 64, Figure 65, and Figure 66. Figure 64(a) shows that after an initial increase the DL band peak energy saturated at approximately 2.55 eV in the b2 RT 4.1 × 10^{13}, 8.0 × 10^{13} sample and at 2.4 eV in the b2 RT 1.6 × 10^{14} and 2.5 × 10^{14} samples. The PL intensity was integrated in the ranges from 3.099 to 3.541 eV for the NBE region and from 1.983 to 2.916 for the DL region. The integrated PL intensities of the NBE and DL regions were normalized by the maximum integrated PL intensity and then were depicted as functions of illumination time in Figure 65. In all the four samples, the fluctuation of the NBE band intensity was smaller than 10 %, except for the 2.5 × 10^{14} sample. This fluctuation was probably due to the fluctuation in the laser excitation

power. Meanwhile, the variation of the DL band intensity was more than 60 % at least. In addition, the illumination time dependence of the DL band intensity did not follow that of the NBE band intensity. Thus, the fluctuation of the laser excitation power was not the main cause for the variation of the DL band intensity. It appears in Figure 66(a) that the DL band PL intensity decreased more slowly with illumination time in the higher implantation dose sample. In addition, the initial growth stage lasted for shorter time as the implantation dose was decreased [see Figure 66(b)]. In particular, in the 4.1×10^{13} sample the initial growth of PL intensity did not occur [see Figure 66(b)]. These data indicate that implantation-induced defects, which resulted in the red-shift of the DL band, were eliminated by illumination with the He-Cd laser 325-nm line; consequently, the band blue-shifted.
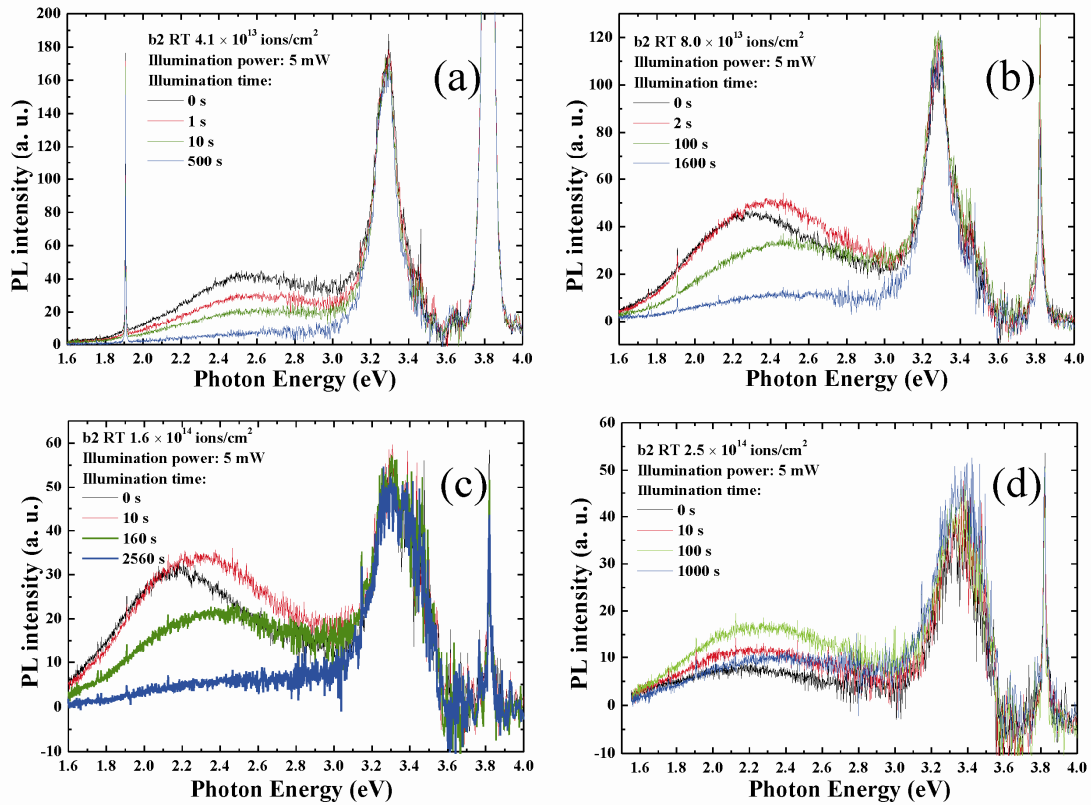
Figure 63. PL spectra of the b2 RT (a) 4.1×10^{13}, (b) 8.0×10^{13}, (c) 1.6×10^{14}, and (d) 2.5×10^{14} ions/cm^2 samples after illuminated with the 5 mW 325 nm line of a cw He-Cd laser for numerous illumination times..
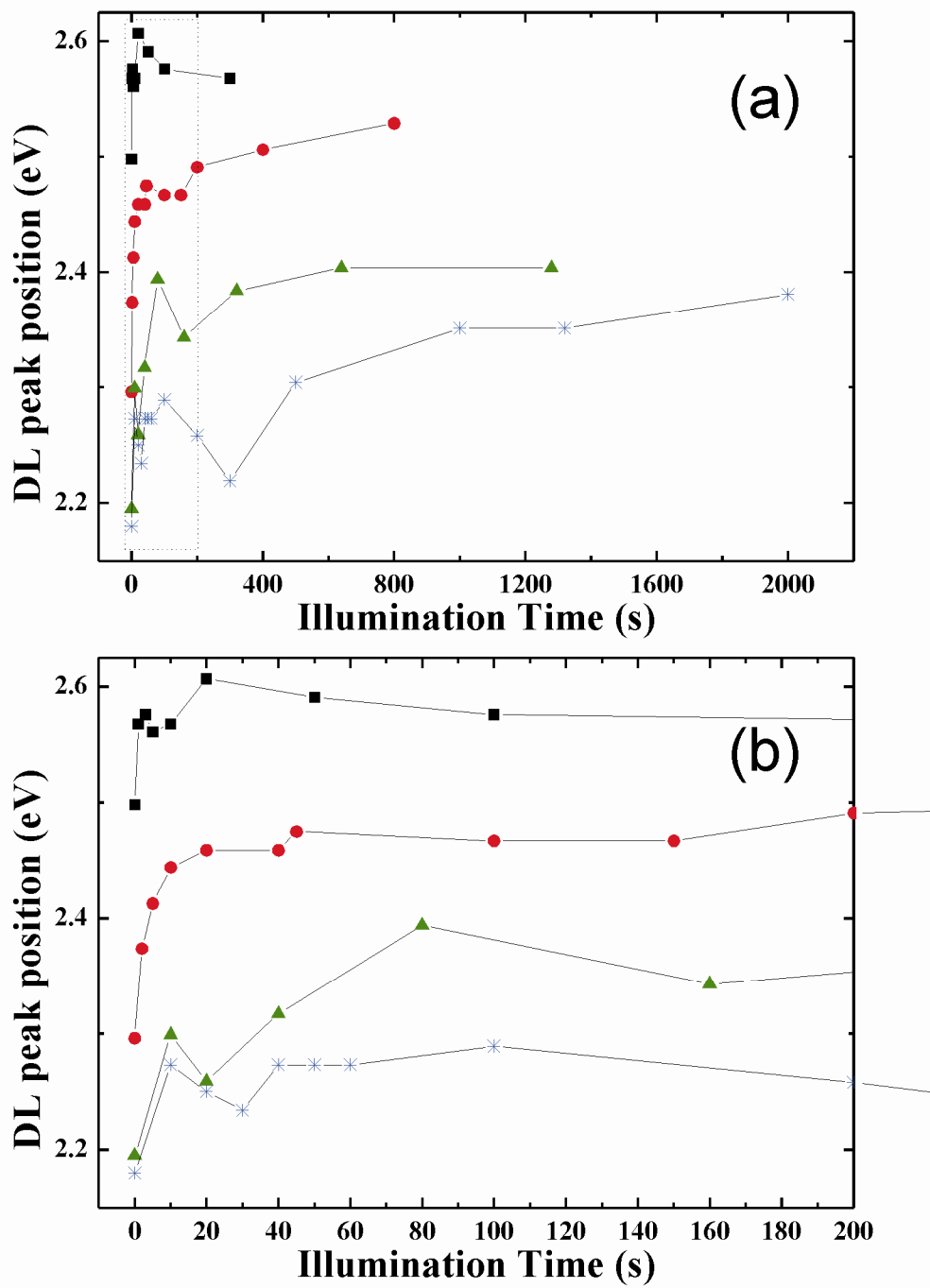
Figure 64. (a) Dependences of the DL peak position in the b2 RT samples and (b) detailed-view of the region hedged by the rectangle in the top figure.
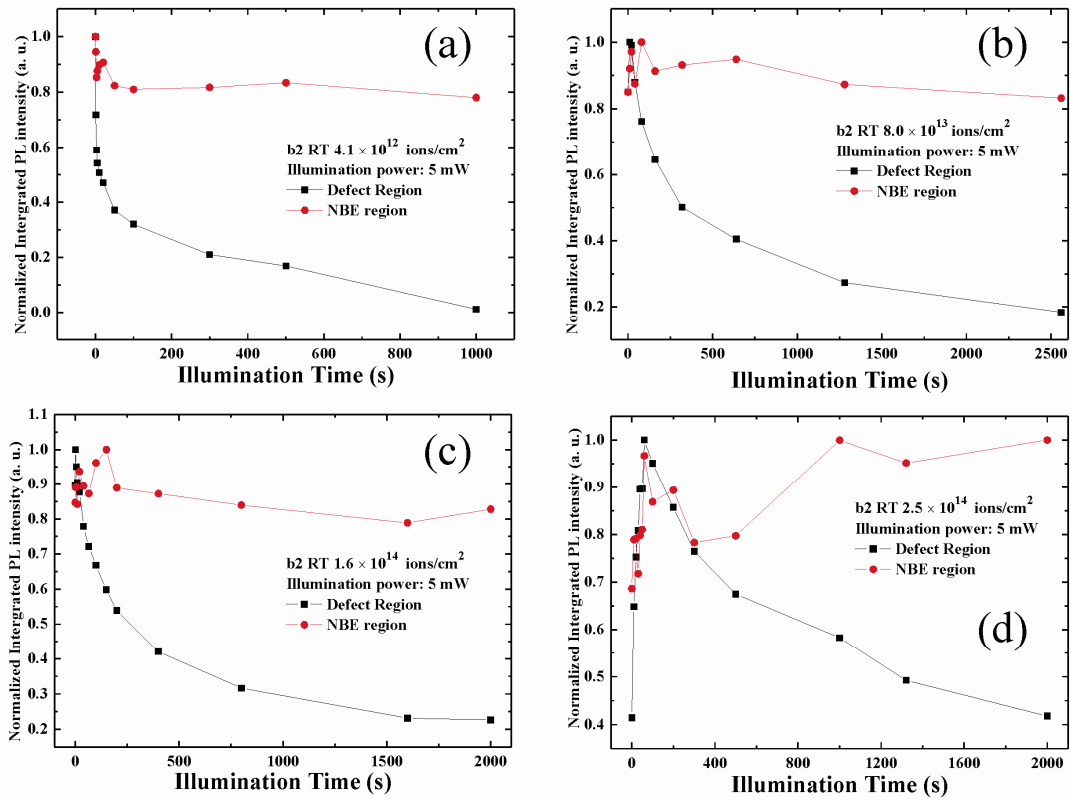
Figure 65. Dependeces of normalized integrated PL intensity on illumination time: (a) 4.1 × 10^{13}, (b) 8.0 × 10^{13}, (c) 1.6 × 10^{14}, and (d) 2.5 × 10^{14} ions/cm^2 samples. The dependences for the DL and NBE band are shown.
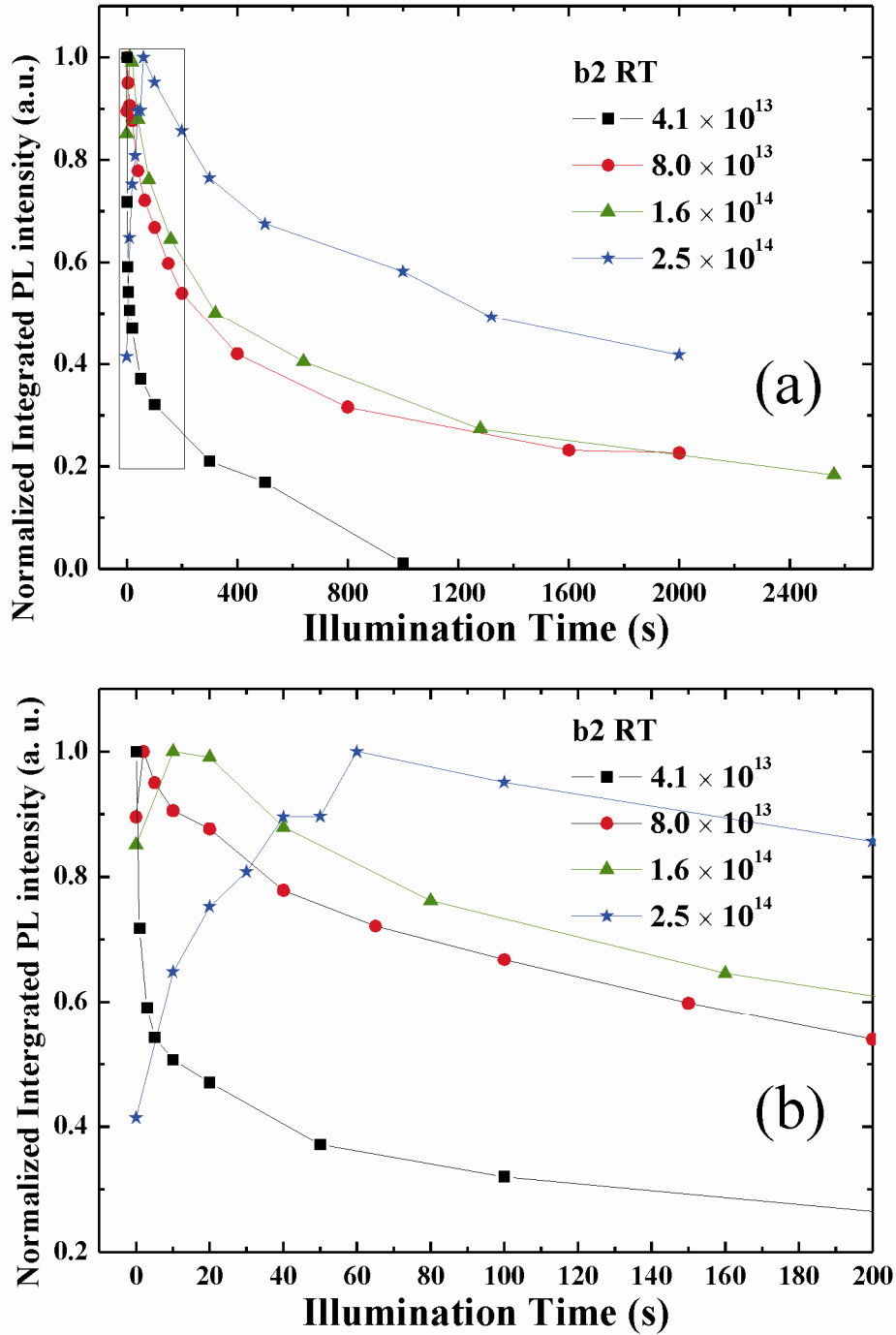
Figure 66. (a) Illumination time dependences of the DL integrated intensity in the 4.1 × 10¹³, 8.0 × 10¹³, 1.6 × 10¹⁴, and 2.5 × 10¹⁴ ions/cm² (b) detailed-view of hedged by the rectangle in the top figure.

Recently, Evans *et al*. [120] and Laiho *et al*. [121] have independently reported the dependence of electron paramagnetic resonance (EPR) intensity of singly ionized oxygen vacancies V_O^+ on illumination time. This dependence was surprisingly similar to that of the DL band PL intensity in the current study; namely, initial rapid growth was followed by a steady decrease. Meanwhile, it has been illustrated that the DL band peaked at 2.15, 2.37, and 2.55 eV as hydrothermal ZnO was annealed in ZnO, O-rich, and Zn-rich atmospheres, respectively [56].

In addition, the 2.37 and 2.55 peaks could be easily switched by solely varying annealing atmospheres [56]. Borseth *et al*. [56] attributed the 2.15, 2.37, and 2.55 bands to Li-related, V_{Zn}, and V_O point defects, respectively. In another study, Studenikin *et al*. [58] have also claimed that annealing in oxygen-deficient atmospheres resulted in the green band emission (2.43 eV), while in oxygen-rich in red band emission (1.94 eV). Furthermore, Zhao *et al*. [60] have attributed the band peaking at 2.38 eV to V_{Zn} basing on the fact that Zn-implants exerted more influence over the PL intensity than O-implants. Based on the studies mentioned above, I discuss the abnormal variations of the DL band with implantation dose and illumination time as follows.

Following the assignment of Zhao *et al*. [60], suppose that the green emission was due to the Zn-related defect transition (we presume that it is the $Zn_i \to V_{Zn}^-$ transition [122]). Implantation introduced more V_O point defects ($V_O^\times$, V_O^+, and V_O^{++}), which facilitated the conduction band to V_O^+ transition ($CB \to V_O^+$) in the orange region; therefore, the DL band red-shifted with implantation dose. During illumination, a $V_O^\times$ center released an electron [120, 123], thus, the V_O^+ concentration initially increased; further illumination reduced the V_O^+ concentration via the hole trapping reaction $V_O^+ + h \to V_O^{++}$ [123]. This explains the variation of the DL band PL intensity with illumination time and partly the blue shift after long-time exposure. However, the model could not explain why the DL band blue-shifted after short-time exposure when the increase in V_O^+ concentration still occurred. The model would contradict the studies of Borseth *et al*. [56] and Studenikin *et al*. [58].

On contrary, following the assignment of Borseth *et al*. [56], suppose that the green band was due to a V_O -related transition (we presume that the oxygen vacancy is V_O^+ in this case), there are two scenarios. First, implantation with Sn^+ ions reduced the relative V_O^+ concentration in comparison with that of other defects because, for example, V_O^+ point defects aggregate to form complexes. According to Borseth *et al*. [56], the red-shift with implantation dose could be attributed to the Li-related defect, whose relative concentration became dominant. Furthermore, illumination recovered the relative V_O^+ concentration via the electron-releasing mechanism (see the previous paragraph) as evident in the initial growth in the DL band PL intensity, and the band blue-shifted. However, this scenario could be excluded because absorbance of the implanted sample in the yellow-orange region increased with implantation dose (see Figure 50). If the yellow-orange PL band was caused by the Li-related defects, the absorbance should not increase with Sn dose. Second, implantation increased the V_O^+ concentration. As indicated by the XRD

data (see Fig. 1), formation of complexes such as multi-vacancies, multi-interstitials, or even dislocations occurred including V_O^+-complexes. Furthermore, the DL band red-shifted with implantation dose because either i) the V_O^+-complexes were still radiative and their energy was smaller than the energy of individual point defects, as argued by Studenikin *et al.* [58]; or ii) the complexes were non-radiative and emission from Li-related defects became dominant, as argued by Borseth *et al.* [56]. During illumination, the complexes dissociated and the number of individual point defects increased, which in turn caused the DL band blue-shift and an initial PL intensity increase. However, it is unclear which mechanism accounted for the dissociation of the complexes, given a small variation in temperature during illumination. Moreover, the second scenario could not naturally explain the next stage when the DL band continued blue-shifting as the band intensity decreased.

Clearly, more investigations are necessary to satisfactorily explain the abnormal behaviors of the DL band.

5 Conclusion

In the $Al_{0.5}Ga_{0.5}As$/GaAs MQW:

The PL properties of a 10-nm-$Al_{0.5}Ga_{0.5}As$/9.6-nm-GaAs MQW were investigated at temperatures in the range 5–400 K. The ratio of the intensity of the PL peak due to the $1e-1lh$ transition to that of the $1e-1hh$ transition could be described quantitatively by the formula: $\exp(-\Delta E/kT)$. This was verified by comparison with experimental data in the temperature range 50–340 K.

In order to determine the PL recombination mechanism, the dependence of the PL intensity on excitation power was measured over a wide temperature range from 5 to 296 K in small steps of 15–20 K. From the results, it was concluded that the relative contribution of free-carrier recombination to the total $1e-1hh$ PL intensity increased with temperature in the range 5–120 K, and then remained constant from 120 to 296 K. The exciton binding energy was determined to be 11.7 ± 1 meV and the activation energy of the $1e-1hh$ transition 13.4 ± 0.8 meV. Both energies were close to the thermal energy of 10.3 ± 1.7 eV, corresponding to the temperature of 120 ± 20 K.

In the hydrothermal ZnO wafers:

TEM, STEM, and EDS techniques were employed to examine ZnO wafers implanted with 60 keV Sn^+ ions at RT to a dose of 8.0×10^{14} ions/cm^2 and at LT to a dose of 1.5×10^{15} ions/cm^2. These ion implantation doses did not render the ZnO wafer amorphous. Within the sensitivity of the EDS measurement device, no regular variations in the relative concentration of O and Zn atoms were observed down to 120 nm under the sample surface.

Photoluminescence spectra of a hydrothermal ZnO wafer implanted at RT to a dose of 3.6×10^{12} ions/cm^2 were measured in the temperature range from 5 to 298 K. The sample was excited by means of the 266-nm line of an Nd^{3+}: YAG Q-switched pulsed laser with numerous average excitation powers in the range from 0.33 mW to 7.50 mW. At constant temperatures, the most intense PL peak red-shifted with average excitation power, whereas positions of other near-band-edge peaks remained unchanged. It was experimentally proven that the red-shift was not due to local heating at the excited spot. Rather, it was due to relaxation of photo-excited carriers to lower energy transitions as the most intense transition was saturated by high excitation photon density. Furthermore, the temperature dependence of the most intense PL peak energy was fitted with the Varshni equation. The Varshni coefficients α and β decreased with increasing pulsed laser excitation power.

Hydrothermal ZnO wafers implanted at RT with 60 keV Sn$^+$ ions to doses of 3.6×10^{12}, 4.1×10^{13}, 8.0×10^{13}, 1.6×10^{14}, and 2.5×10^{14} ions/cm^2 were examined by photoluminescence (PL), atomic force spectroscopy (AFM), and X-ray diffractometry (XRD) techniques. The PL intensity significantly decreased in the wafers implanted at RT to the doses of 4.1×10^{13} ions/cm^2 and higher. The AFM measurements indicate that the roughness variation was not the cause of the significant decrease in PL intensity. Furthermore, under illumination of the He-Cd laser 325 nm line the DL band peak in the PL spectra of the implanted samples blue-shifted, and the DL band intensity first increased and then steadily decreased with illumination time. The illumination time dependence of PL intensity was similar to the dependence of EPR V_O^+ signal reported previously [120, 121]. The abnormal behaviors of the DL band were discussed.

Publications

Refereed papers:

1) **Giang T. Dang**, Toshiyuki Kawaharamura, Noriko Nitta, Takashi Hirao, Toshimasa Yoshiie, and Masafumi Taniwaki: "Photoluminescence, morphology, and structure of hydrothermal ZnO implanted at room temperature with 60 keV Sn^+ ions", J. Appl. Phys. **109**, 123516 (2011).

2) **Giang T. Dang**, Toshiyuki Kawaharamura, Takashi Hirao, Noriko Nitta, and Masafumi Taniwaki: "Characteristics of ZnO Wafers Implanted with 60 keV Sn^+ Ions at Room Temperature and at 110 K", AIP Conf. Proc. **1321**, 270-273 (2011).

3) **Giang T. Dang**, Hiroshi Kanbe, and Masafumi Taniwaki: "Photoluminescence of an $Al_{0.5}Ga_{0.5}As/GaAs$ multiple quantum well in the temperature range from 5 to 400 K", J. Appl. Phys. **106**, 093523 (2009).

4) **Giang T. Dang**, Hiroshi Kanbe, Toshiyuki Kawaharamura, and Masafumi Taniwaki: "Pulsed laser excitation power dependence of photoluminescence peak energies in bulk ZnO", J. Appl. Phys. (accepted for publication).

5) V. Dneprovskii, D. Kabanin, V. Lyaskovskii, A. Santalov, T. Wumaier, **Thai Giang Dang**, and E. Zhukov: "Nonlinear absorption and refraction of CdSe/ZnS quatum dots at two-photon resonant exciation of exitons", Phys. Stat. Sol. (C) **5**, Iss. 7, 2507-2510 (2008).

6) Toshiyuki Kawaharamura, **Giang T. Dang**, and Mamoru Furuta: "Successful growth of conductive highly crystalline Sn-doped α-Ga_2O_3 thin films by fine channel mist chemical vapor deposition", Jpn. J. Appl. Phys. (Rapid communication, minor revision required).

7) **Giang T. Dang**, Noriko Nitta, Toshimasa Yoshiie, and Masafumi Taniwaki: "TEM observations of hydrothermal ZnO wafers implanted with 60 keV Sn^+ ions", J. Appl. Phys. (to be submitted).

8) **Giang T. Dang**, Toshiyuki Kawaharamura, Noriko Nitta, Takashi Hirao, Toshimasa Yoshiie, and Masafumi Taniwaki: "Reflectance, transmittance, and absorbance of ZnO implanted with 60 keV Sn^+ ions", Surface and Coatings Technology (submitted).

9) Mamoru Furuta, Toshiyuki Kawaharamura, Dapeng Wang, **Giang T. Dang**: "Electrical properties of thin-film transistors with a-IGZO channel and AlOx gate dielectric deposited by solution-based atmospheric pressure chemical vapor deposition", Applied Physics Express (submitted).

Conferences:

1) Giang T. Dang, Toshiyuki Kawaharamura, Noriko Nitta, Takashi Hirao, Toshimasa Yoshiie, and Masafumi Taniwaki: "Characterization of hydrothermal bulk ZnO implanted at room temperature with 60 keV Sn^+ ions", International Workshop on Plasma-based Ion Implantation and Deposition, September 8-12, 2011, Harbin, China.

2) Giang T. Dang, Hiroshi Kanbe and Masafumi Taniwaki: "Excitation-Power Dependence of Photo-luminescence Intensity of an $Al_{0.5}Ga_{0.5}As$/GaAs Multiple Quantum Well in the Temperature Range from 5 K to 296 K the 6th International Conference on Photonics and Applications (ICPA-6) November 8-12, 2010, Hanoi, Vietnam.

3) Giang T. Dang, Toshiyuki Kawaharamura, Takashi Hirao, Noriko Nitta, Masafumi Taniwaki: "Photoluminescence of ZnO wafers implanted with 60 keV Sn^+ ions to doses from 2×10^{14} to 1.5×10^{15} cm^{-2} at 112 K and room temperature. ",The 18th International Conference on Ion Implantation Technology, June 6-11, 2010, Kyoto, Japan.

4) T. G. Dang, H. Kanbe, and M. Taniwaki: "Photoluminescence of $Al_{0.5}Ga_{0.5}As$/GaAs multiple quantum well", Proceedings of the Workshop on Clarification of Materials Irradiation Effects and Improvement of Irradiation Technique (KURRI-KR-24), March 2009, Osaka, Japan.
5) Toshiyuki Kawaharamura, Mamoru Furuta, Dapeng Wang, **Giang T. Dang**: "Fabrication of IGZO TFT prepared by mist CVD", Thin film Materials and Devices Meeting, November 4, Kyoto, Japan.

APPENDIX: the program for calculating Kronig-Penney fits.

Table I. List of parameters utilized to calculate the $1e-1hh$ and $1e-1lh$ transitions.

| Temperature K	ΔE_c eV	ΔE_v eV	Well Electron Effective Mass, m_0	Well Heavy Hole Effective Mass, m_0	Well Light Hole Effective Mass, m_0	Barrier Electron Effective Mass, m_0	Barrier Heavy Hole Effective Mass, m_0	Barrier Light Hole Effective Mass, m_0
5	0.504514	0.229881	0.066498	0.51	0.095095	0.12014	0.635	0.121171
10	0.503705	0.229599	0.066491	0.51	0.095082	0.119998	0.635	0.12383
15	0.502895	0.229317	0.066481	0.51	0.09506	0.119856	0.635	0.126489
20	0.502086	0.229035	0.066467	0.51	0.09503	0.119715	0.635	0.129149
25	0.501276	0.228753	0.06645	0.51	0.094994	0.119573	0.635	0.131808
30	0.500466	0.228471	0.066429	0.51	0.09495	0.119431	0.635	0.134468
35	0.499657	0.22819	0.066405	0.51	0.0949	0.119289	0.635	0.137127
40	0.498847	0.227908	0.066379	0.51	0.094844	0.119147	0.635	0.139786
45	0.498038	0.227626	0.06635	0.51	0.094783	0.119006	0.635	0.142446
50	0.497228	0.227344	0.066318	0.51	0.094716	0.118864	0.635	0.145105
55	0.496419	0.227062	0.066284	0.51	0.094644	0.118722	0.635	0.147765
60	0.495609	0.22678	0.066248	0.51	0.094568	0.11858	0.635	0.150424
65	0.494799	0.226498	0.06621	0.51	0.094487	0.118439	0.635	0.153083
70	0.49399	0.226216	0.06617	0.51	0.094402	0.118297	0.635	0.155743
75	0.49318	0.225935	0.066127	0.51	0.094313	0.118155	0.635	0.158402
80	0.492371	0.225653	0.066084	0.51	0.094221	0.118013	0.635	0.161062
85	0.491561	0.225371	0.066038	0.51	0.094125	0.117871	0.635	0.163721
90	0.490752	0.225089	0.065991	0.51	0.094025	0.11773	0.635	0.16638
95	0.489942	0.224807	0.065942	0.51	0.093922	0.117588	0.635	0.16904
100	0.489133	0.224525	0.065892	0.51	0.093816	0.117446	0.635	0.171699
105	0.488323	0.224243	0.065841	0.51	0.093708	0.117304	0.635	0.174359
110	0.487513	0.223961	0.065788	0.51	0.093596	0.117163	0.635	0.177018
115	0.486704	0.22368	0.065734	0.51	0.093482	0.117021	0.635	0.179677
120	0.485894	0.223398	0.065679	0.51	0.093366	0.116879	0.635	0.182337
125	0.485085	0.223116	0.065622	0.51	0.093247	0.116737	0.635	0.184996
130	0.484275	0.222834	0.065565	0.51	0.093126	0.116595	0.635	0.187656
135	0.483466	0.222552	0.065506	0.51	0.093002	0.116454	0.635	0.190315
140	0.482656	0.22227	0.065447	0.51	0.092877	0.116312	0.635	0.192974
145	0.481846	0.221988	0.065387	0.51	0.092749	0.11617	0.635	0.195634
150	0.481037	0.221706	0.065325	0.51	0.09262	0.116028	0.635	0.198293
155	0.480227	0.221424	0.065263	0.51	0.092489	0.115887	0.635	0.200953
160	0.479418	0.221143	0.0652	0.51	0.092356	0.115745	0.635	0.203612
165	0.478608	0.220861	0.065137	0.51	0.092221	0.115603	0.635	0.206271
170	0.477799	0.220579	0.065072	0.51	0.092085	0.115461	0.635	0.208931
175	0.476989	0.220297	0.065007	0.51	0.091947	0.115319	0.635	0.21159
180	0.47618	0.220015	0.064941	0.51	0.091808	0.115178	0.635	0.214249
185	0.47537	0.219733	0.064874	0.51	0.091667	0.115036	0.635	0.216909
190	0.47456	0.219451	0.064807	0.51	0.091525	0.114894	0.635	0.219568

195	0.473751	0.219169	0.064739	0.51	0.091381	0.114752	0.635	0.222228
200	0.472941	0.218888	0.06467	0.51	0.091237	0.114611	0.635	0.224887
210	0.471322	0.218324	0.064531	0.51	0.090944	0.114327	0.635	0.230206
220	0.469703	0.21776	0.06439	0.51	0.090646	0.114043	0.635	0.235525
230	0.468084	0.217196	0.064247	0.51	0.090344	0.11376	0.635	0.240843
240	0.466465	0.216633	0.064103	0.51	0.090038	0.113476	0.635	0.246162
250	0.464846	0.216069	0.063956	0.51	0.089728	0.113193	0.635	0.251481
260	0.463227	0.215505	0.063808	0.51	0.089415	0.112909	0.635	0.2568
270	0.461607	0.214941	0.063658	0.51	0.089099	0.112626	0.635	0.262119
280	0.459988	0.214378	0.063507	0.51	0.088779	0.112342	0.635	0.267437
290	0.458369	0.213814	0.063354	0.51	0.088457	0.112059	0.635	0.272756
300	0.45675	0.21325	0.0632	0.51	0.088132	0.111775	0.635	0.278075
320	0.453512	0.212122	0.062889	0.51	0.087475	0.111208	0.635	0.288713
340	0.450273	0.210995	0.062573	0.51	0.086808	0.110641	0.635	0.29935
360	0.447035	0.209867	0.062254	0.51	0.086134	0.110074	0.635	0.309988
380	0.443797	0.20874	0.061931	0.51	0.085452	0.109507	0.635	0.320625
400	0.440559	0.207612	0.061605	0.51	0.084764	0.108939	0.635	0.331263

Table II. List of the calculated the $1e-1hh$ and $1e-1lh$ transition energies.

Temperature	$1e-1hh$	$1e-1lh$
K	eV	eV
5	1.570435	1.591335
10	1.570247	1.591247
15	1.569845	1.590945
20	1.569435	1.590635
25	1.568925	1.590225
30	1.568321	1.589721
35	1.56763	1.58913
40	1.566856	1.588456
45	1.566004	1.587704
50	1.56508	1.58688
55	1.564087	1.585987
60	1.56303	1.58503
65	1.561911	1.584011
70	1.560734	1.582934
75	1.559603	1.581903
80	1.55832	1.58072
85	1.556988	1.579488
90	1.555609	1.578209
95	1.554186	1.576886
100	1.55272	1.57552
105	1.551215	1.574115
110	1.549672	1.572672
115	1.548192	1.571292

120	1.546578	1.569778
125	1.54493	1.56823
130	1.543251	1.566651
135	1.541542	1.565042
140	1.539904	1.563504
145	1.538138	1.561838
150	1.536346	1.560146
155	1.534529	1.558429
160	1.532687	1.556687
165	1.530922	1.555022
170	1.529034	1.553234
175	1.527025	1.551425
180	1.525095	1.549595
185	1.523246	1.547846
190	1.521277	1.545977
195	1.51929	1.54409
200	1.517385	1.542285
210	1.513325	1.538425
220	1.509301	1.534601
230	1.505119	1.530619
240	1.500981	1.526681
250	1.496692	1.522592
260	1.492455	1.518555
270	1.488172	1.514472
280	1.483748	1.510248
290	1.479384	1.506084
300	1.474982	1.501882
320	1.465976	1.493276
340	1.456844	1.484544
360	1.4477	1.4758
380	1.438356	1.466856
400	1.429021	1.457921

Interface of the program written in Delphi 7 to calculate the $1e-1hh$ and $1e-1lh$ transitions.
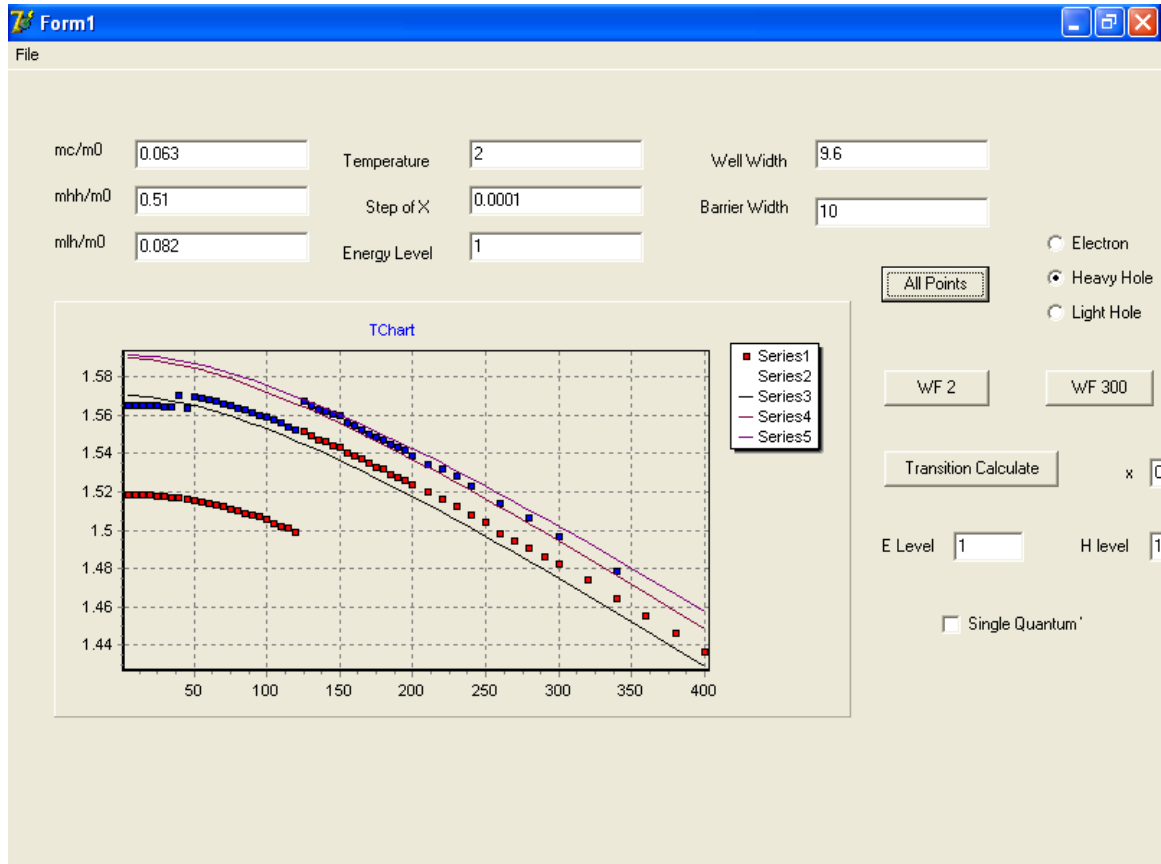
The code used to calculate the energy level, according to the Kronig-Penney model.

```
function TForm1.GetEnergyLevel(mw,mb,Eb,lw,lb,Xstep: extended; n: integer): extended;
var a,E,F,Fstore, Alp, Bet, AlpLw,BetLb: Extended;
   i,j,k : integer;
begin
 i := 0;
 F := 0;
 a := sqrt(2 * 9.1093897 * 1.60217733)/1.05457266;
 Fstore := 0;
 E := 0;
 While E <= Eb do
   begin
     if (Eb-E)<0 then Exit;
     Alp := a * sqrt(mw * E);
     AlpLw := Alp * Lw;
     Bet := a * sqrt(mb * (Eb-E));
     BetLb := Bet * Lb;
     F := (sqr(Bet) - sqr(Alp)) * sin (AlpLw) * sinh (BetLb);
     F := F + 2  *(Bet*Alp)* cos (AlpLw) * cosh(BetLb);
     F := F - 2 * (Bet*Alp);//* cos (Alp * (Lw+Lb));
     If Fstore * F < 0 then
       begin
         inc(i);
         if i = n then
           begin
             Result := E;
             exit;
           end;
       end;
     Fstore := F;
     E := E + Xstep;
   end;
end;
```

References

[1] - R.K. Willardson and A.C. Beer, *Semiconductors and Semimetals: Transport and Optical Phenomena*. Vol. 8. 1972, New York: Academic Press. 280.

[2] - D.C. Reynolds, D.C. Look, B. Jogai, C.W. Litton, T.C. Collins, W. Harsch, and G. Cantwell, *Neutral-donor bound-exciton complexes in ZnO crystals*. Phys. Rev. B, 1998. **57**(19): p. 12151.

[3] - P.J. Dean, J.D. Cuthbert, D.G. Thomas, and R.T. Lynch, *Two-Electron Transitions in the Luminescence of Excitons Bound to Neutral Donors in Gallium Phosphide*. Physical Review Letters, 1967. **18**(4): p. 122.

[4] - W. Schairer and T.O. Yep, *Two-hole transition in the luminescence of excitons bound to neutral acceptors in GaAs*. Solid State Communications, 1971. **9**(7): p. 421-424.

[5] - R.C. Miller, A.C. Gossard, W.T. Tsang, and O. Munteanu, *Extrinsic photoluminescence from GaAs quantum wells*. Physical Review B, 1982. **25**(6): p. 3871.

[6] - S.M. Sze and K.K. Ng, *Physics of Semiconductor Devices*. Third ed. 2007, New Jersey: Wiley-Interscience.

[7] - M. Razeghi, *Technology of Quantum Devices*. 2010, New York: Springer.

[8] - B.R. Nag, *Physics of Quantum Well Devices*. 2002, New York: Kluwer Academic Publishers.

[9] - R. Dingle, W. Wiegmann, and C.H. Henry, *Quantum States of Confined Carriers in Very Thin AlxGa1-xAs-GaAs-AlxGa1-xAs Heterostructures*. Physical Review Letters, 1974. **33**(14): p. 827.

[10] - P.O. Holtz, M. Sundaram, R. Simes, J.L. Merz, A.C. Gossard, and J.H. English, *Spectroscopic study of an acceptor confined in a narrow GaAs/AlxGa1-xAs quantum well*. Physical Review B, 1989. **39**(18): p. 13293.

[11] - W.T. Masselink, P.J. Pearah, J. Klem, C.K. Peng, Morko, ccedil, H., G.D. Sanders, and Y.-C. Chang, *Absorption coefficients and exciton oscillator strengths in AlGaAs-GaAs superlattices*. Physical Review B, 1985. **32**(12): p. 8027.

[12] - H. Okamoto, *Semiconductor Quantum-Well Structures for Optoelectronics: Recent Advances and Future Prospects*. Japanese Journal of Applied Physics, 1987. **26**(Part 1, No. 3): p. 315.

[13] - L.L. Chang, L. Esaki, and R. Tsu, *Resonant tunneling in semiconductor double barriers*. Applied Physics Letters, 1974. **24**(12): p. 593-595.

[14] - M. Tsuchiya, H. Sakaki, and J. Yoshino, *Room Temperature Observation of Differential Negative Resistance in an AlAs/GaAs/AlAs Resonant Tunneling Diode*. Japanese Journal of Applied Physics. **24**(Part 2, No. 6): p. L466.

[15] - W.T. Tsang, *Extremely low threshold (AlGa)As modified multiquantum well heterostructure lasers grown by molecular-beam epitaxy*. Applied Physics Letters, 1981. **39**(10): p. 786-788.

[16] - M. Takashi, H. Satoshi, F. Toshio, and N. Kazuo, *A New Field-Effect Transistor with Selectively Doped GaAs/n-Al$_x$Ga$_{1-x}$As Heterojunctions*. Japanese Journal of Applied Physics. **19**(5): p. L225.

[17] - C. Sirtori, P. Kruck, S. Barbieri, P. Collot, J. Nagle, M. Beck, J. Faist, and U. Oesterle, *GaAs/AlxGa1?xAs quantum cascade lasers*. Vol. 73. 1998: AIP. 3486-3488.

[18] - H.M. Gibbs, S.S. Tarng, J.L. Jewell, D.A. Weinberger, K. Tai, A.C. Gossard, S.L. McCall, A. Passner, and W. Wiegmann, *Room-temperature excitonic optical bistability in a GaAs-GaAlAs superlattice [e-acute]talon*. Applied Physics Letters, 1982. **41**(3): p. 221-222.

[19] - B.F. Levine, *Quantum-well infrared photodetectors*. Journal of Applied Physics, 1993. **74**(8): p. R1-R81.

[20] - T.H. Wood, C.A. Burrus, D.A.B. Miller, D.S. Chemla, T.C. Damen, A.C. Gossard, and W. Wiegmann, *High-speed optical modulation with GaAs/GaAlAs quantum wells in a p-i-n diode structure.* Applied Physics Letters, 1984. **44**(1): p. 16-18.

[21] - M. Levinshtein, S. Rumyantsev, and M. Shur, *Handbook series on Semiconductor Parameters.* Vol. 2. 1996, London: World Scientific.

[22] - T. Hayakawa, K. Matsumoto, M. Morishima, M. Nagai, H. Horie, Y. Ishigame, A. Isoyama, and Y. Niwata, *High power AlGaAs quantum well laser diodes prepared by molecular beam epitaxy.* Applied Physics Letters, 1993. **63**(13): p. 1718-1720.

[23] - D.S. Jiang, H. Jung, and K. Ploog, *Temperature dependence of photoluminescence from GaAs single and multiple quantum-well heterostructures grown by molecular-beam epitaxy.* Journal of Applied Physics, 1988. **64**(3): p. 1371-1377.

[24] - W.M. Zheng, M.P. Halsall, P. Harmer, P. Harrison, and M.J. Steer, *Acceptor binding energy in delta-doped GaAs/AlAs multiple-quantum wells.* J. Appl. Phys., 2002. **92**(10): p. 6039-6042.

[25] - X. Zhongying, X. Jizong, G. Weikun, Z. Baozhen, X. Junying, and L. Yuzhang, *The excitonic properties and temperature behaviour of the photoluminescence from GaAs-GaAlAs multiple quantum well structures.* Solid State Communications, 1987. **61**(11): p. 707-711.

[26] - L.C. Andreani and A. Pasquarello, *Accurate theory of excitons in GaAs-Ga1-xAlxAs quantum wells.* Physical Review B, 1990. **42**(14): p. 8928.

[27] - M.H. Meynadier, C. Delalande, G. Bastard, M. Voos, F. Alexandre, Li, eacute, and J.L. vin, *Size quantization and band-offset determination in GaAs-GaAlAs separate confinement heterostructures.* Physical Review B, 1985. **31**(8): p. 5539.

[28] - R.C. Miller, D.A. Kleinman, W.T. Tsang, and A.C. Gossard, *Observation of the excited level of excitons in GaAs quantum wells.* Physical Review B, 1981. **24**(2): p. 1134.

[29] - J.E. Fouquet and A.E. Siegman, *Room-temperature photoluminescence times in a GaAs/Al[sub x]Ga[sub 1 - x]As molecular beam epitaxy multiple quantum well structure.* Applied Physics Letters, 1985. **46**(3): p. 280-282.

[30] - G.D. Sanders and Y.-C. Chang, *Effect of band hybridization on exciton states in GaAs-AlxGa1-xAs quantum wells.* Physical Review B, 1985. **32**(8): p. 5517.

[31] - J. Christen and D. Bimberg, *Line shapes of intersubband and excitonic recombination in quantum wells: Influence of final-state interaction, statistical broadening, and momentum conservation.* Physical Review B, 1990. **42**(11): p. 7213.

[32] - P. Dawson, G. Duggan, H.I. Ralph, and K. Woodbridge, *Free excitons in room-temperature photoluminescence of GaAs-AlxGa1-xAs multiple quantum wells.* Physical Review B, 1983. **28**(12): p. 7381.

[33] - J.E. Fouquet and A.E. Siegman, *Room-temperature photoluminescence times in a GaAs/Al$_x$Ga$_{1-x}$As molecular beam epitaxy multiple quantum well structure.* Applied Physics Letters, 1985. **46**(3): p. 280-282.

[34] - T. Hayakawa, K. Takahashi, S. Yamamoto, and T. Hijikata, *Temperature Dependence of Photoluminescence Properties in (111)- and (100)-Oriented GaAs/AlGaAs Quantum Well Structures.* Japanese Journal of Applied Physics. **27**(Part 2, No. 6): p. L979.

[35] - S.J. Pearton, D.P. Norton, K. Ip, Y.W. Heo, and T. Steiner, *Recent progress in processing and properties of ZnO.* Prog. Mater. Sci., 2005. **50**: p. 293.

[36] - K. Kaneko, T. Nomura, I. Kakeya, and S. Fujita, *Fabrication of Highly Crystalline Corundum-Structured ($Ga_{1-x}Fe_x$)$_2O_3$ Alloy Thin Films on Sapphire Substrates.* Appl. Phys. Express, 2009. **2**(7): p. 075501.

[37] - C. Jagadish and S.J. Pearton, *Zinc Oxide Bulk, Thin Films and Nanostructures.* 2006, Oxford: Elsevier.

[38] - R.L. Weiher and R.P. Ley, *Optical Properties of Indium Oxide.* Journal of Applied Physics, 1966. **37**(1): p. 299-302.

[39] - D. Alexis and G. Michael, *Visible Light-Induced Water Oxidation on Mesoscopic $\alpha-Fe_2O_3$ Films Made by Ultrasonic Spray Pyrolysis.* The Journal of Physical Chemistry B, 2005. **109**(36): p. 17184-17191.

[40] - C.W. Bunn, *The lattice-dimensions of zinc oxide.* Proceedings of the Physical Society, 1935. **47**(5): p. 835.

[41] - Y. Chen, D. Bagnall, and T. Yao, *ZnO as a novel photonic material for the UV region.* Mater. Sci. Eng. B, 2000. **75**: p. 190.

[42] - C.P. Dietrich, M. Lange, G. Benndorf, H. Wenckstern, and MariusGrundmann, *Donor$^\perp$acceptorpairrecombinationinnon-stoichiometricZnOthinfilms.* Solid State Commun., 2010. **150**: p. 379.

[43] - Y.R. Ryu, J.A. Lubguban, T.S. Lee, H.W. White, T.S. Jeong, C.J. Youn, and B.J. Kim, *Excitonic ultraviolet lasing in ZnO-based light emitting devices.* Appl. Phys. Lett., 2007. **90**: p. 131115.

[44] - T. Gruber, C. Kirchner, R. Kling, F. Reuss, and A. Waag, *ZnMgO epilayers and ZnO?ZnMgO quantum wells for optoelectronic applications in the blue and UV spectral region.* Vol. 84. 2004: AIP. 5359-5361.

[45] - P. Yang, H. Yan, S. Mao, R. Russo, J. Johnson, R. Saykally, N. Morris, J. Pham, R. He, and H.J. Choi, *Controlled Growth of ZnO Nanowires and Their Optical Properties.* Advanced Functional Materials, 2002. **12**(5): p. 323-331.

[46] - H. Zhou, H. Alves, D.M. Hofmann, W. Kriegseis, B.K. Meyer, G. Kaczmarczyk, and A. Hoffmann, *Behind the weak excitonic emission of ZnO quantum dots: ZnO/Zn(OH)2 core-shell structure.* Vol. 80. 2002: AIP. 210-212.

[47] - P.F. Carcia, R.S. McLean, M.H. Reilly, and G. Nunes, *Transparent ZnO thin-film transistor fabricated by rf magnetron sputtering.* Vol. 82. 2003: AIP. 1117-1119.

[48] - K. Koike, I. Nakashima, K. Hashimoto, S. Sasa, M. Inoue, and M. Yano, *Characteristics of a Zn0.7Mg0.3O/ZnO heterostructure field-effect transistor grown on sapphire substrate by molecular-beam epitaxy.* Vol. 87. 2005: AIP. 112106.

[49] - T. Aoki, Y. Hatanaka, and D.C. Look, *ZnO diode fabricated by excimer-laser doping.* Vol. 76. 2000: AIP. 3257-3258.

[50] - A. Tsukazaki, A. Ohtomo, T. Onuma, M. Ohtani, T. Makino, M. Sumiya, K. Ohtani, S.F. Chichibu, S. Fuke, Y. Segawa, H. Ohno, H. Koinuma, and M. Kawasaki, *Repeated temperature modulation epitaxy for p-type doping and light-emitting diode based on ZnO.* Nat Mater, 2005. **4**(1): p. 42-46.

[51] - S. Chu, M. Olmedo, Z. Yang, J. Kong, and J. Liu, *Electrically pumped ultraviolet ZnO diode lasers on Si.* Vol. 93. 2008: AIP. 181106.

[52] - N.W. Emanetoglu, C. Gorla, Y. Liu, S. Liang, and Y. Lu, *Epitaxial ZnO piezoelectric thin films for saw filters.* Materials Science in Semiconductor Processing, 1999. **2**(3): p. 247-252.

[53] - M.-W. Ahn, K.-S. Park, J.-H. Heo, J.-G. Park, D.-W. Kim, K.J. Choi, J.-H. Lee, and S.-H. Hong, *Gas sensing properties of defect-controlled ZnO-nanowire gas sensor.* Vol. 93. 2008: AIP. 263103.

[54] - S.O. Kucheyev, J.S. Williams, C. Jagadish, J. Zou, C. Evans, A.J. Nelson, and A.V. Hamza, *Ion-beam-produced structural defects in ZnO.* Phys. Rev. B, 2003. **67**: p. 094115.

[55] - Ü. Özgür, Y.I. Alivov, C. Liu, A. Teke, M.A. Reshchikov, S. Doğan, V. Avrutin, S.-J. Cho, and H. Morkoç, *A comprehensive review of ZnO materials and devices.* J. Appl. Phys. , 2005. **98**: p. 041301.

[56] - T.M. Børseth, B.G. Svensson, A.Y. Kuznetsov, P. Klason, Q.X. Zhao, and M. Willander, *IdentificationofoxygenandzincvacancyopticalsignalsinZnO.* Appl. Phys. Lett. , 2006. **89**: p. 262112.

[57] - V.A. Nikitenko, *LUMINESCENE AND EPR OF ZINC OXIDE.* J. Appl. Spectrosc., 1992. **57**: p. 783.

[58] - S.A. Studenikin, N. Golego, and M. Cocivera, *Fabrication of green and orange photoluminescent, undoped ZnO films using spray pyrolysis.* J. Appl. Phys., 1998. **84**: p. 2287.

[59] - M. Liu, A.H. Kitai, and P. Mascher, *Point defects and luminescence centres in zinc oxide and zinc oxide doped with manganese.* J. Lumin., 1992. **54**: p. 35.

[60] - Q.X. Zhao, P. Klason, M. Willander, H.M. Zhong, W. Lu, and J.H. Yang, *Deep-level emissions influenced by O and Zn implantations in ZnO.* Appl. Phys. Lett., 2005. **87**: p. 211912.

[61] - H. Iwanaga, N. Shibata, K. Suzuki, and S. Takeuchi, *Formation of dislocation loops on prismatic faults in zinc oxide in a high voltage electron microscope* Philos. Mag., 1977. **35**: p. 1213.

[62] - V.A. Coleman, H.H. Tan, C. Jagadish, S.O. Kucheyev, and J. Zou, *Thermal stability of ion-implanted ZnO.* Appl. Phys. Lett., 2005. **87**: p. 231912.

[63] - N. Nitta, M. Taniwaki, Y. Hayashi, and T. Yoshiie, *Formation of cellular defect structure on GaSb ion-implanted at lowtemperature.* J. Appl. Phys., 2002. **92**: p. 1799.

[64] - N. Nitta, M. Taniwaki, Y. Hayashi, and T. Yoshiie, *Cellular structure formed by ion-implantation-induced point defect.* Physica B: Condensed Matter, 2006. **376-377**: p. 881-885.

[65] - M. Taniwaki, H. Koide, N. Yoshimoto, T. Yoshiie, S. Ohnuki, M. Maeda, and K. Sassa, *Amorphization and solid-phase epitaxial growth in tin-ion-implanted gallium arsenide.* Journal of Applied Physics, 1990. **67**: p. 4036-4041.

[66] - D.C. Reynolds, C.W. Litton, and T.C. Collins, *Zeeman Effects in the Edge Emission and Absorption of ZnO.* Phys. Rev., 1965. **140**(5A): p. A1726.

[67] - T. Kawaharamura, H. Nishinaka, and S. Fujita, *Growth of Crystalline Zinc Oxide Thin Films by Fine-Channel-Mist Chemical Vapor Deposition.* Jpn. J. Appl. Phys., 2008. **47**: p. 4669-4675.

[68] - X.H. Zhang, S.J. Chua, A.M. Yong, H.Y. Yang, S.P. Lau, S.F. Yu, X.W. Sun, L. Miao, M. Tanemura, and S. Tanemura, *Exciton radiative lifetime in ZnO nanorods fabricated by vapor phase transport method.* Appl. Phys. Lett. , 2007. **90**: p. 013107.

[69] - B. Kumar, H. Gong, S. Vicknesh, S.J. Chua, and S. Tripathy, *Luminescence properties of ZnO layers grown on Si-on-insulator substrates.* Appl. Phys. Lett., 2006. **89**(14): p. 141901.

[70] - H.J. Ko, Y.F. Chen, Z. Zhu, T. Yao, I. Kobayashi, and H. Uchiki, *Photoluminescence properties of ZnO epilayers grown on CaF$_2$(111) by plasma assisted molecular beam epitaxy.* Appl. Phys. Lett., 2000. **76**(14): p. 1905-1907.

[71] - V.A. Fonoberov, K.A. Alim, A.A. Balandin, F. Xiu, and J. Liu, *Photoluminescence investigation of the carrier recombination processes in ZnO quantum dots and nanocrystals.* Phys. Rev. B, 2006. **73**(16): p. 165317.

[72] - C. Li, G. Fang, N. Liu, J. Li, L. Liao, F. Su, G. Li, X. Wu, and X. Zhao, *Structural, Photoluminescence, and Field Emission Properties of Vertically Well-Aligned ZnO Nanorod Arrays.* J. Phys. Chem. C, 2007. **111**(34): p. 12566-12571.

[73] - L. Wang and N.C. Giles, *Temperature dependence of the free-exciton transition energy in zinc oxide by photoluminescence excitation spectroscopy.* J. Appl. Phys. , 2003. **94**: p. 973.

[74] - B. Cao, W. Cai, and H. Zeng, *Temperature-dependent shifts of threee mission bands for ZnO nanoneedle arrays.* Appl. Phys. Lett. , 2006. **88**: p. 161101.

[75] - D.W. Hamby, D.A. Lucca, M.J. Klopfstein, and G. Cantwell, *Temperature dependent exciton photoluminescence of bulkZnO.* J. Appl. Phys., 2003. **93**: p. 3214.

[76] - M.D. McCluskey and S.J. Jokela, *Defects in Zn.* J. Appl. Phys., 2009. **106**: p. 071101.

[77] - R. Dingle, *Luminescent Transitions Associated With Divalent Copper Impurities and the Green Emission from Semiconducting Zinc Oxide.* Physical Review Letters, 1969. **23**(11): p. 579.

[78] - K. Vanheusden, W.L. Warren, C.H. Seager, D.R. Tallant, J.A. Voigt, and B.E. Gnade, *Mechanisms behind green photoluminescence in ZnO phosphor powders.* Journal of Applied Physics, 1996. **79**: p. 7983-7990.

[79] - L.S. Vlasenko and G.D. Watkins, *Optical detection of electron paramagnetic resonance in room-temperature electron-irradiated ZnO.* Physical Review B, 2005. **71**(12): p. 125210.

[80] - W.E. Carlos, E.R. Glaser, and D.C. Look, *Magnetic resonance studies of ZnO.* Physica B: Condensed Matter, 2001. **308-310**: p. 976-979.

[81] - J.M. Smith and W.E. Vehse, *ESR of electron irradiated ZnO confirmation of the F+ center.* Physics Letters A, 1970. **31**(3): p. 147-148.

[82] - V.A. Nikitenko, *Luminescence and EPR of Zinc Oxide.* J. Appl. Spectrosc., (1992) [Zh. Prikl. Spektrosk. **57**, 367 (1992)]. **57**: p. 783.

[83] - J. Cheng and F.B. Prinz, *Damage in yttria-stabilized zirconia by Xe irradiation measured byX-ray diffraction.* Nucl. Instrum. and Meth. B, 2005. **227**: p. 577.

[84] - P. Zaumseil, U. Winter, F. Cembali, M. Servidori, and Z. Sourek, *Determination of Dislocation Loop Size and Density in Ion Implanted and Annealed Silicon by Simulation of Triple Crystal X-Ray Rocking Curves.* Phys. Status Solidi A, 1987. **100**: p. 95.

[85] - L.J.v.d. Pauw, *A method of measuring specific resistivity and Hall effect of discs of arbitrary shape.* Philips Res. Repts, 1958. **13**: p. 1-9.

[86] - B.D. Cullity, *Elements of X-ray diffraction.* Second ed. 1978, California: Addison-Wesley Publishing Company, Inc.

[87] - F. Cembali, A.M. Mazzone, and M. Servidori, *Characterization of Lattice Damage in Ion Implanted Silicon: Monte Carlo Simulation Combined with Double Crystal X-Ray Diffraction.* physica status solidi (a), 1985. **91**(2): p. K125-K127.

[88] - F. Cembali, M. Servidori, E. Gabilli, and R. Lotti, *Effect of diffuse scattering in the strain profile determination by double crystal X-ray diffraction.* physica status solidi (a), 1985. **87**(1): p. 225-233.

[89] - P. Zaumseil and U. Winter, *Triple crystal diffractometer investigations of silicon crystals with different collimator-analyzer arrangements.* 1982, WILEY-VCH Verlag. p. 497-505.

[90] - F.J. Giessibl, *Advances in atomic force microscopy.* Reviews of Modern Physics, 2003. **75**(3): p. 949.

[91] - V.J. Morris, A.R. Kirby, and A.P. Gunning, *Atomic Force Microscopy for Biologists.* 2010, Imperial College Press: London. p. 47-58.

[92] - R. Erlandsson, L. Olsson, and P. Martensson, *Inequivalent atoms and imaging mechanisms in ac-mode atomic-force microscopy of Si(111) 7 x 7.* Physical Review B, 1996. **54**(12): p. R8309.

[93] - T.R. Albrecht, P. Grütter, D. Horne, and D. Rugar, *Frequency modulation detection using high-Q cantilevers for enhanced force microscope sensitivity.* J. Appl. Phys., 1991. **69**: p. 668-673.

[94] - J.F. Ziegler, J.P. Biersack, and M.D. Ziegler, *SRIM: The Stopping and Range of Ions in Matter.* 2008.

[95] - D.B. Williams and C.B. Carter, *Transmission Electron Microscopy - A Textbook for Materials Science.* Second ed. 2009, New York: Springer.

[96] - J.W. Edington, *Practical electron microscopy in materials science.* 1976, New York: Van Nostrand Reinhold Co. 37, 183, 282.

[97] - J. Goldstein, D. Newbury, D. Joy, C. Lyman, P. Echlin, E. Lifshin, L. Shawyer, and J. Michael, *Scanning electron microscopy and x-ray microanalysis.* Third ed. Vol. 1. 2003, New York: Kluwer Academic.

[98] - C.D. Thurmond, *The standard thermodynamic Functions of the Formation of Electrons and Holes in Ge, Si, GaAs, and GaP.* J. Electrochem. Soc., 1975. **122**: p. 1133.

[99] - D.S. Jiang, H. Jung, and K. Ploog, *Temperature dependence of photoluminescence from GaAs single and multiple quantum-well heterostructures grown by molecular-beam epitaxy.* J. Appl. Phys., 1988. **64**: p. 1371.

[100] - H.J. Pain, *The physics of Vibrations and Waves.* Sixth ed. 2005, Chichester: John Wiley & Sons Ltd.

[101] - L. Hrivnak, *Determination of Gamma electron and light hole effective masses in $Al_xGa_{1-x}As$ on the basis of energy gaps, band-gap offsets, and energy levels in $Al_xGa_{1-x}As/GaAs$ quantum wells.* Appl. Phys. Lett., 1990. **56**(24): p. 2425-2427.

[102] - P.J. Dean, *Absorption and Luminescence of Excitons at Neutral Donors in Gallium Phosphide.* Physical Review, 1967. **157**(3): p. 655.

[103] - F.E. Williams and H. Eyring, *The Mechanism of the Luminescence of Solids.* The Journal of Chemical Physics, 1947. **15**(5): p. 289-304.

[104] - E.H. Bogardus and H.B. Bebb, *Bound-Exciton, Free-Exciton, Band-Acceptor, Donor-Acceptor, and Auger Recombination in GaAs.* Physical Review, 1968. **176**(3): p. 993.

[105] - D. Bimberg, M. Sondergeld, and E. Grobe, *Thermal Dissociation of Excitons Bounds to Neutral Acceptors in High-Purity GaAs.* Physical Review B, 1971. **4**(10): p. 3451.

[106] - T. Taguchi, J. Shirafuji, and Y. Inuishi, *Excitonic emission in cadmium telluride.* physica status solidi (b), 1975. **68**(2): p. 727-738.

[107] - T. Schmidt, K. Lischka, and W. Zulehner, *Excitation-power dependence of the near-band-edge photoluminescence of semiconductors.* Physical Review B, 1992. **45**(16): p. 8989.

[108] - D.R. Locker and J.M. Meese, *Displacement Thresholds in ZnO.* Nuclear Science, IEEE Transactions on, 1972. **19**(6): p. 237-242.

[109] - N. Sousbie, L. Capello, J. Eymery, F. Rieutord, and C. Lagahe, *X-ray scattering study of hydrogen implantation in silicon.* Vol. 99. 2006: AIP. 103509.

[110] - T. Singh, R. Scholz, S.H. Christiansen, U. Gösele, and R. Singh, *Surface exfoliation in ZnO by hydrogen implantation and its smoothening by high temperature annealing.* Phys. Status Solidi C, 2010. **7**(2): p. 444.

[111] - S. OZAKI, T. MISHIMA, and S. ADACHI, *Photoreflectance Spectroscopy of ZnO for Ordinary and Extraordinary Rays.* Jpn. J. Appl. Phys., 2003. **42**: p. 5465.

[112] - I. Munder, R. Helbig, and J. Lagois, *The influence of ion implantation on the excitonic reflectance of ZnO.* Solid State Communications, 1982. **41**(7): p. 553-556.

[113] - J.G. Gay, *Screening of Excitons in Semiconductors.* Physical Review B, 1971. **4**(8): p. 2567.

[114] - D.C. Look, D.C. Reynolds, C.W. Litton, R.L. Jones, D.B. Eason, and G. Cantwell, *Characterization of homoepitaxial p-type ZnO grown by molecular beam epitaxy.* Appl. Phys. Lett., 2002. **81**: p. 1830.

[115] - Y.R. Ryu, T.S. Lee, and H.W. White, *Properties of arsenic-doped p-type ZnO grown by hybrid beam deposition.* Appl. Phys. Lett., 2003. **83**: p. 87.

[116] - T.C. Damen, S.P.S. Porto, and B. Tell, *Raman Effect in Zinc Oxide.* Phys. Rev., 1966. **142**(2): p. 570.

[117] - T. Matsumoto, H. Kato, K. Miyamoto, M. Sano, E.A. Zhukov, and T. Yao, *Correlation between grainsize and optical properties in zinc oxide thin films.* Appl. Phys. Lett., 2002. **81**: p. 1231.

[118] - Y.P. Varshni, Physica (Amsterdam), 1967. **34**: p. 149.

[119] - C.H. Ahn, Y.Y. Kim, D.C. Kim, S.K. Mohanta, and H.K. Choa, *A comparative analysis of deep level emission in ZnO layers deposited by various methods.* J. Appl. Phys., 2009. **105**: p. 013502.

[120] - S.M. Evans, N.C. Giles, L.E. Halliburton, and L.A. Kappers, *Further characterization of oxygen vacancies and zincvacancies in electron-irradiatedZnO.* J. Appl. Phys., 2008. **103**: p. 043710.

[121] - R. Laiho, L.S. Vlasenko, and M.P. Vlasenko, *Optical detection of magnetic resonance and electron paramagnetic resonance study of the oxygen vacancy and lead donors in ZnO.* J. Appl. Phys., 2008. **103**: p. 123709.

[122] - G.T. Dang, T. Kawaharamura, T. Hirao, N. Nitta, and M. Taniwaki, *Characteristics of ZnO Wafers Implanted with 60 keV Sn$^+$ Ions at Room Temperature and at 110 K.* AIP Conf. Proc., 2011. **1321**: p. 270.

[123] - L.S. Vlasenko, *Point defects in ZnO: Electron paramagnetic resonance study.* Physica B, 2009. **404**(23-24): p. 4774.